THE GROWTH OF IMPACT DAMAGE IN COMPRESSIVELY LOADED LAMINATES

Thesis by

Herzl Chai

In Partial Fulfillment of the Requirements

For the Degree of

Doctor of Philosophy

California Institute of Technology

Pasadena, California

(1982)

Submitted March, 1982

ACKNOWLEDGEMENTS

I would like to thank all those faculty who have contributed to my education. In particular, I wish to express my deep appreciation to my advisor, Professor C.D. Babcock, for his guidance, encouragement and teaching example.

Many thanks to the graduate students of the Solid Mechanics group of GALCIT for their friendship. I am also grateful to all members of the Aeronautics Machine and Electronics Shops for their help. I much appreciate the help of Ms. Marta Nyiri, Mrs. B. Wood and Mr. H. Hamaguchi in the preparation of this manuscript.

This work was supported by the National Aeronautics and Space Administration. I am appreciative of this support and wish to acknowledge the interest of Dr. James H. Starnes, Jr. of NASA-Langley.

This work is dedicated to Jonathan.

PREFACE

Composite materials are recognized as an attractive replacement for metallic structures in applications where low-density and high-stiffness requirements are the primary considerations. A particular class of composite encountered in aerospace applications is the laminated composite. There are two elements, fiber and matrix, that have to be combined together to form an efficient composite laminate. The accompanying figure illustrates such a composition.

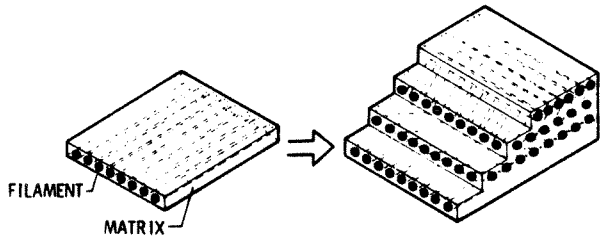

Each layer of the laminate is constructed from fibers pre-impregnated in a soft matrix to form a "tape". These tape materials, in which the fibers are all running parallel, are combined together and processed in an autoclave. The fibers in each layer or tape may be differently oriented so as to yield preferential mechanical properties.

The fact that the filament geometry and orientation are discretionary, and that various types of filaments and matrices may be combined, introduce new degrees of freedom into the development of material strength and stiffness properties. By the same token, undesired phenomena such as bending-stretching coupling[1], three-dimensional stress gradients at free edges[2], and low-strength through the plate thickness, are common. Furthermore, defects introduced during material processing can pose a severe limitation on the long-term applicability of the composite. Thickness variations, holes, cut-outs, or defects such

1 E. Reissner, Y. Stavsky, "Bending and Stretching of Certain Types of Hetrogeneous Aeolotropic Elastic Plates", J. of Appl. Mech. Vol. 28, No 3, pp 402-408, (September 1961).

2 R. Byron Pipes and N.J. Pagano, "Interlaminar Stresses in Composite Laminates Under Uniform Axial Extension", J. Comp. Materials, Vol. 4, P. 538, (1970).

as cracks, delaminations and voids can lead to a variety of failure modes in composite structures. These failure modes will depend upon the type of flaw as well as on the type of loading.

This work is concerned with the failure resulting from the simultaneous effects of low-velocity impact and compression loading. Impact causes interlaminar separation under the impact site. The superposition of a compressive load leads to local laminate buckling and stress gradients in the damaged region of the plate. This may result in failure propagation and a complete rupture of the structure at a load as low as 30% of the maximum load of the undamaged plate[3]. The severity of such a situation is exemplified in the accompanying figure, which shows failure of a large-scale structure after impact[4].

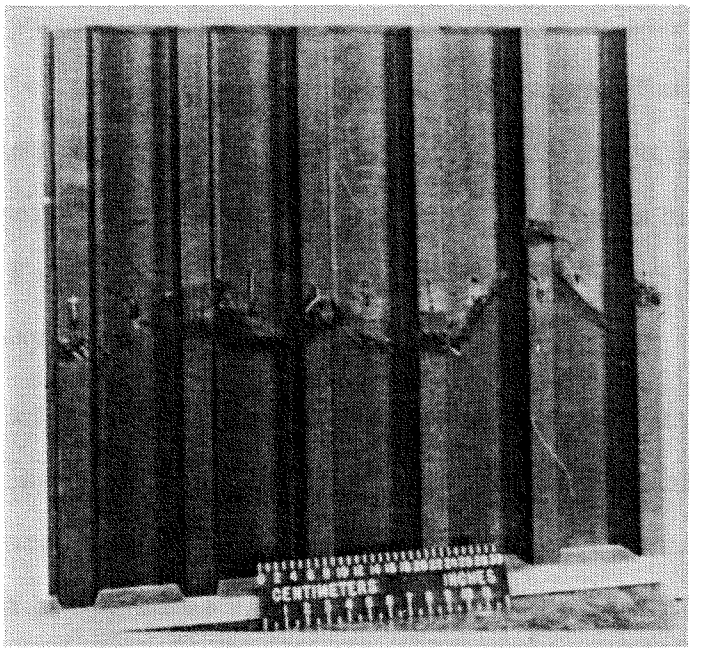

3 J.G. Williams, M.S. Anderson, M.D. Rhodes, J.H. Starnes, Jr., and W.J. Stroud, "Recent Developments in the Design, Testing and Impact-Damage Tolerance of Stiffened Composite Panels", NASA TM 80077, (April 1979).

4 M.D. Rhodes, J.G. Williams, J. H. Starnes, Jr.,"Effect of Impact Damage on the Compression Strength of Filamentary-Composite Hat-Stiffened Panels", Paper presented at the 23rd SAMPLE National Symposium and Exhibition, Anheim, California, (May 2-4, 1978).

This graphite-epoxy stiffened panel is typical of designs being proposed by NASA for heavily-loaded primary structures. The impactor is a 0.5 in. aluminum ball propelled normal to the plate at a velocity of 175 ft/sec. The load on this panel was less than 50% of the maximum load of the undamaged panel.

For the case of a tension loading an explanation of the delamination failure problem has been proposed based upon lamination plate theory[5]. The present problem of compression failure is more complicated, and no adequate failure analysis has been formulated to date. The feasibility of applying simplified damage geometries such as circular holes and cracks to predict the failure caused by impact damage was investigated in ref. 6. The predictability question in [6] was adressed by applying the "point stress" failure criterion to a wide range of plate widths and comparing the failure conditions with that of impact. While for some range of parameters strength reduction due to holes was found comparable with that of impact damage, this approach was found insufficient to describe the actual failure process occurring in impact experiments. For instance, the analysis in [6] shows that the load to failure is highly influenced by the size of the hole compared with the plate width, whereas impact tests show that there is no such a dependency.

The analysis of the problem of simultaneous in-plane compression and low-velocity impact becomes more complicated when the dynamics aspects of the failure process are taken into consideration. The impact and subsequent failure propagation can be viewed as a series of events with characteristic time scales that may overlap. The first phase of the failure is the impact which sets up a very complex system of stress waves. The complexity arises due to the

5 N.J. Pagano and R. Byron Pipes, "Some Observations on the Interlaminar Strength of Composite Laminates", Int. J. Mech. Sci., Vol. 15, p. 679, (1973).

6 M.M. Mikulas, Jr., "Failure Prediction Techniques for Compression Loaded Composite Laminates with Holes", Selected NASA Research in Composite Materials and Structures, NASA CP 2142, pp 1-33, (August 1980).

hetrogeneous nature of the composite and the interaction of the composite with the impactor. The impact duration will depend upon the material properties and will be on the order of few microseconds. The next stage in the failure scenario is laminate buckling and subsequent propagation. The mechanism by which this damage propagates and the time scale of the growth are not well understood.

A reliable treatment of such a complex problem must be based upon experimental data. These data must provide sufficient information regarding the failure propagation mechanism. In addition, it must also determine the degree of coupling between the phases of failure as well as the relative importance of the global plate response on the failure process. If a temporal separation of the various phases of growth is found, then it will become much simpler to develop a suitable analysis. Only after such information has been gathered, will one be able to formulate a valid model of failure. It is with this philosophy in mind that this problem is undertaken.

The thesis is divided into two chapters. The first chapter describes an experimental program carried out to determine the phenomenological aspects of composite panel failure (graphite/epoxy laminate) under simultaneous in-plane compression and low-velocity transverse impact (0-250 ft/sec). High-speed photography and the shadow moire technique were used to record a full-field, surface deformation history of the impacted plate. The information gained from these records, supplemented by plate sectioning and observation for interior damage, has shown that the predominant failure mechanism is the coupled effect of delamination and buckling.

In chapter 2, this process of failure is modelled by delamination buckling wherein the local delamination stability, growth or arrest are governed by an

energy release rate criterion. Various degrees of problem simplifications are employed, starting with a one-dimensional, delaminated-beam model. In the most sophisticated treatment, it is assumed that the damaged area has an elliptical shape. It was found that this model is capable of describing the growth conditions and the growth behavior of the damaged area. It was also found that the predominant parameter controlling delamination growth or arrest is the fracture energy associated with delamination.

In the appendix at the end of this work, the fracture energy of a composite laminate is considered. A modified cleavage analysis is developed, and is applied to evaluate this quantity for two composite materials of current interest. The test results are then examined with reference to impact damage tolerance data available for these materials. A viscoelastic characterization of the two resins used to fabricate the two composites mentioned above is also provided. The results of these measurements are then examined with reference to long-term applicability of the matrix material.

TABLE OF CONTENTS

CHAPTER 1

OBSERVATION OF DAMAGE GROWTH IN COMPRESSIVELY LOADED LAMINATES

ABSTRACT

An experimental program to determine the phenomenological aspects of composite panel failure under simultaneous compressive in-plane loading and low-velocity transverse impact (0-250 ft/sec) was carried out. High-speed photography coupled with the shadow moire technique was used to record the failure propagation phenomenon. The information gained from these records, supplemented by plate sectioning and observation for interior damage, has provided information regarding the failure propagation mechanisms.

The results show that the failure process can be divided into two phases. In the first phase the plate is impacted, and the resulting response causes interlaminar separation. In the second phase the local damage spreads to the undamaged portion of the plate through a combination of laminate buckling and further delamination.

TABLE OF CONTENTS

NOMENCLATURE

n = fringe number

V = impact velocity

w = out-of-plane displacement

w/n = fringe constant

Δt = time interval between frames

ε_0 = compression strain

1.1 INTRODUCTION

Graphite/epoxy laminates are a special class of composites which enjoy a definite strength-to-weight advantage over many standard engineering materials used in aerospace applications. While their load carrying capacity is comparable with aluminum, for instance, their mass density is about 40% lower. This advantage is somewhat lessened, however, by their sensitivity to operational hazards such as low-velocity impact by foreign objects. Impact may cause considerable damage since the cohesive strength of the plate through its thickness is quite low. Under the action of compression load, this local damage, which occurs in the form of cracks and delaminations between plies, may grow to the undamaged area of the plate. This leads to a global failure of the structure at a load well below the design level. For this reason the application of this material in the commercial aircraft industry is currently limited to secondary structures, which are either lightly-loaded components or are located at places where no impact damage is likely to occur. The full mass-saving advantage can be achieved, however, only in primary structure usages such as fuselage, wing skin, etc. Unfortunately, primary structures may be subjected to both high-compression load and impact damage which may even occur at the same time. This situation is exemplified, for instance, when a runway stone impacts the wing skin at the bottom during landing or take-off. The vibratory motion generated by the landing action induces compression-tension cycles at the skin. If the impact occurs during the compression cycle, then the local damage induced by impact can propagate away leading to a global failure of the structure.

The effect of impact damage on the strength degradation of composite laminates is usually characterized by the catastrophic failure threshold curve as shown in fig. 1. This curve is generated by impacting panels pre-loaded in compression and by assessing the post-impact conditions. Panels that failed

globally upon impact have load-impact velocity data above the failure threshold curve whereas those which did not fail upon impact, even though they may have incurred a local damage, have data below this curve. Also shown in fig. 1 a graph of the damage area caused upon impact versus the impact velocity. It can be seen from fig. 1 that for small impact velocity (range I, i.e. $V < 120$ ft/sec) there is no damage and no strength reduction in the laminate. For larger impact velocity (range II), the damage area increases while the plate strength decreases. At impact speed above 300 ft/sec (range III), the plate will fail at about 30% of its undamaged load-carrying capacity.

A considerable effort has been devoted in the past and throughout the course of this investigation to the evaluation of the effect of low-velocity impact damage on the strength degradation in compressively loaded graphite/epoxy composite laminates [1-6]. In all these works, the consequences of failure were studied via post-mortem examination of the impacted plates. While the effect of impact damage was fairly well established in [1-6], little information concerning the damage-spreading mechanisms was developed. The large amount of energy released during catastrophic failure usually leads to a considerable disintegration of the test specimen making it difficult if not impossible to deduce the nature of the damage-spreading mechanisms.

In this work, an experimental program to determine the damage growth mechanisms in compressively loaded graphite/epoxy flat laminates subjected to low-velocity impact is carried out through real-time recording of the impact event. The material selected, a 48-ply orthotropic laminate, is typical of designs being proposed for future heavily-loaded primary structures and has stiffness properties similar to existing transport aircraft wing skins. The projectile is a 0.5 in. diameter aluminum sphere propelled normal to the plane of the plate at a velocity in the range of 0-250 ft/sec. The projectile mass and speeds simulate

momentum typical of low-velocity impact hazards that occur in commercial aircraft service. The main tool in this investigation is high-speed photography coupled with the shadow moire technique to record a full-field surface deformation history of the impacted plates.

One of the most difficult experimental aspects of high-speed photography and moire is specimen illumination. The need to record a rapidly propagating phenomenon at an exposure time on the order of one microsecond, plus the fact that in the moire method the plate surface is a diffuse surface, requires an intense light source. A considerable effort was devoted to developing techniques to meet this challenge. This subject is also discussed in the following.

1.2 TEST APPARATUS

An apparatus was developed to conduct impact tests on graphite/epoxy panels and to record the impact event in real time. Section 1.2.1 describes the loading and impact facilities which include the panel support fixture, the loading machine and the impact device (air-gun). Details of the recording, including the shadow moire technique, the light source and two high-speed cameras are given in section 1.2.2 . A photograph of the test set up including all the components mentioned above is shown in fig. 2.

1.2.1 Loading and Impact Facilities

Following is a brief summary on the impact and loading facilities:

Panel Fixture: Two fixtures have been designed to support the two different sizes of graphite/epoxy panels used in this work, i.e. the 8x4x0.24 in. panel ("small panel") and the 10x6x0.24 in. panel ("large panel"). These fixtures are shown in fig. 3. The upper and lower edges of the panel which transmit the load are bonded to aluminum plates in grooves which were filled with a bonding agent (Devcon). The grooves' depths in the small and large panel fixtures are 0.4 in. and 1.0 in., respectively. In the small specimen fixture, both sides of the specimen are held by 0.1 in. wide flat surfaces which are adjustable along the length of the specimen to ensure a close, but not binding, support. In the large panel fixture, the specimen sides are held by 0.2 in. radius circular surfaces. The edges and sides support details are given in fig. 4.

Loading Machine: The load applied to the specimens was achieved by using a hydraulic testing machine capable of exerting loads up to 150 tons. A spherical base support was used to transmit the load to the specimen to assure uniformity in the load distribution. The latter was measured by using as many as eight strain gages and was found to be within ± 3% of the mean.

Impact Device: The projectile is accelerated using a simple air-gun consisting of a compressed-air reservoir, solenoid activated valve and a 15 in. long barrel. The projectile velocity is controlled by adjusting the pressure in the reservoir and is measured by twice interrupting a light beam monitored by a photodiode. The time interval between beam interruptions is measured by a counter. This method allowed the projectile velocity to be controlled and measured to an accuracy of ± 1%.

1.2.2 Recording Facilities

Following is a description of the recording facilities.

Shadow Moire: This technique was adopted in this work to record full-field normal displacements of the plate during impact. A review of this method can be found in [7] and only a brief summary is given below.

Moire is an optical phenomenon based on the interference of light formed with two gratings; one grating being stationary and undeformed (the master grating) while the other deforms with the specimen. As the specimen grating deforms, a fringe pattern related to the surface deformation of the specimen is observed. In the shadow moire, a grid placed close to the specimen surface serves as the master grating while its shadow on the matte-reflective surface of the plate, formed by an incident collimated light beam, serves as the specimen grating. Referring to fig. 5 and [7], the normal displacement w is given as follows:

$$\frac{w}{n} = \frac{p}{\tan \Theta_1 + \tan \Theta_2} = \text{Fringe Constant} \qquad (1)$$

where n is the fringe constant, p is the grating pitch and Θ_1 and Θ_2 are the angles formed between the normal to the plate and the directions of the incident and viewing light, respectively.

A 100 lines/in. Ronchi-ruled grid was used as the master grating. The grid was placed close to the specimen surface (0.08-0.16 in.) for sufficient fringe contrast. Because the grating was destroyed in each test, replicas of the grating were formed by contact printing the master onto high-contrast, high-resolution Kodak Ortho Plate PFO. The matte reflective surface for the shadow moire was achieved by painting the plate surface with Krylon "silver" spray paint.

Light Source: Lighting is a recurring problem in high-speed photography applications such as shadow moire. The matte reflective surface of the specimen allows for only a fraction of the incident light beam to be collected by the camera lens. This, along with the need to record a rapidly propagating phenomenon at an exposure time on the order of one microsecond, required a very intense light source which was not readily available. A considerable effort has been devoted to meet this condition. In the first phase of this work, a 200 Watt Mercury short arc (0.1 in. arc gap) lamp, housed in a Pek Lamphousing Model M-12, was employed. This provided a point source of sufficient quality, but not enough light intensity, under normal recommended usage. The amount of light was increased by pulsing the lamp to 800 Watts during the impact event. This was achieved by overpowering the lamp prior to impact, but blocking the excess power with a variable resistor. During impact the resistor was shorted by means of a mechanical relay, thus allowing the extra current to discharge through the lamp, according to the record shown in figure 6a. Because the event of interest lasted less than 1 msec., it was sufficient to employ only the peak part of the light trace in figure 6a during the impact recording. The pulsed Mercury lamp has yielded sufficient amount of light for recording the small panel area but was found insufficient to provide an adequate illumination for the large panel. In recording the large panels, a Xenon flash tube was employed. The tube is powered by a bank of capacitors which is capable of discharging 4000 Joules

over a short period of time. A system of collimating lenses, shown in fig 6b, was employed so that the light emerging from this source is collimated and uniform. The flash duration and shape can be controlled by adjusting the discharging rate of the capacitors and was selected to produce a one millisecond duration pulse of uniform intensity as shown in the record in fig. 6b. The flash tube was triggered by the projectile using a simple wire-breaking circuit. The two light sources discussed above were used simultaneously in some tests to record both back and front panel surfaces during the impact event.

High Speed Camera: One or two 16 mm Hycam (Red Lake Laboratory, Model K2054BE) high-speed framing cameras were used to record the impact event. A quarter-frame assembly was installed in one camera to increase its recording rate up to 40,000 frames/sec. The exposure time, controlled by an interchangable shutter, was selected to be in the range of 2.5-5μs. In cases where two cameras were used simultaneously, a common timing light pulse displayed on the developed films was used for syncronization between the two motion pictures. A Kodak pan film, 2484 high-speed film, rated at 800 A.S.A., was used to help in meeting the severe light requirement.

1.3 IMPACT EXPERIMENT RESULTS AND DISCUSSIONS

Impact tests were carried out on two sets of graphite/epoxy panels and the impact event photographed. The laminate properties, test procedure and test conditions are given in section 1.3.1. In section 1.3.2 the damage induced by impact is characterized through plate sectioning and observation with a microscope. Section 1.3.3 presents high-speed photographs of the damage propagation along with their interpretation and discussion with an eye towards the development of damage growth mechanism.

1.3.1 Test Procedure and Test Data

The panels tested in this investigation were furnished by NASA-Langley. The specimens were fabricated from commercially available tapes made from unidirectional Thornel-300 graphite fibers preimpregnated with Narmco-5208 epoxy resin (28% resin content). The tapes or layers were laid up to form a 48-ply $(+45/-45/0/0/+45/-45/0/0/+45/-45/0/90)_{2s}$ orthotropic laminate. The nominal ply properties and the calculated composite stiffnesses are given in table I. Two groups of plates of different sizes were tested in this work, i.e. a 8x4x0.24 in. panel ("small panel") and a 10x6x0.24 in. panel ("large panel"). This selection of plates size reflects a compromise between the desire to have a relatively stiff panel which can sustain a high load without global buckling and one which is large enough to allow for damage growth over a large area without interference with the plate boundary.

The panels, supported by the panel fixture, were impacted at the center while under compressive load and the impact event was photographed by a high-speed camera. The test conditions are summarized in table II and displayed in fig. 7 along with the catastrophic failure threshold curve from ref. 4. The solid symbols in fig. 7 represent specimens that failed catastrophically upon impact while

the open symbols represent specimens that did not fail catastrophically upon impact. A failure threshold curve was drawn for the large panels and is also shown in fig.7. In the construction of this curve, use was made of the high-speed photographs; panels close to this curve exhibited slow propagation rates, which offered good threshold data. It is noted that this curve is somewhat lower than the threshold curve of ref. 4. However, that curve was drawn with limited data in what appears to be a transition in the threshold curve. As can be seen from fig. 7, the majority of the tests were carried out in the middle of the transition region in the threshold curve. This selection was made in the belief that more could be learned about the damage growth behavior by testing in this range which features sensitivity to both impact velocity and strain.

Some panels that did not fail catastrophically upon impact were examined ultrasonically and/or sectioned through the plate thickness at different locations and examined microscopically for interior damage. In all tests, the panel back-surface was photographed in real time using a high-speed camera. These records were made in conjunction with the shadow moire technique. In some tests back-surface moire and front-surface moire or back-surface moire and panel edge cinematographs were taken simultaneously to assist in relating the observed surface deformation to the interior damage. The photographic procedure is given in table II.

1.3.2 Interior Damage Characterization

Fig 8a shows an ultrasound C-Scan[1] record of a plate impacted while under zero load. From this record, the damage area appears nearly circular in shape with approximately 1.2 in. in diameter. This panel was then sectioned horizontally (or along the 90^0 plies) through the impact point and a photograph of this

1 The C-Scans were carried out by Dr. J.H. Starnes, Jr., NASA-Langley, to whom the author is grateful.

section is shown in fig. 8b. The print shows that the plate has incurred damage across its full thickness, with the damage being more extended toward the unimpacted panel face than toward the impacted face. The damage is mainly in the form of matrix failure or delamination and intraply cracking.

Fig. 8c shows a section of a plate which was loaded during impact. This section is along the load axis (or along the 0^0 plies) and through the impact point. The appearance and distribution of the damage in fig. 8c is quite similar to that in the unloaded case shown in fig. 8b, though the damage extends over a larger area due to the effect of the load. A section parallel to this section, but 0.5 in. away, is shown in fig 8d. This print shows that the delaminated area is confined only to the vicinity of the surface opposed to the impact face. As mentioned earlier, this plate did not fail upon impact. Since the conditions at impact were close to the threshold condition, the initial damage area is similar to that of the panels that did fail upon impact.

1.3.3 Results of High-Speed Photography

In this section, high-speed records of the damage propagation resulting from impact are presented and discussed with an eye towards the establishment of a damage growth model. Two groups of panels which differ only by their sizes were tested. In the small panel group, the effort was directed toward understanding the basic damage growth phenomenon by confining the test data (i.e. impact velocity and load) to a narrow domain, and by photographing the propagating damage from several positions. For the large panel group, emphasis was placed on the more detailed aspects of the growth phenomenon by increasing the range of loading and impact velocity. The results for the two groups of panels are presented separately.

Results of High-Speed Photography - Small Panels

As can be seen from fig. 7, the majority of the tests for the small panels were carried out over a narrow range of impact velocity (200-250 ft/sec) and compression strain (0.0030-0.0035) where the strength degradation due to impact is most pronounced. A relatively small load was selected (about 25% of the buckling load of this panel) so that the effect of global plate response due to impact on the local damage growth process would be as small as possible.

A typical back-surface moire pattern showing failure of a plate after impact is shown in fig. 9a along with the camera field of view. The fringes shown in the prints represent contours of equal out-of-plane displacements. For convenience, these displacements are presented in fig. 10 as a function of horizontal and vertical coordinates which originate at the impact point. The displacements in fig. 9a and fig. 10 include both permanent and vibration deformations. However, an analysis[2] has shown that the contribution of the vibration term to the total displacement is small and the latter can be viewed as representing permanent deformation or damage. Frame 0 in fig. 9a represents the condition just prior to impact and has been assigned the time t=0. In the subsequent frame the impact has already occurred and it caused a bulging of the surface near the impact region with a peak displacement on the order of 0.05 in. . Based on the results of section 1.3.2, this bulging of the surface is interpreted as a local buckling of the delaminated area under the action of the compressive load. Subsequent frames, at 50μs time interval, show that this buckled region propagates to the undamaged area of the plate in a direction which is normal to the loading. The growth rate is approximately 1000 ft/sec, with the peak displacement

2 The analysis, based upon orthotropic plate theory and a Hertzian contact model for the impact load history, has indicated that the maximum displacement that would be expected under conditions that simulate the test conditions would be on the order of 0.01 in. or approximately a single fringe in fig. 9a.

increasing during the growth.

While the growth history of the damage at the back-surface of the panel is fairly well understood from fig. 9a, no information was revealed concerning the damage extension in the interior of the plate during the growth process. It was thought that this information could be gained by recording the other surfaces of the panel (i.e. front-surface and corner or side surface) during the impact event. Fig. 9b shows the front-surface moire version of the panel in fig. 9a (a 0.6 in. diameter hole was drilled at the grid center to allow for impact without destroying the grid). Note that the dark area in this series of photographs is due to interruption of the illuminating light beam with the barrel edge. The two motion pictures in fig. 9 were recorded simultaneously using two high-speed cameras[3], and the time relation between the two series of frames was evaluated using the common timing light pulse. This relation is marked in fig. 9b with reference to the time t=0 set for frame 0 in fig. 9a. Impact has already occurred in the second frame in fig. 9b (t = 23μs). Subsequent frames show that a characteristic deformation[4] has developed and propagated across the panel width with little growth in the vertical direction. Comparing the time history of this growth to that in the back-surface (fig. 9a), it is evident that the two growth phenomena at the front and back-surfaces are closely related in time. This indicates that the full thickness of the plate has suffered damage during the growth process.

The other photographic procedure employed to aid in relating the observed surface damage boundary to an internal damage boundary was a simultaneous recording of the back-surface and the panel side. For this purpose, a 1.5 in. long clearance was made along the edge of the panel fixture as shown in fig. 3. This clearance, while allowing for panel side vision, does not alter the support

3 The author is grateful to J.P.L. Photo-Lab for supplying the additional camera.

4 Based on post-mortem examination of the deformed panel, and also on an estimate of the projectile contact duration, this deformation is interpreted to be toward the plate midplane.

condition along the panel edge. The result of this test is shown in fig. 11. The sequence of events for the back-surface is much the same as discussed earlier, though the damage growth rate appears somewhat slower due to the lower load. It is noted, however, that the characteristic deformation has reached the left edge of the panel at approximately 300μs after impact. This occurrence is equivalent in time to the appearance of the first crack at the edge (frame 6' in the lower sequence in fig. 11). The result of this experiment suggests that the internal damage front does not extend much beyond the first or lowest order fringe in the moire pattern. This damage extension association will be used later in this work. Subsequent frames in both motion pictures show the final stages in the collapse of the panel. The relatively long time it took for this to occur (approximately 1.5 ms. after impact) may be attributed to the response of the testing machine.

Results of High-Speed Photography - Large Panels

The test data for the large panels cover a relatively broad domain in the transition region in the threshold curve (fig. 7) which allows for evaluation of the more detailed aspects of the damage growth phenomena. Fig. 12 shows a series of four back-surface motion pictures for four panels which were all impacted at the same velocity but were loaded differently. The failure process for these tests is much the same as for the small panels discussed previously. However, the relatively large dimension of these panels and the broad range in the loading conditions allow the evaluation of the dynamics of the growth process. Fig. 12 indicates that the rate of growth of the characteristic damage increases as the damage spreads, and is larger for greater loadings. Fig. 13a gives the growth rate history of the delamination area for four different panels, three of which are shown in fig. 12. The growth rate was evaluated based on the amount of the horizontal extension of the damaged area, as defined in the insert in fig. 13a,

over the time interval between two adjacent frames in the moire sequence. Similar symbols in fig.13a represent data from a single test. All tests exhibit a phase of relatively slow growth which is followed by a "smooth" and rapid growth as the delamination area spreads. A systematic transition between these two phases of growth is not strictly apparent from the data presented, but it is seen that the phase of rapid propagation starts after the damage has extended over about 2 inches. For a delamination of twice this size, the growth rate is more than doubled, reaching a value of up to 2500 ft/sec for the test with the highest load. The dependence of the growth rate upon the load level is shown in fig. 13b. This figure was constructed from fig. 13a by extrapolating the vertical axis at a given delamination size for panels with various loadings. The results show that the delamination propagation speed is strongly affected by the strain level. An increase of about 40% in the load leads to an increase of about 250% in the propagation speed.

There are other features which can be inferred from fig 12. The first to be noted concerns the effect of the load level on the extension of the delaminated area along the load axis. Fig. 12 shows that panels with larger loads have not yielded larger damage spread in the load axis than those with the smaller loads; in fact the opposite of this seems to occur. This observation is somewhat surprising judging from post-mortem examinations which usually show that the panels with the larger loads have more massive damaged area. The other observation to be noted concerns the failure mechanism itself. Some frames in fig. 12 show a distortion at the horizontal front of the damaged area which is not associated with the familiar buckling type deformation. This is particularly evident in the latter sequence in the failure process (i.e. when the damage is fairly extended) or in the panels with the larger loads. In these cases the load carried by the undamaged portions of the plate becomes exceedingly large, which may

lead to other types of failure.

Some panels have yielded damage growth patterns which are distinguished from those presented earlier in either the geometry or the nature of the damage growth process. A test which belongs to the first category mentioned is shown in fig. 14. The interesting feature of this test is the "rectangular" type boundary of the propagating delamination, which differs from the more contoured boundary observed in the majority of the tests. This difference, however, does not seem to have an effect on the nature and sequence of the growth process as observed and discussed earlier. This type of growth was observed in some other tests, especially those with relatively large impact velocity, and is significant in that it allows some degree of freedom in formulating an analytical model of damage growth.

The result of a test belonging to the other category mentioned above is shown in fig. 15. As can be seen, this panel has failed in a rather unique fashion, with the failure occurring as a consequence of the global plate response. The test conditions for this panel are at the far left portion of the threshold curve (fig. 7) with the impact velocity relatively small (152 ft/sec) and the load relatively large (ε = 0.0054 or about 70% of the buckling load for this panel). Apparently, the damaged area induced by impact has not buckled locally and the plate has failed at a latter stage as a result of global buckling.

CONCLUSIONS

The results of the damage propagation in a compressively loaded composite laminate will now be summarized. When an object impacts a composite laminate, damage or delaminations may result. Under in-plane compression, the delamination area may buckle and propagate to the undamaged area of the plate through a combination of ***delamination and buckling***. This growth, which always occurs at a right angle to the load, starts at a relatively slow speed and is followed by a "smooth" and rapid propagation which accelerates as the delamination spreads. The propagation speed of the delamination region is strongly influenced by the strain level and a speed up to 2500 ft/sec was recorded for the largest strain attempted. While this speed is small in comparison with the sound speed for this material, it is quite substantial.

The consistency in the growth behavior during the rapid growth phase observed in many tests indicates that this phase can be separated temporarily from the damage generation phase as well as from the global plate response due to impact. This assessment, which was found to be valid so long as the load is not near the buckling load of the plate, will be of great help in the formulation of a damage growth model.

REFERENCES

1. J.G. Williams, M.S. Anderson, M.D. Rhodes, J.H. Starnes, Jr., and W.J. Stroud, "Recent Developments in the Design, Testing and Impact-Damage Tolerance of Stiffened Composite Panels", NASA TM 80077, (April 1979).

2. J.H. Starnes, Jr., M.D. Rhodes and J.G. Williams, "The Effect of Impact Damage and Circular Holes on the Compressive Strength of a Graphite-Epoxy Laminate", NASA TM 78796, (October 1978).

3. M.M. Mikulas, Jr., "Failure Prediction Techniques for Compression Loaded Composite Laminates with Holes", Selected NASA Research in Composite Materials and Structures, NASA CP 2142, pp 1-33, (August 1980).

4. M.D. Rhodes, "Damage Tolerance Research on Composite Compression Panels", Selected NASA Research in Composite Materials and Structures, NASA CP 2142, pp 107-142 (August 1980).

5. R. Garcia and M.D. Rhodes, "Effects of Low-Velocity Impact on Graphite/Polyimide Compression Laminates", Graphite/Polyimide Composites, NASA CP 2079, pp 239-248, (February 1979).

6. B.A. Byers, "Behavior of Damaged Graphite/Epoxy Laminates Under Compression Loading", NASA CR 159293, (August 1980).

7. S.T. Theocaris, "Moire Fringes in Strain Analysis", Pergamon Press, (1969).

Table I - Material Properties for T300/5208 Graphite/Epoxy

Lay Up: $(+45/-45/0/0/+45/-45/0/0/+45/-45/0/90)_{2S}$

Nominal Ply Properties

Longitudinal modulus, $E_1 = 19.00 \times 10^6$ psi

Transverse Modulus, $E_2 = 1.89 \times 10^6$ psi

Shear Modulus, $G_{12} = 0.93 \times 10^6$ psi

Major Poisson's ratio, $\nu_{12} = 0.38$

Ply thickness = 0.0055 in. (0.14 mm)

Density = 0.055 lbm/in^3 (1.52 g-cm^3)

Laminate Stiffness Properties

Dimension: A_{ij}: 10^6 x lbf/in. (=0.176 GN/m)

D_{ij}: 10^3 x lbf-in. (112.98×10^{-9} N-m), i,j= 1,2,6

$$\begin{bmatrix} N_x \\ N_y \\ N_{xy} \\ M_x \\ M_y \\ M_{xy} \end{bmatrix} = \left[\begin{array}{ccc|ccc} 3.03 & 0.72 & 0.00 & & & \\ & 1.51 & 0.00 & & 0 & \\ \text{SYM.} & & 0.77 & & & \\ \hline & & & 17.71 & 4.57 & 0.23 \\ & 0 & & & 7.88 & 0.23 \\ & & & \text{SYM.} & & 4.88 \end{array}\right] \times \begin{bmatrix} \partial u/\partial x \\ \partial v/\partial y \\ \partial v/\partial x + \partial u/\partial y \\ -\partial^2\omega/\partial x^2 \\ -\partial^2\omega/\partial y^2 \\ -2\partial^2\omega/\partial x \partial y \end{bmatrix}$$

Table II - Test Conditions

Notation:

Test Data: v = Impact velocity (ft/sec), ε_0 = Compression strain (micro-strain)

Photo Procedure : BM,FM-Back and front surface moire, respectively, SP-panel side photo

Post Test Conditions:PF-Panel failed upon impact, NF-Not failed

Small Panel (8x4x0.24 in.)

v	ε_0	photo proc.	post test conditions
233	3257	BM&FM	F
217	3220	"	"
192	4500	"	"
249	2940	BM&SP	"
95	8620	"	NF
214	3458	SP	F
208	3335	BM	"
"	3250	"	"
214	3178	"	"*
"	3510	"	"
"	3376	"	"
"	190	"	NF
226	100	"	"
214	3273	"	"

Large Panel (10x6x0.24 in.)

v	ε_0	photo proc.	post test conditions
226	3810	BM	F
"	3630	"	"
214	3900	"	"
246	3660	"	"
214	4050	"	"
246	3426	"	"
214	4500	"	"
"	4930	"	"
"	5570	"	"
178	4790	"	"
152	5448	"	"
230	4069	"	"
248	3564	"	"
185	4025	"	NF
163	4970	"	NF

*Panel failed about 1 minute after impact

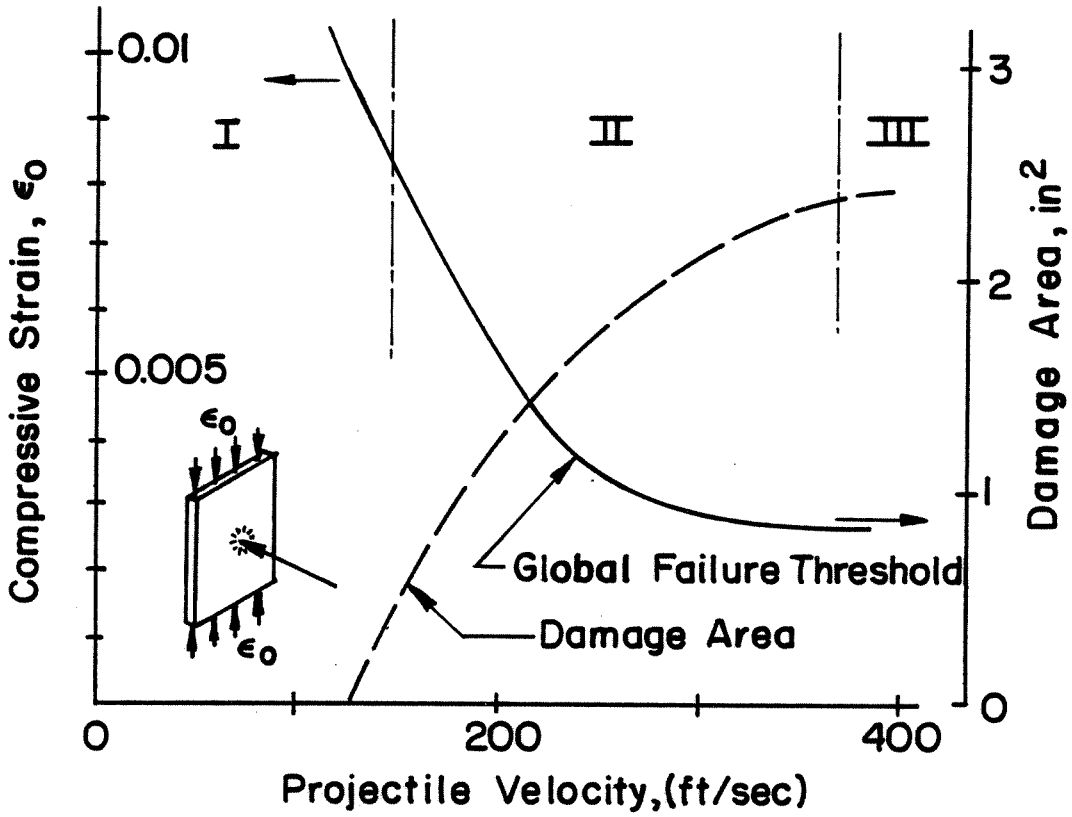

FIG. 1 THE EFFECT OF LOW-VELOCITY IMPACT ON THE COMPRESSION STRENGTH OF A LAMINATED PANEL

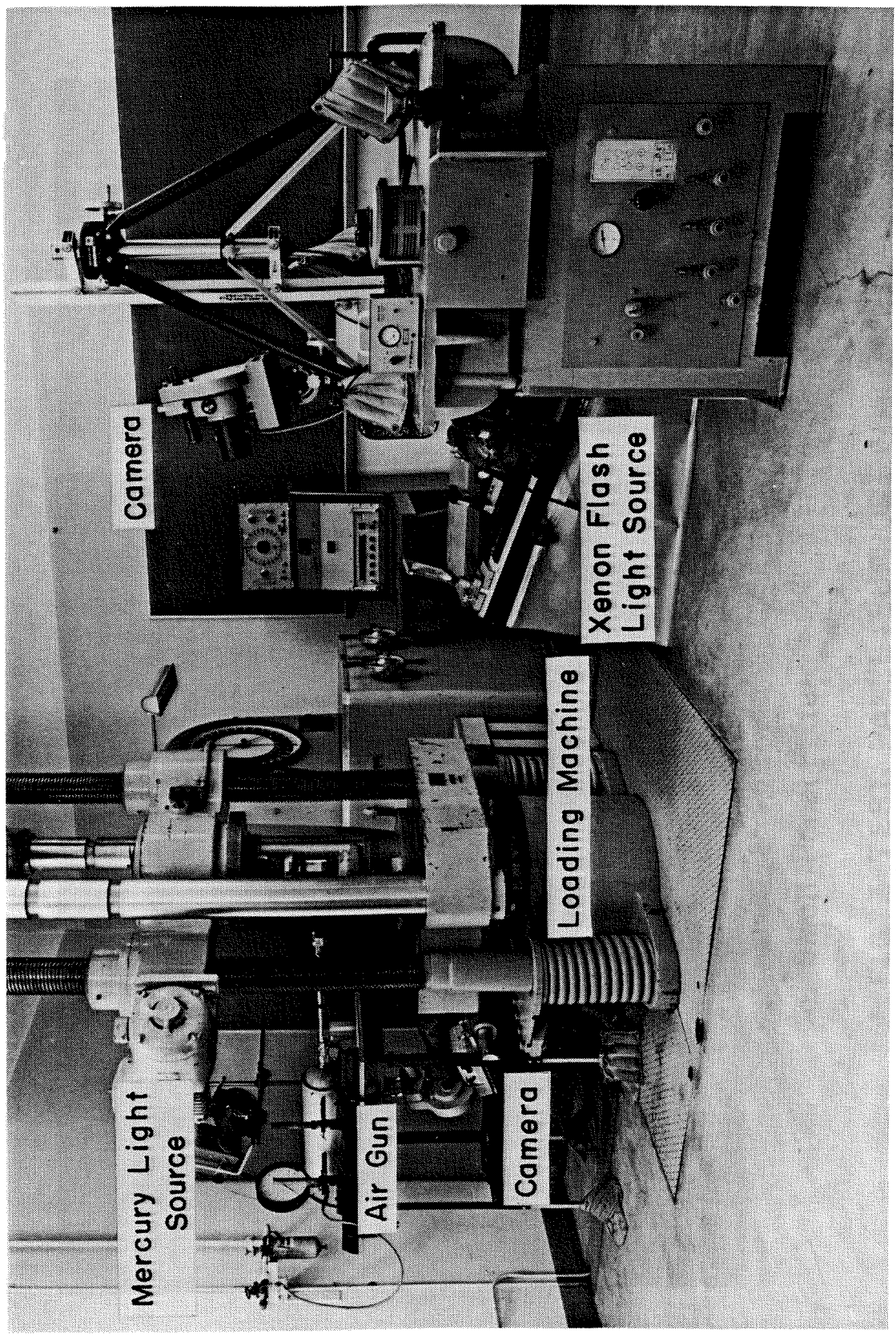

FIG. 2 IMPACT AND RECORDING TEST SET UP

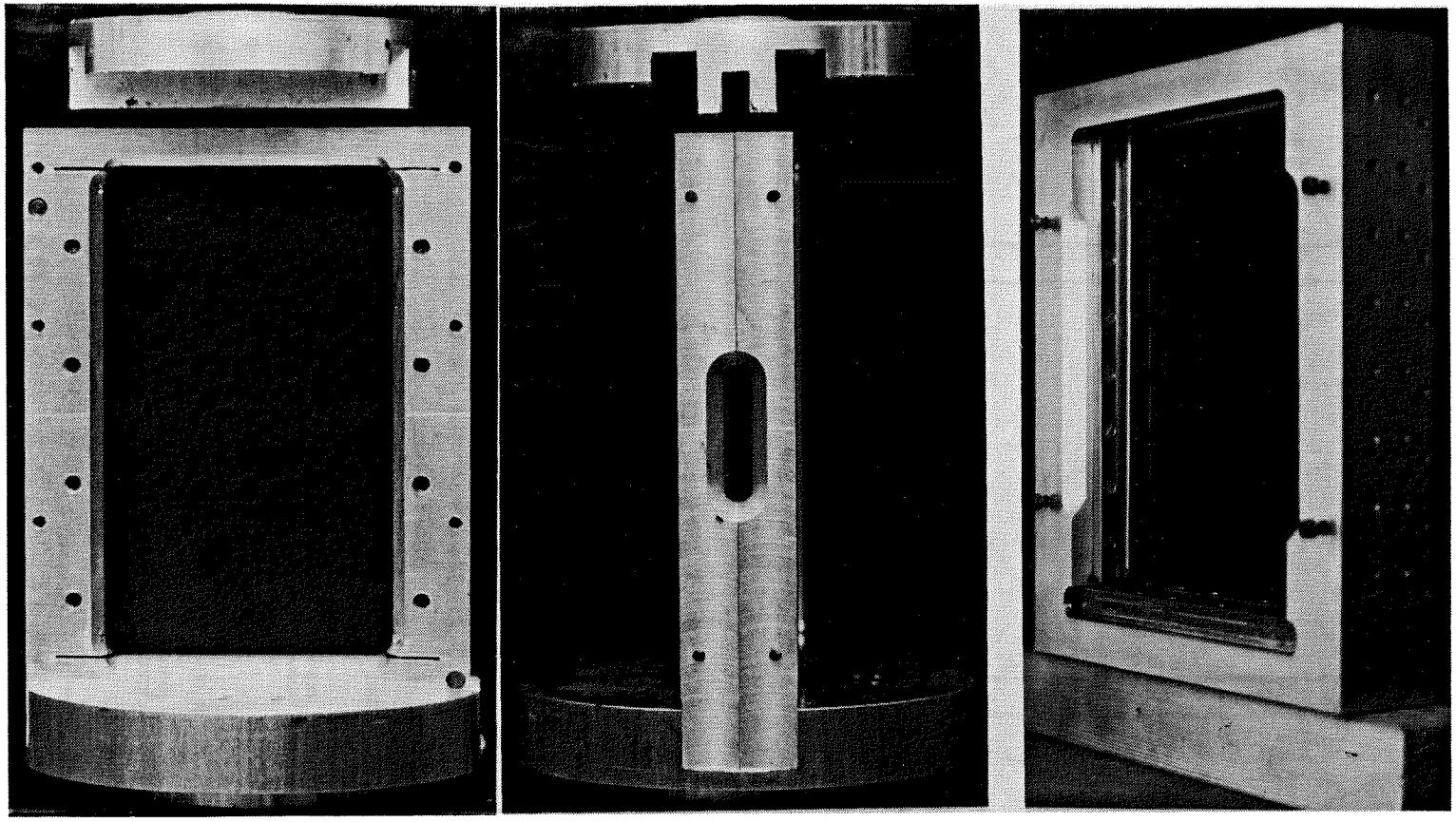

a. Small Panel Fixture b.Large Panel Fixture

FIG. 3 TEST PANEL SUPPORT FIXTURE

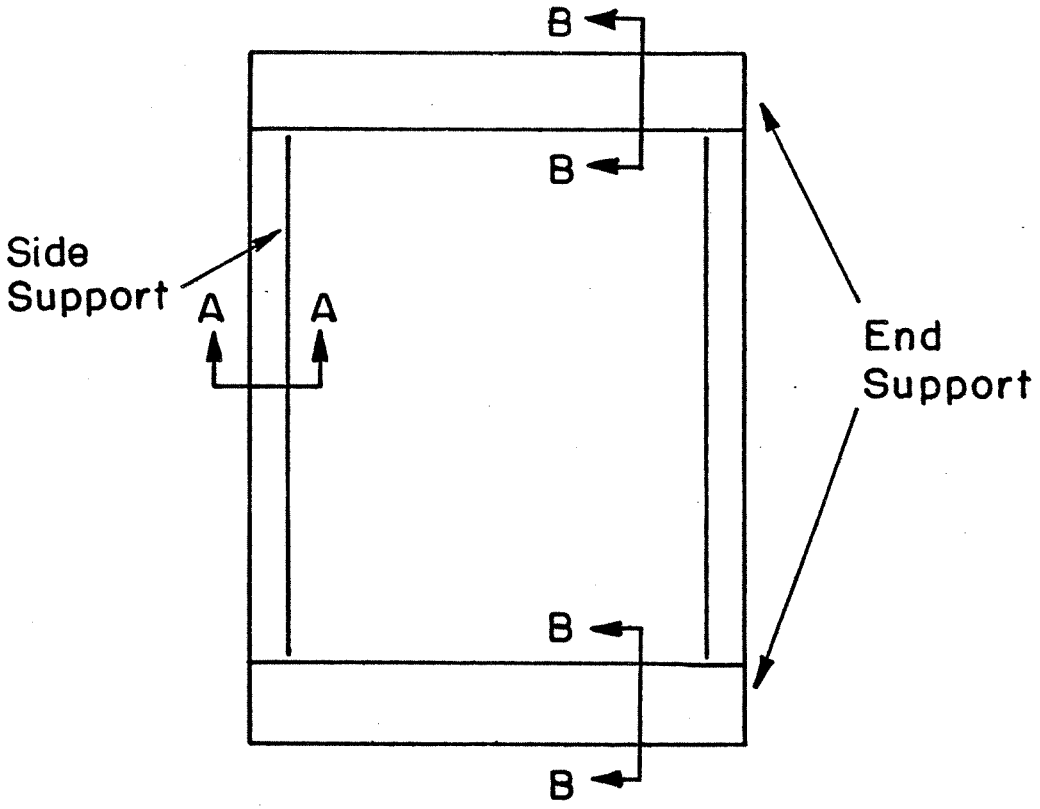

Section B - B

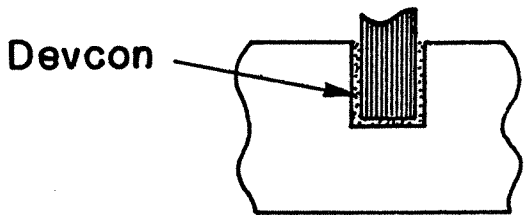

Section A - A

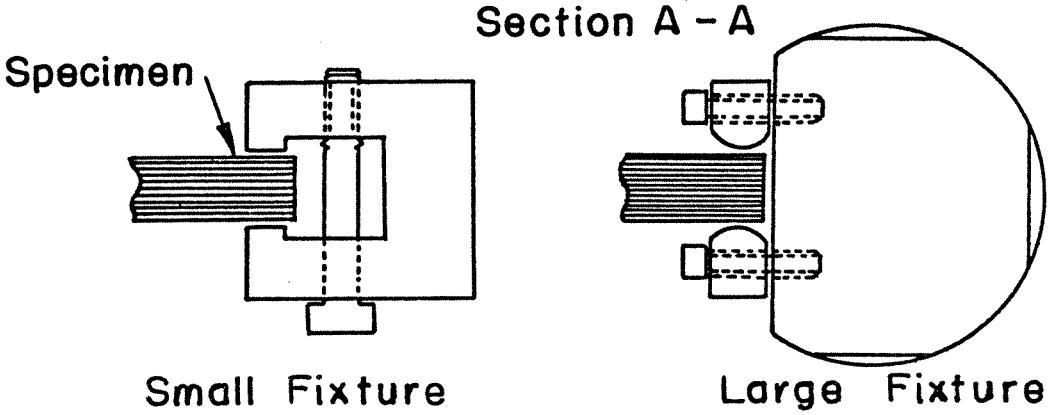

FIG. 4 TEST PANEL EDGE SUPPORTS

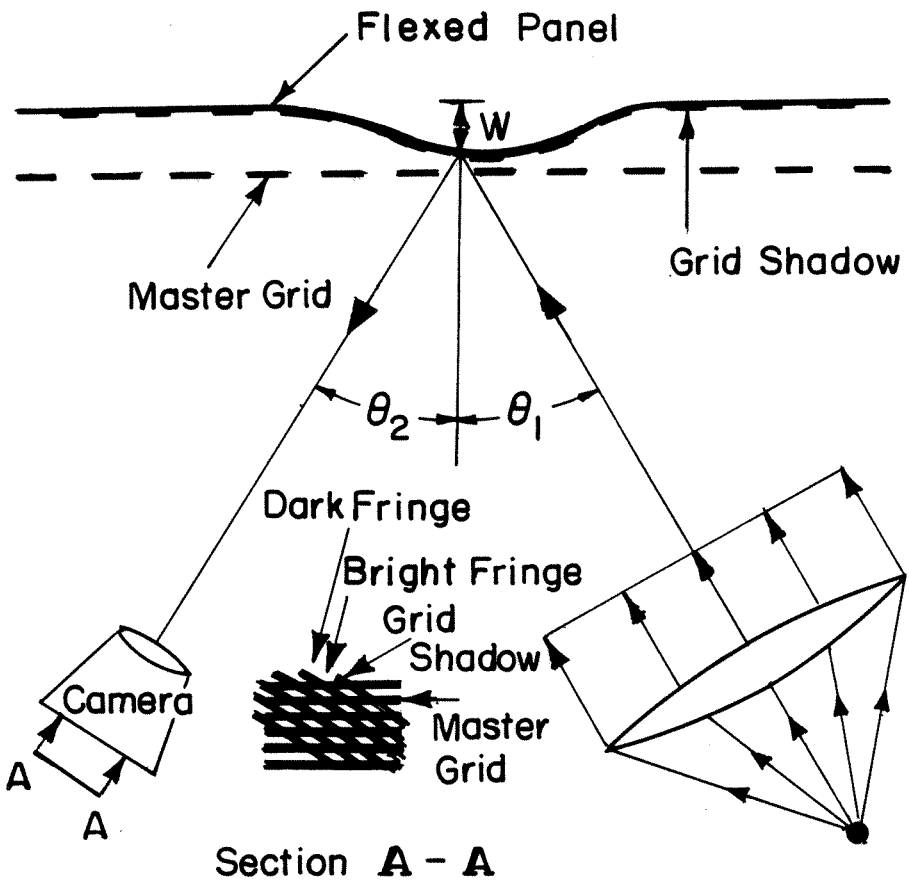

FIG. 5 SHADOW MOIRE OPTICAL SET UP

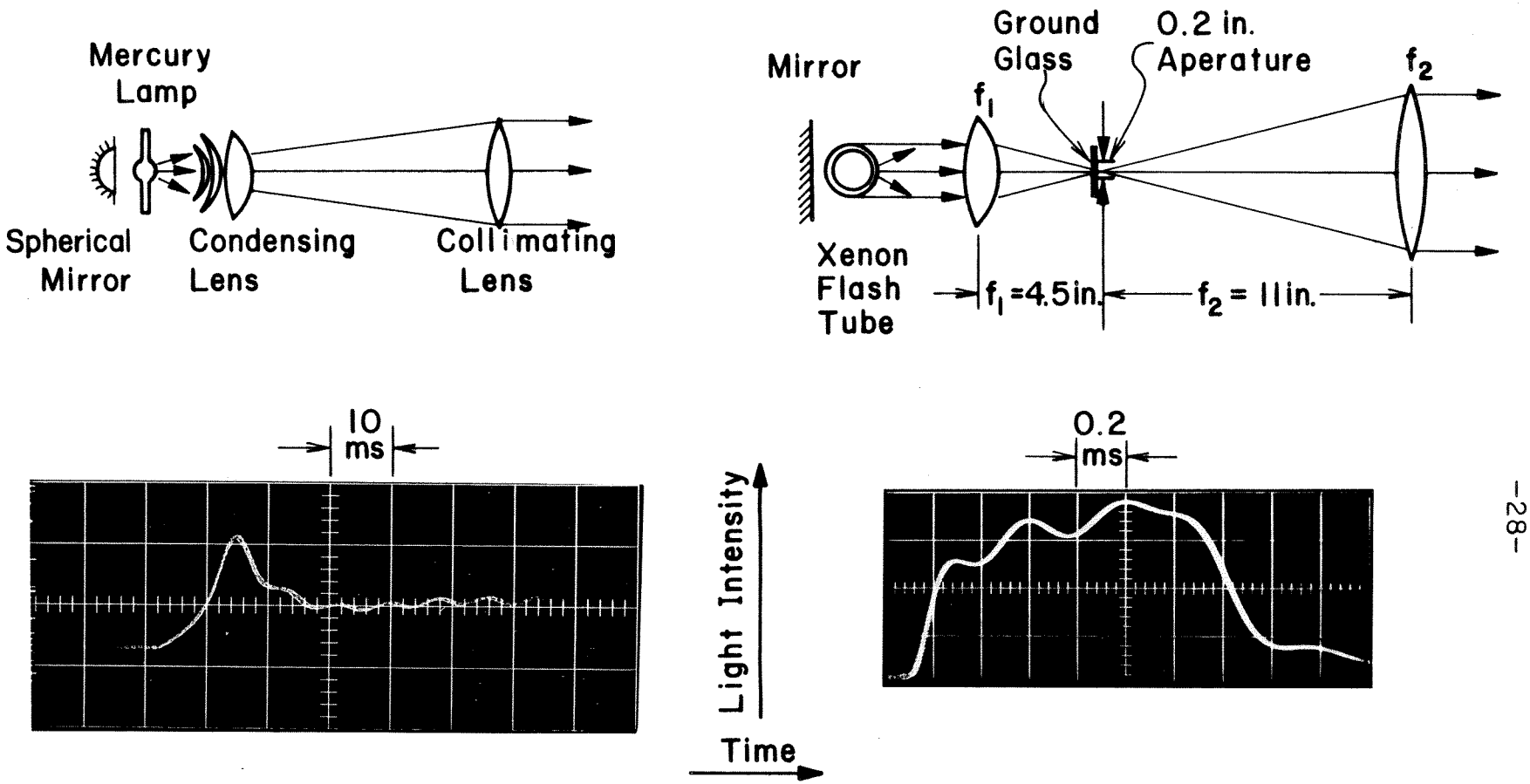

FIG. 6 OPTICAL ARRANGEMENT (UPPER PARTS) AND LIGHT INTENSITY HISTORY (LOWER PARTS) OF TWO LIGHT SOURCES.

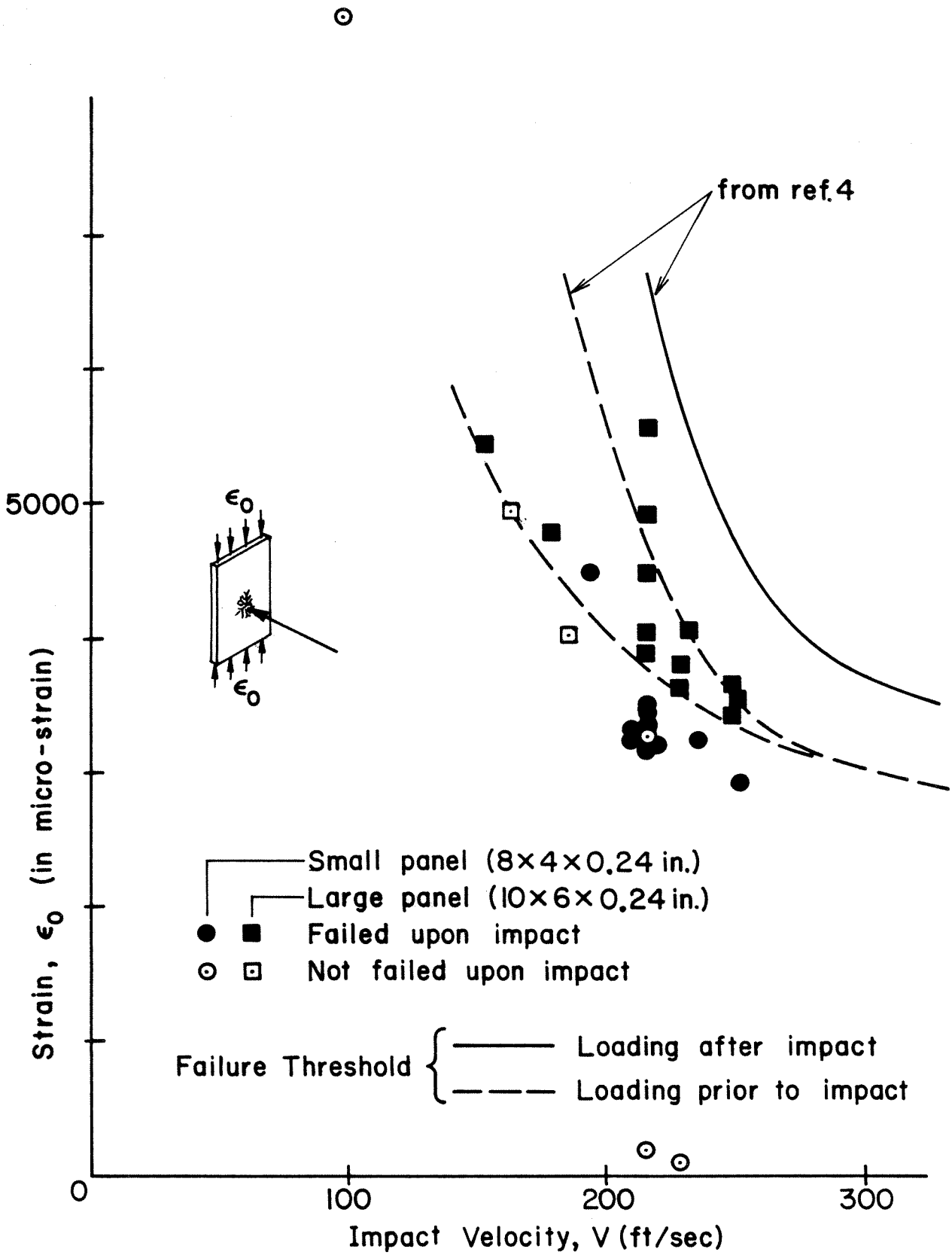

FIG. 7 IMPACT CONDITIONS FOR T300/5208 ORTHOTROPIC LAMINATE.

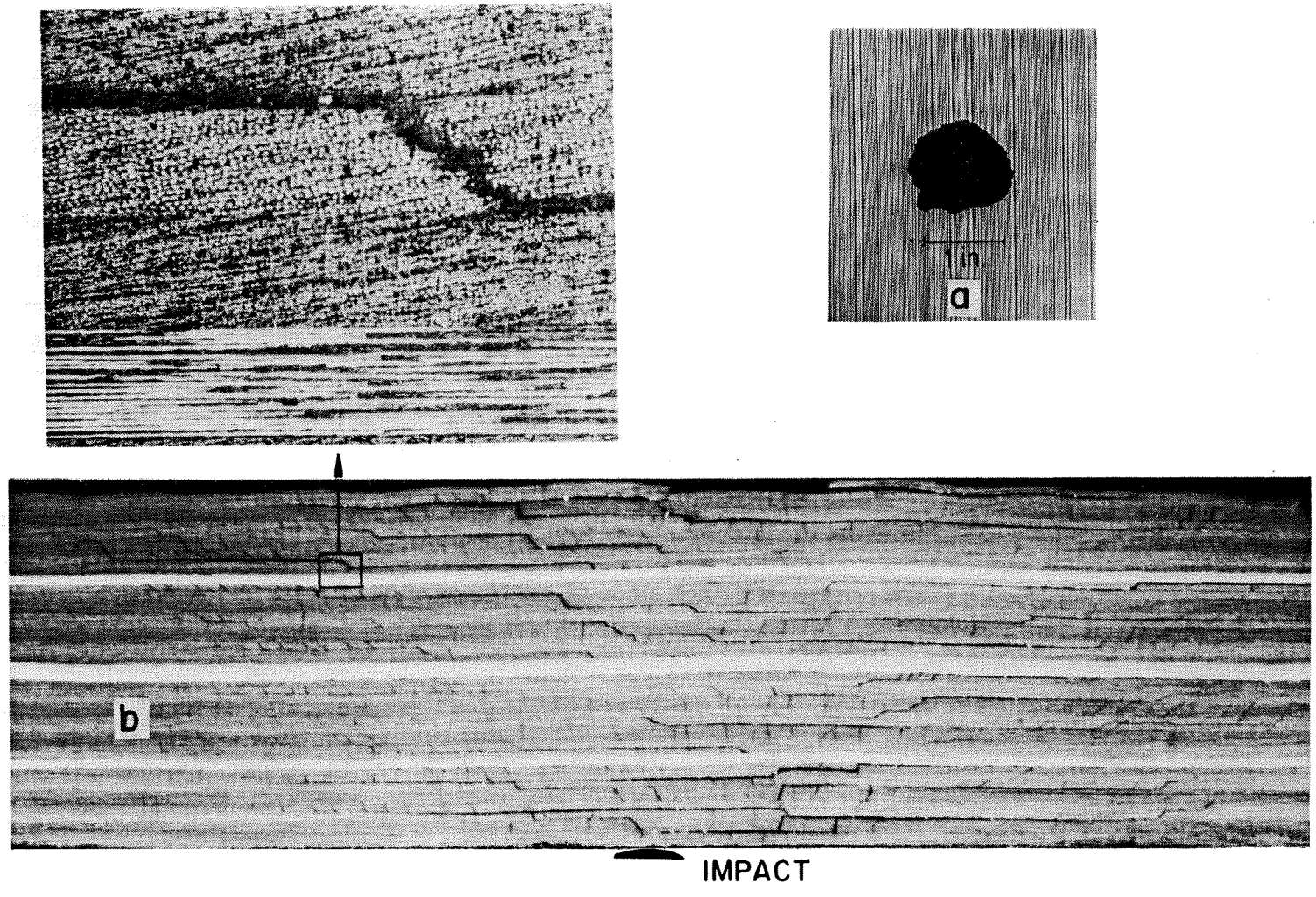

FIG. 8 IMPACT DAMAGE IN A 0.24 in. THICK Gr./EP. LAMINATE: (a) C-SCAN OF AN UNLOADED PLATE IMPACTED AT 250 ft/sec, (b) THROUGH-THE-THICKNESS HORIZONTAL SECTION OF THE PLATE IN (a)

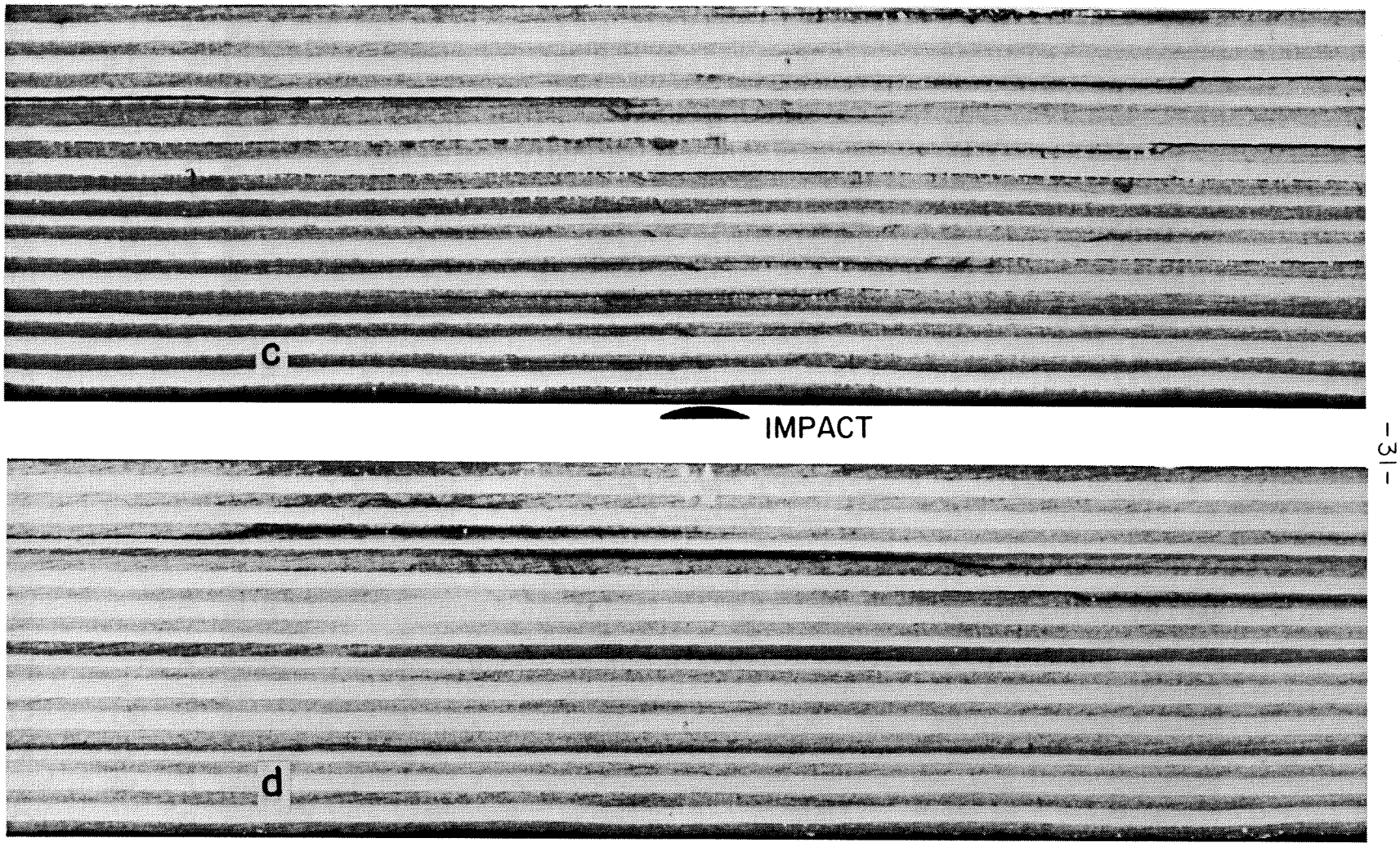

FIG. 8 CONT. (c) AND (d) - TWO VERTICAL SECTIONS, 0.5 in. APART, OF A PLATE LOADED TO ϵ_0=0.0035 AND IMPACTED AT 214 ft/sec.

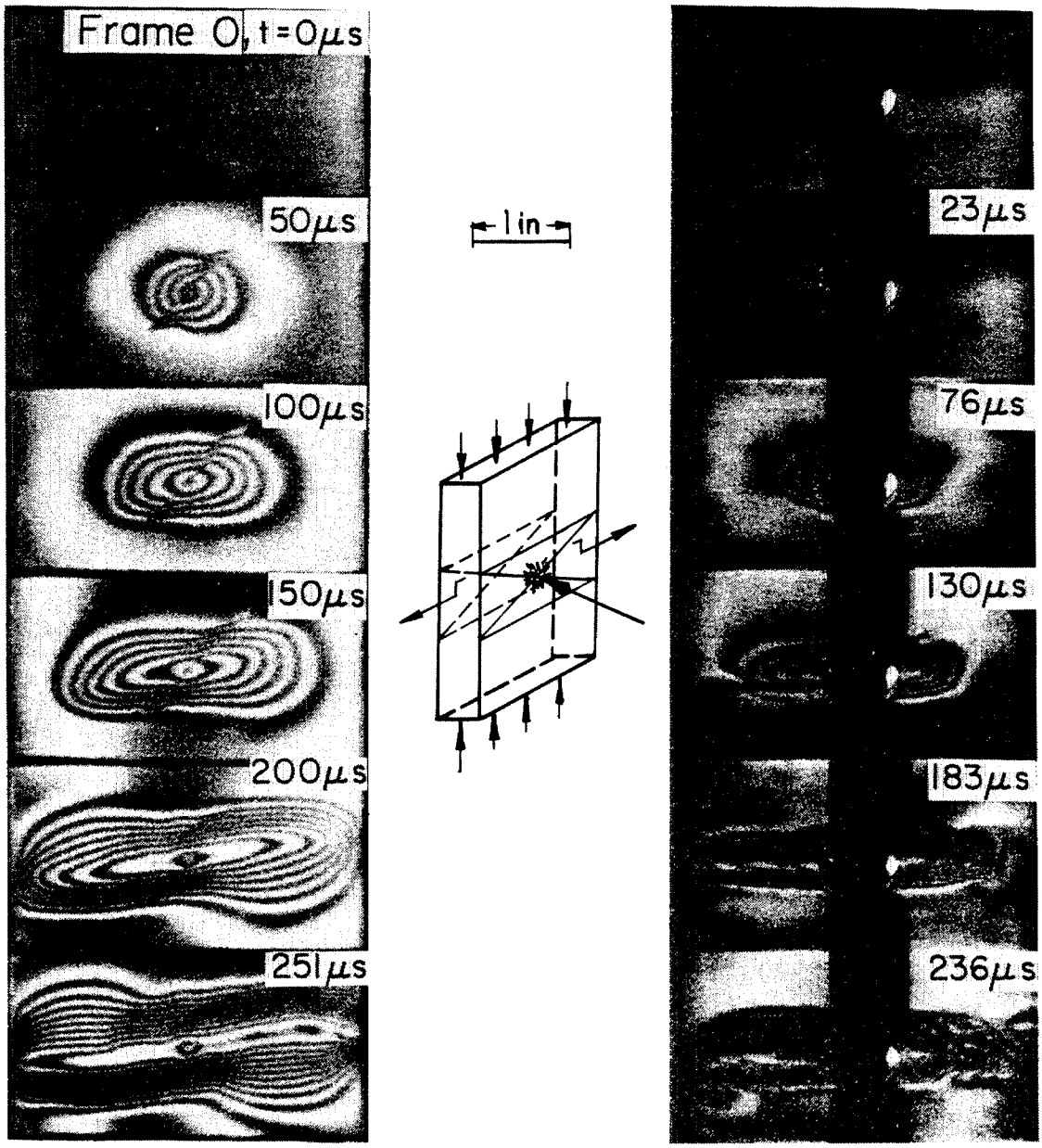

a) Back Surface

$\frac{W}{n} = 0.0126$ in.

b) Front Surface

$\frac{W}{n} = 0.0122$ in.

FIG. 9 SIMULTANEOUS BACK AND FRONT SURFACE MOIRE MOTION PICTURES SHOWING PLATE FAILURE. $\epsilon_0 = 0.00326$, V = 233 ft/sec

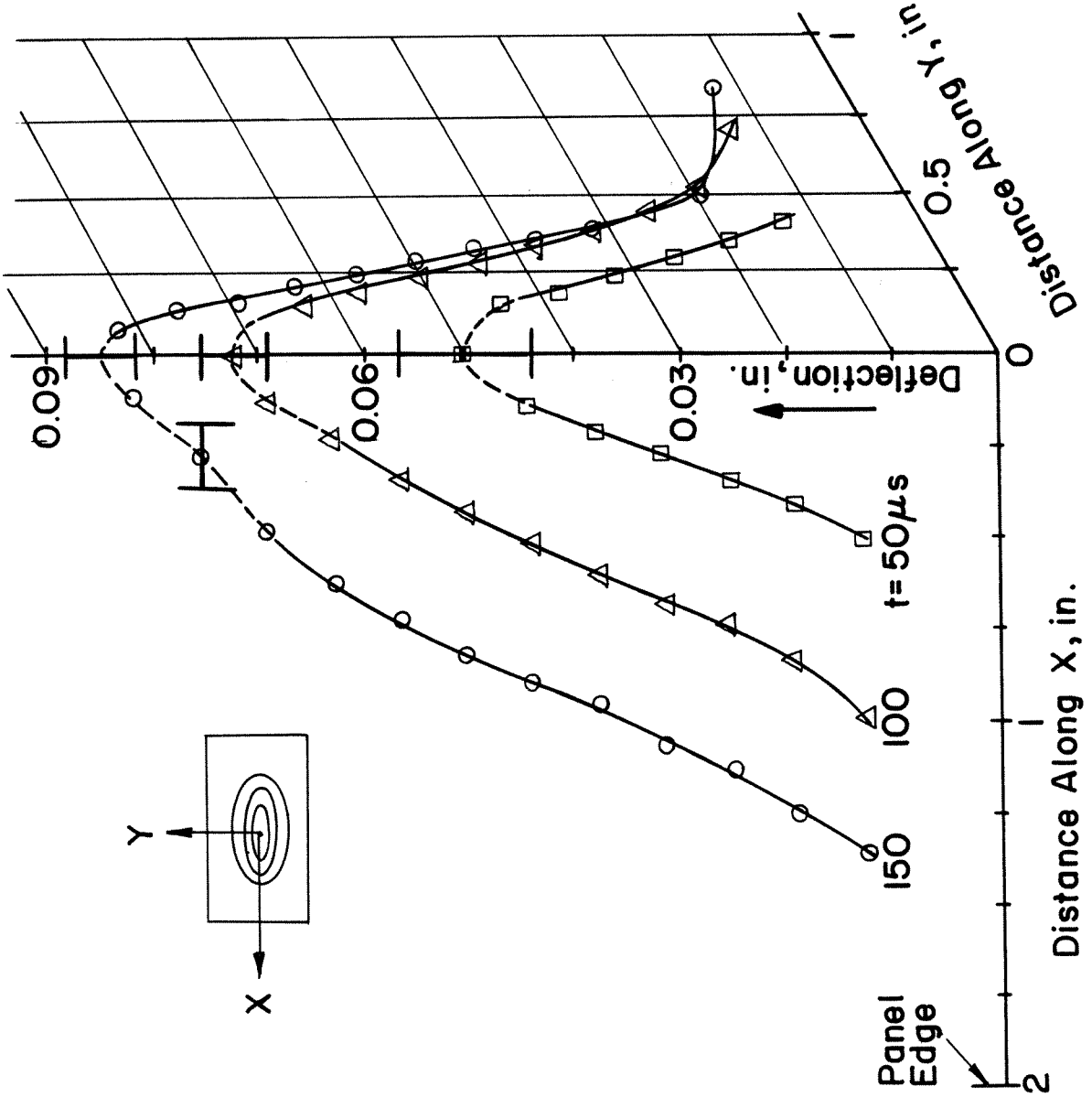

FIG. 10 OUT OF PLANE DISPLACEMENT FOR THE PANEL IN FIG. 9a

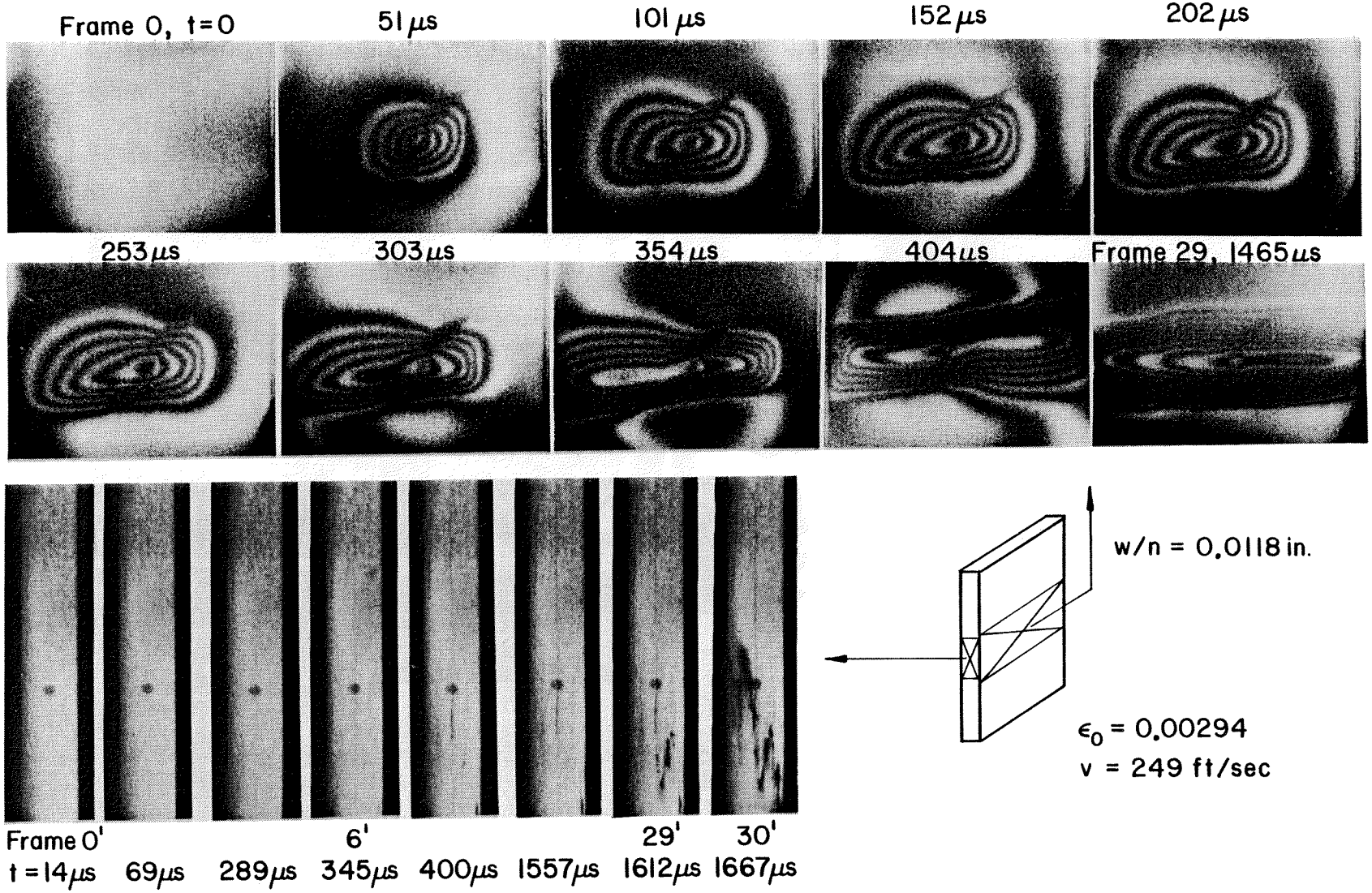

FIG. 11 SIMULTANEOUS BACK SURFACE (UPPER PRINTS) AND SIDE VIEW MOTION PICTURES

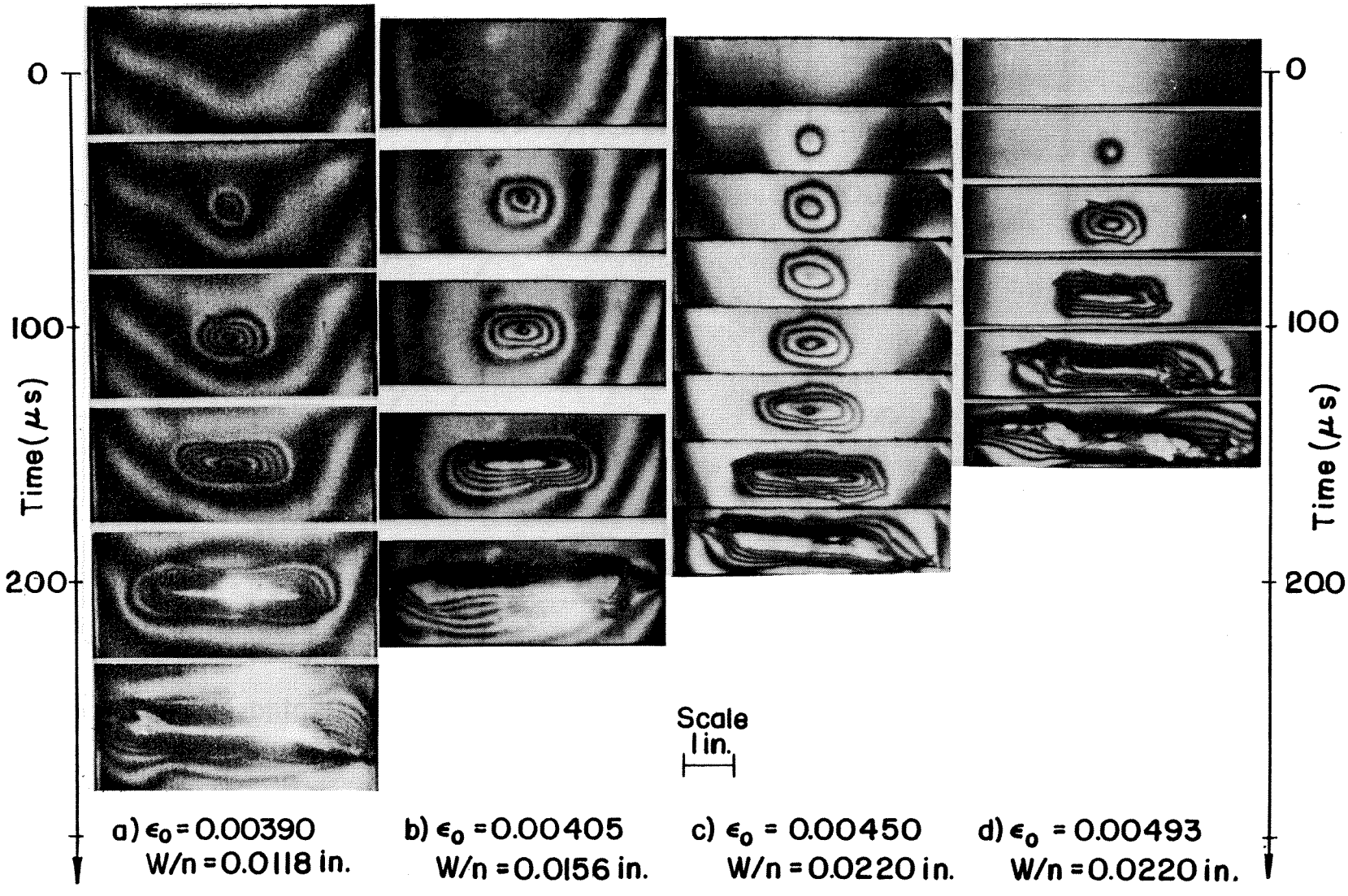

FIG. 12 DAMAGE PROPAGATION UNDER DIFFERENT LOADING, V = 214 ft./sec.

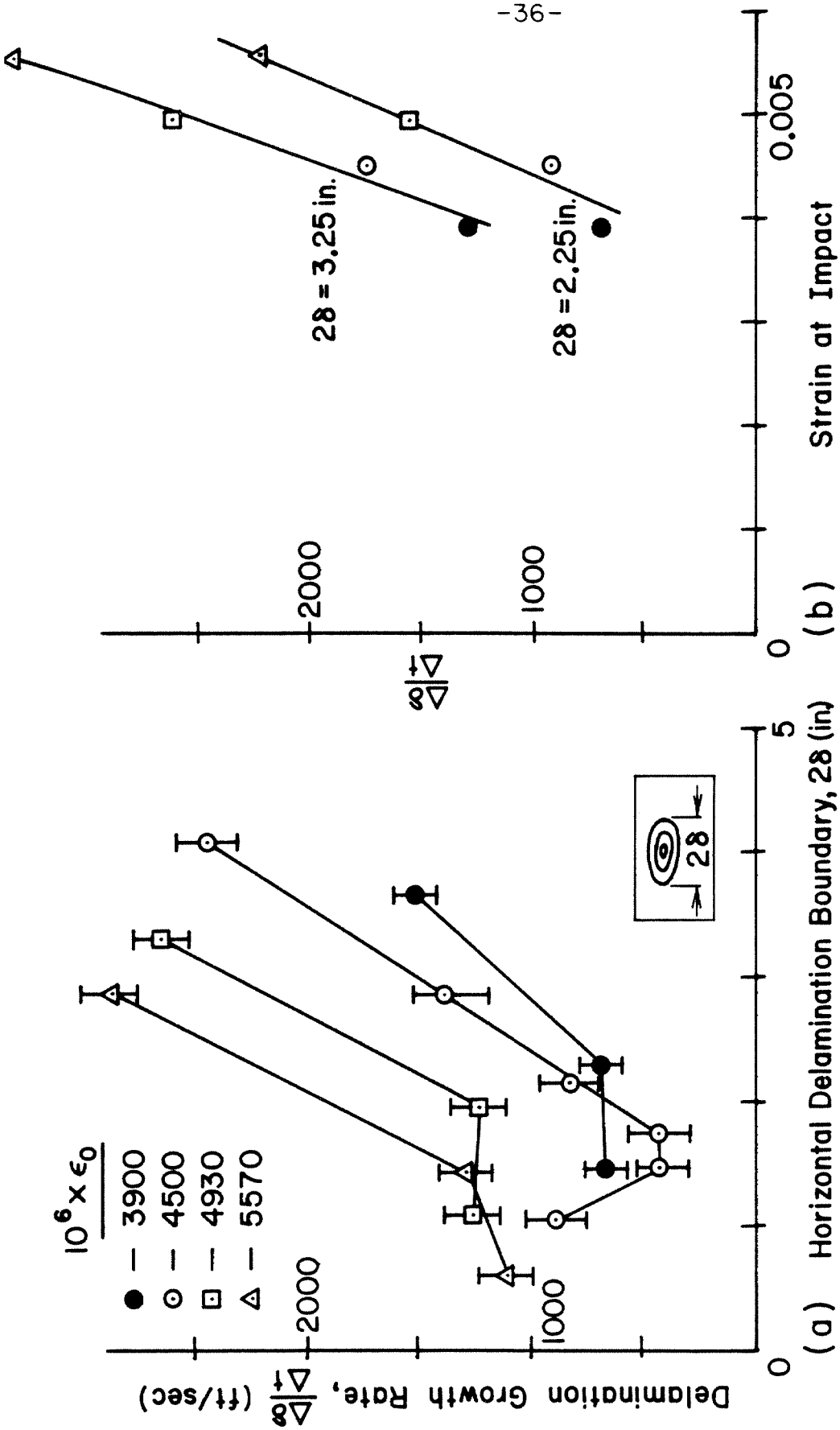

FIG. 13 DELAMINATION GROWTH RATE AS A FUNCTION OF DELAMINATION SIZE AND LOAD.

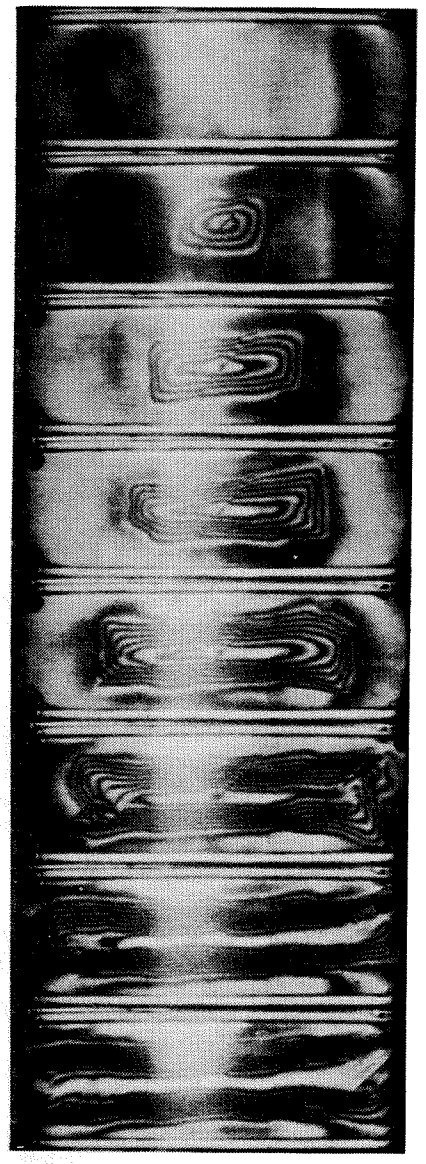

FIG. 14 A "RECTANGULAR" TYPE DAMAGE BOUNDARY

$w/n = 0.0165$ in., $\Delta t = 55.6 \mu s$

$\epsilon_0 = 0.00356$, $V = 248$ ft/sec

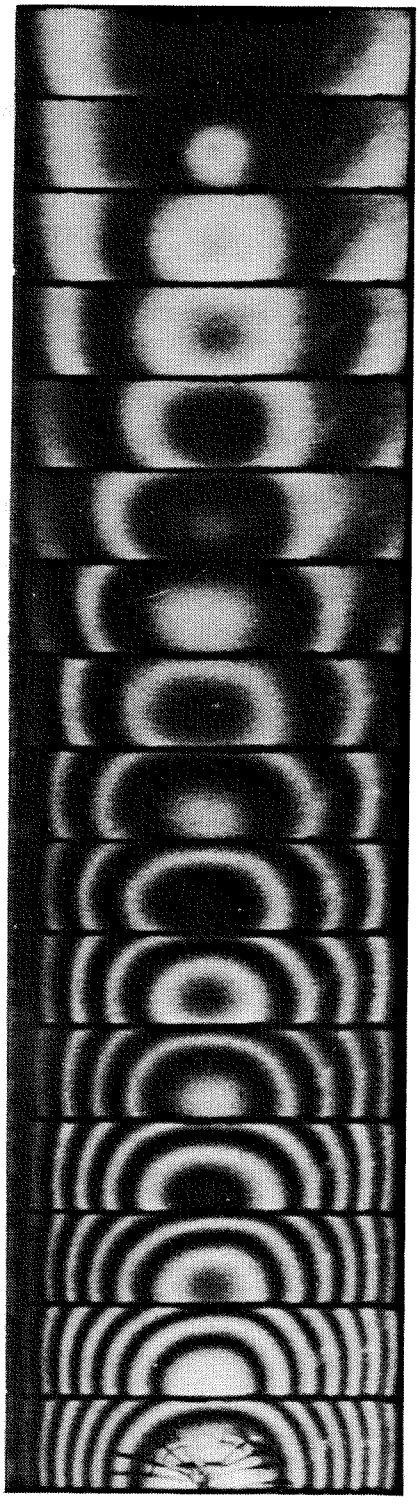

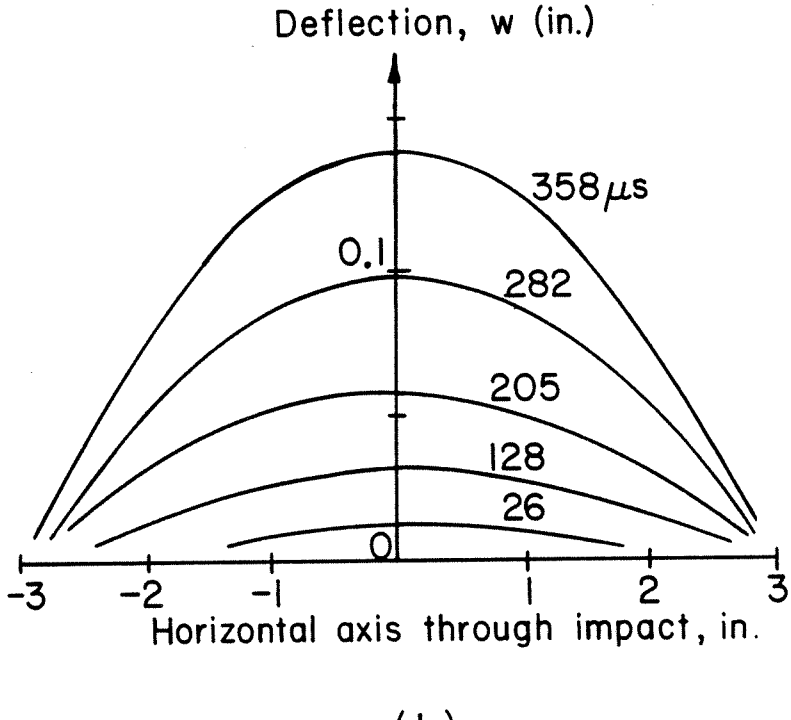

(b)

(a) w/n = 0.022 in., $\Delta t = 25.6\mu s$

$\epsilon_0 = 0.00545$, V = 152 ft/sec

FIG. 15 FAILURE DUE TO GLOBAL PANEL RESPONSE (a) BACK-SURFACE, (b) DEFLECTION

CHAPTER 2

MODELLING OF FAILURE BY DELAMINATION BUCKLING IN COMPOSITE PLATES

ABSTRACT

When low-speed objects impact composite laminated plates, damage may result. Under simultaneous in-plane compression loading the damaged area may propagate to the undamaged area which can lead to a global failure of the plate at a load well below the design level. Impact experiments reported in chapter 1 have shown that one of the damage growth mechanisms is the coupled effect of delamination and buckling leading to further growth.

This failure process is modeled here assuming quasistatic conditions, wherein the local delamination stability, growth or arrest are governed by a fracture mechanics-based energy release rate criterion. Various degrees of problem simplifications are employed. In the most sophisticated treatment it is assumed that the damage area has an elliptical shape.

The analysis is developed in a general manner, but emphasis is placed on the conditions that simulate impact damage. It was found that the proposed model is capable of describing the conditions for damage growth as well as the damage growth behavior observed in impact tests, and therefore can be used as a guide for impact damage tolerance improvements.

TABLE OF CONTENTS

NOMENCLATURE

A_3 = Midplane transverse deflection in section 3

a,b = Delamination major and minor axis, respectively

b_0 = Initial minor axis

$a^*, b^*, b^*_0 = \dfrac{(a, b, b_0)}{h\,\Gamma_0^{*-1/4}}$

$D_i = \dfrac{Et_i^3}{12(1-\nu^2)}$ = Bending rigidity in the i^{th} section

E = Young's Modulus

G = Strain energy release rate (s.e.r.r.) per unit area

$\overline{G} = \dfrac{G}{Et^5\,L^{-4}\,(1-\nu^2)^{-1}}$

G_a.....G_e = s.e.r.r. associated with models a.....e

G^a, G^b = s.e.r.r. with b fixed and with a fixed, respectively

h = Delamination thickness

$\overline{h}$ = h/t

L = Total length of plate

l = Delamination length

l_0 = Initial film length

$l_1 = (L-l)/2$, $l_2 = l_3 = l$

l_A , l_B = Significant film lengths

l_{a^*}, l_{e^*} = Delamination length which maximizes G_a and G_e, respectively

$l_{e^{**}}$ = Delamination length which minimizes G_e

$$\bar{l}, \bar{l}_{a^*}, \bar{l}_{e^*}, \bar{l}_{e^{**}} = \frac{(l, l_{a^*}, l_{e^*}, l_{e^{**}})}{L}$$

$$l^*, l^*_0 = \frac{(l, l_0)}{h\,\Gamma^*_0{}^{-1/4}} \quad , \quad l^*_A = 3.376 \quad , \quad l^*_B = 2.221$$

P_i = Total load in i^{th} section

r = Delamination radius

r_0 = Delamination radius introduced in stage ii

$$r^*, r^*_0 = \frac{(r, r_0)}{h\,\Gamma^*_0{}^{-1/4}}$$

t = Total plate thickness , $t_1 = t$, $t_2 = t-h$, $t_3 = h$

U = Strain energy

U_i , U_{ii} , U_{iii} = Strain energy for three different stages

$$\bar{U} = \frac{U}{E\,T^5\,L^{-3}\,(1-\nu^2)^{-1}}$$

$$\bar{\bar{U}} = \frac{U}{\left[\frac{\pi E h a b}{2(1-\nu^2)^2}\left(\frac{h}{b}\right)^4\right]}$$

$u_i = \frac{l_i}{2}\sqrt{P_i/D_i}$, $i = 1-3$, – Normalized total load in i^{th} section

Γ_0 = Fracture energy per unit area

$$\Gamma^*_0 = \frac{\Gamma_0}{Eh[2(1-\nu^2)]^{-1}}$$

δ = End deflection of delamination

ε_0 = Loading strain

$\varepsilon_i = \frac{P_i}{Et_i}$, $i = 1-3$ – Midplane (membrane) strain in i^{th} section

$\varepsilon_L = \frac{\pi^2}{3(1-\nu^2)}(\frac{t}{L})^2$ = Buckling strain of plate

$\varepsilon_{cr} = \frac{\pi^2}{3(1-\nu^2)}(\frac{h}{l})^2$ = Buckling strain of delamination

$\bar{\varepsilon}_0, \bar{\varepsilon}_i, \bar{\varepsilon}_{cr} = \frac{(\varepsilon_0, \varepsilon_i, \varepsilon_{cr})}{\varepsilon_L}$, $i = 1-3$

$\bar{\varepsilon}_{cr} = (\frac{\bar{h}}{\bar{l}})^2$

$\varepsilon^*_0 = \frac{\varepsilon_0}{(1-\nu^2)^{-1}\,\Gamma^{*1/2}_0}$, $\varepsilon^*_{0A} = 0.866$, $\varepsilon^*_{0B} = 1.000$

$\eta = u_3 - \pi$ = Expansion parameter

Θ = End rotation of delamination

$\bar{\Theta} = \Theta L/t$

$\lambda = (1-\nu^2)\varepsilon_0(b/h)^2$ = Load–geometry parameter

$\xi \equiv a/b$ = Delamination aspect ratio

ν = Poisson's ratio

2.1 INTRODUCTION

The mechanisms of strength degradation resulting from low-velocity impact on compressively loaded graphite/epoxy laminates have been investigated in chapter 1. It was found that the failure process can be divided roughly into two phases. In the first phase, which was observed to occur in less than 25μs (the resolution time of the camera), the plate is impacted, and the resulting response causes interlaminar separation. In the second phase, the damage spreads to the undamaged area of the plate through a combination of delamination buckling and further delamination, leading to a global failure of the structure. It is this phase which is of concern in this work. In the following, an analytical model of this damage growth mechanism is developed with the ultimate goal of determining the factors controlling damage growth or arrest.

It is assumed that damage exists in the plate as shown in fig. 1. The damaged area, corresponding to a region which has been delaminated from the plate after impact, is characterized by two parameters, l and ω. The dimensions of these parameters are large compared to the delamination thickness, h, but small compared to the plate size. The problem is further simplified by assuming an analytically tractable elliptical shape for the delamination boundary. The plate may be initially unloaded or, under an in-plane compression when the delamination appears. In either case, the analysis will study the growth (under load) of the damage area. Quasistatic conditions will be assumed, and the analysis will draw on the large-deflection plate theory as well as on a fracture criterion.

In order to elucidate the dominant physical phenomenon in a readily tractable analytical manner it appears prudent to deal first with a geometrically simpler situation than the full plate problem illustrated in fig. 1. Therefore, the

analysis will first deal with the one-dimensional plate analogue represented by the cross-section in fig. 1 in which geometry and loading are considered to be invariant along the coordinate normal to the plane of the figure. In formulating the one-dimensional model, various degrees of sophistication will be employed, all of which possess an exact closed-form solution within the assumptions of technical beam/plate theory. The results of the one-dimensional model will serve in formulating the more complicated elliptical (two-dimensional) model and also in providing a basis for comparison.

The problem starts when the compression load is sufficiently large to cause buckling of the delamination area. When buckling does occur, stresses are set up at the delamination boundary which tend to spread out the delamination. The analysis then determines the conditions (load, delamination geometry etc.) for stability, growth or arrest of the delamination by examining the change in the strain energy of the system with increasing delamination size and determining whether this change is sufficient to create the new surface. Growth of the delamination is assumed to occur in its own plane in keeping with the laminate character of the layered composite. Yet, for simplicity reasons, the properties of the plate are assumed homogeneous, isotropic and linearly elastic.

The fracture resulting from a compressive load applied parallel to the crack (or flaw) plane has not been recognized or understood as the other types of failure usually encountered in fracture mechanics, and only few treatments on this subject are given in the literature [1-10]. A brief review of the works that are related, to some degree or another, to the present one follows.

The first observation on the effect of a compressive load on the fracture process in a cracked body is due to Guernsey and Gilman [1] and Svensson [2]. Both references have considered a cleavage-type specimen as shown in the left part of

sketch 1. By adding a sufficient amount of compressive load Q to the splitting loads P in sketch 1, they were able to keep the crack growing in its own plane which otherwise will deviate away (see the right hand side in sketch 1).

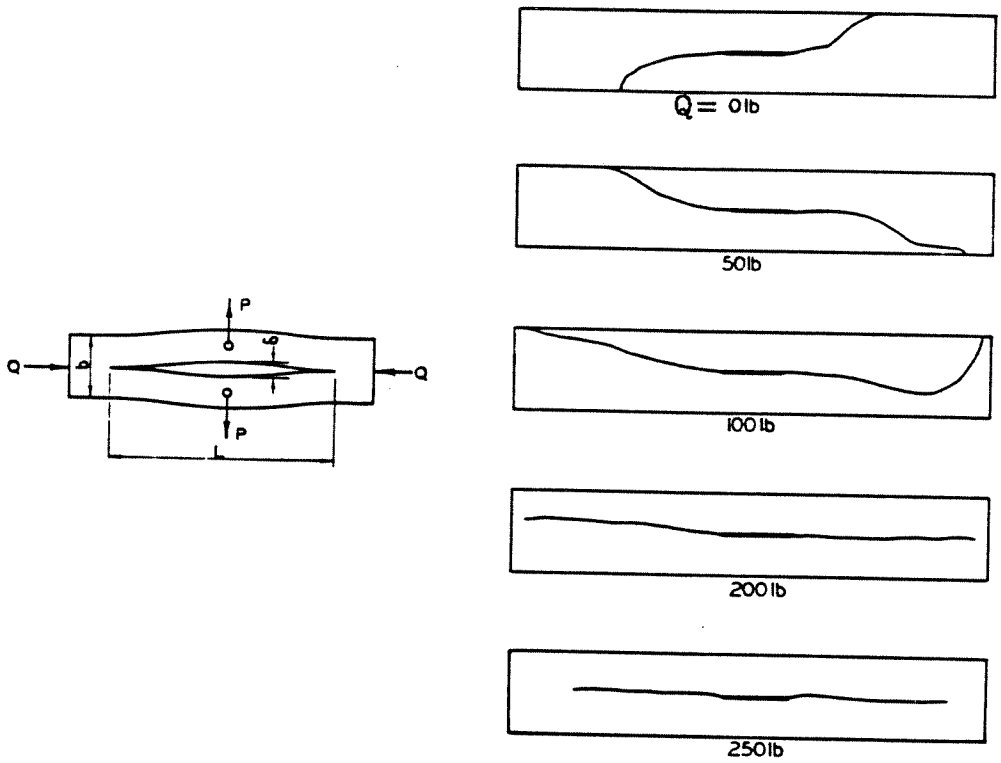

SKETCH 1 The Effect of Compressive Load Q on Crack Growth Direction (from [2])

Kachanov considered the sudden detachment of an internal layer of a glass-fiber pipe subjected to an external pressure [3] and that of a layer attached to a compressively loaded column [4]. Kachanov based his fracture criterion on the difference in the energy levels of the layer before and after the detachment; when this energy difference is larger than the energy required to create the new surface, detachment can take place. No fracture criterion was developed in [3 ,4], however, for the post-buckling configuration of the detached layer. In [5], a fracture type specimen similar to the one shown in sketch 1 (with the load P

being set to zero) was proposed. The split beams in this specimen were made imperfect in order to obtain splitting stress at the crack tip for loads below the buckling load of the perfect column. Reference 6 studied the postbuckled through-width delamination in a laminated coupon by employing the finite-element method to calculate the stress distribution around the crack tip. Finally, the failure of a laminated structure resulting from a compressive load applied in the delamination or damage plane was considered experimentally in references 7-10. The works in these references include static and fatigue loading of an impact-induced delamination or simulated delamination.

2.2 ONE-DIMENSIONAL MODEL

As a first step toward the analysis of the two-dimensional model shown in fig. 1, the development of the delamination/buckling model for the relatively simple one-dimensional analogue represented by the cross-section in fig. 1 will be carried out. Depending upon the degree of sophistication in treating this problem, further approximations may be considered. In fig. 2a, the unbuckled portion of the plate has been made infinitely thick; this is called the "thin film" model and is treated in section 2.2.1. In the most general case, fig. 2e, the delamination thickness may be on the same order of magnitude as the other thicknesses involved. This case is treated in section 2.2.2. The rest of the models in fig. 2, i.e. the "thick column" (fig. 2b), the "multiple delamination column" (fig. 2c) and the "symmetric split" (fig. 2d) are derived in section 2.2.3 as limit cases of the general case. The analysis for the "thin film" model is carried out first in detail since the results are quite simple and illustrative of the results for the more complete models.

2.2.1 Thin Film Delamination

Consider the three stages in the thin film delamination and buckling shown in fig. 3. The delaminated film of thickness h and length ℓ is part of an infinitely thick medium characterized by Young's modulus E and Poisson's ratio ν. Stage i represents the unstressed medium while stage ii denotes the uniformly compressed medium (strain = ε_0). Stage iii differs from ii in that the delamination has buckled. The conditions for growth of the delamination are determined by examining the change in stored energy of the system as the delamination spreads. If the elastic energy change in that process equals or exceeds the energy required to create a unit of new delamination, then growth will take place. If growth does take place, it is of interest to examine whether or not the

growth is arrested at a later stage.

The strain necessary to cause buckling, ε_{cr}, and the post buckled shape of the film can be easily calculated if use is made of the usual assumptions of technical beam/plate theory. The buckling displacements are assumed reasonably small. This yields

$$\varepsilon_{cr} = \frac{\pi^2}{3(1-\nu^2)}\left(\frac{h}{l}\right)^2 \tag{1}$$

$$v = \frac{A}{2}(1 + \cos 2\pi x/l) \tag{2}$$

The amplitude A is determined by the condition that in going from stage ii to iii the length l of the delaminated section remains unchanged, and the membrane stress in the buckled laminate is the same as the buckling stress. These conditions lead to

$$(\varepsilon_0 - \varepsilon_{cr})(1-\nu^2)l = \int_{-l/2}^{l/2} \frac{1}{2}\left(\frac{dv}{dx}\right)^2 dx \tag{3}$$

or

$$A^2 = (\varepsilon_0 - \varepsilon_{cr})\left(\frac{2l}{\pi}\right)^2 (1-\nu^2) \tag{4}$$

The strain energy in the buckled layer consists of the membrane energy and the bending energy. It is given by (on a per unit width basis)

$$U_{iii} = \frac{Ehl}{2}\left[\varepsilon_{cr}^2(1-\nu^2) + \nu^2\varepsilon_0^2\right] + \frac{Eh^3}{24(1-\nu^2)}\int_{-l/2}^{l/2}\left(\frac{d^2v}{dx^2}\right)^2 dx \tag{5}$$

or

$$U_{iii} = \frac{Ehl(1-\nu^2)}{2}\left[2\varepsilon_0\varepsilon_{cr} - \varepsilon_{cr}^2 + \frac{\nu^2}{(1-\nu^2)}\varepsilon_0^2\right] \tag{6}$$

Next the energy release rate, G, is calculated for the condition that the length of the film changes from l to $l+\Delta l$. To distinguish the energy release rate in this

example from those encountered later on let us affix a subscript "a"; then

$$G_a = \lim_{\Delta l \to 0} \left[U_{III}(l) + \frac{1}{2}Eh\varepsilon_0^2 \Delta l - U_{III}(l+\Delta l) \right] \frac{1}{\Delta l} \tag{7}$$

which can be reduced to

$$G_a = \frac{Eh(1-\nu^2)}{2}(\varepsilon_0 - \varepsilon_{cr})(\varepsilon_0 + 3\varepsilon_{cr}) \tag{8}$$

Finally, the strain energy in the laminate corresponding to stage ii is given by

$$U_{II} = \frac{1}{2}Eh l \varepsilon_0^2 \tag{9}$$

The history of the strain energy of the "thin film" delamination can now be considered. There will be two different cases depending upon the time in the load history at which the delamination is introduced. The first case considered will be the one in which the delamination is introduced prior to inception of loading. Next the case of a delamination introduced while the plate is under compression load will be considered.

For the first case the strain energy increases quadratically with load (eq. 9) until ε_0 reaches ε_{cr} (fig. 4). At $\varepsilon_0 = \varepsilon_{cr}$ the laminate buckles and the strain energy increases in accordance with equation (6). This is shown in fig. 4 where ν has been chosen as 0.3 for plotting purposes. Since the stresses at the ends of the delamination (the delamination crack-tip) are considered to promote further splitting only after buckling has occurred, the question of delamination growth is of interest only for $\varepsilon_0 > \varepsilon_{cr}$. Equation 8 indicates a positive strain energy release only for $\varepsilon_0 > \varepsilon_{cr}$. Whether further delamination occurs depends, however, on the magnitude of the fracture energy Γ_0, which is defined as the energy required to produce a unit of new delamination. The dependence of the strain energy release rate, G_a, upon loading and delamination length (from (8)) is plotted in fig. 5. In order to generalize these results for arbitrary Poisson's ratio ν

and fracture energy Γ_0, the following normalizations were employed

$$\Gamma^*_0 = \frac{\Gamma_0}{Eh\,[2(1-\nu^2)]^{-1}}$$

$$\varepsilon^*_0 = \frac{\varepsilon_0}{(1-\nu^2)^{-1}\,\Gamma^{*1/2}_0} \tag{10}$$

$$l^* = \frac{l}{h\,\Gamma^{*-1/4}_0}$$

With the aid of fig. 5, the history of the delamination as a function of load can be determined. In this connection there are two values of load ε_0 (or ε^*_0) which have a special significance. The first, denoted by ε_{0A}, is the lowest value of strain for which the strain energy release rate can equal or exceed Γ_0. Referring to fig. 5, it is clear that this value is determined from the dual condition

$$G_a(l) = \Gamma_0 \quad \text{and} \quad \frac{\partial G_a}{\partial l} = 0 \tag{11}$$

which yields

$$\varepsilon_{0A} = \frac{\sqrt{3\Gamma^*_0}}{2(1-\nu^2)} \quad \text{or} \quad \varepsilon^*_{0A} = 0.866 \tag{12a}$$

and the corresponding delamination length

$$l_A = \frac{h(2\pi^2/\sqrt{3})^{1/2}}{\Gamma^{*1/4}_0} \quad \text{or} \quad l^*_A = 3.376 \tag{12b}$$

The other important strain, denoted by ε_{0B}, is the limit beyond which G_a exceeds Γ_0 as $l \to \infty$; it is given by

$$\varepsilon_{0B} = \frac{\sqrt{\Gamma^*_0}}{(1-\nu^2)} \quad \text{or} \quad \varepsilon^*_{0B} = 1.000 \tag{13}$$

For this value of load the strain energy release rate exceeds Γ_0 when the delamination length l^* falls in the range

$$l^*_B < l^* < \infty \qquad (l^*_B = 2.221) \tag{14}$$

By knowing these bounds, the length of the delaminated region can be found as a function of its initial length l_0 and the loading ε_0. This is illustrated by fig. 6 for normalized delamination length and loading. Suppose the initial delamination length, l_0, is such that $l^*_0 = l^*_A$. Then a load ε^*_0 increasing from zero will produce no further damage growth until $\varepsilon^*_0 = \varepsilon^*_{0A}$ in accordance with fig. 6 (cf. path 1). When ε^*_0 exceeds ε^*_{0A} stable delamination growth occurs such that for $\varepsilon^*_0 \to \varepsilon^*_{0B}$, $l^* \to \infty$. It is also clear that for $l^*_0 > l^*_A$ similarly stable growth occurs, though starting at values of ε^*_0 larger than ε^*_{0A} (cf. path 2). Now consider $l^*_B < l^*_0 < l^*_A$ (cf. path 3). Then no growth occurs until ε^*_0 is sufficiently large, corresponding to points C in figures 5 and 6. Thereafter, unstable crack growth occurs until the delamination reaches a new length corresponding to point D in figures 5 and 6, with only stable growth possible for a further increase in ε^*_0. Finally, consider $l^*_0 < l^*_B$. Then in accordance with path 4 in fig. 6 no growth occurs until ε^*_0 reaches a value larger than ε^*_{0B}. At this value of load the delamination becomes unstable.

From this type of calculation it is clear that a variety of behavior may be observed during a test on a delaminated structure. The behavior would be dependent upon the dimension of the damaged area as well as on the other parameters of the problem.

For the second case, consider the history of the strain energy if a delamination is introduced while the structure is under a load such that $\varepsilon_0 > \varepsilon_{cr}$. Prior to the introduction of the delamination the strain energy is given by (9). In fig. 4, let that strain be associated with point A. Now introduce a delamination (possibly by impact) and assume for the present that this process does not absorb energy from that stored in the system. Next buckling will occur and the new

equilibrium state has a lower energy corresponding to point B on the branch of the energy trace marked U_{III} in fig. 4. If the energy state at that instant is such that $G_a > \Gamma_0$ further delamination will occur. However, note that even if the energy release rate at point B in fig. 4 is not sufficient to allow further delamination growth, it may be possible that part of the energy released in the buckling process, denoted by ΔU in fig. 4, contributes to the further fracture process. This possibility could be reflected in a lowering of the load at which the damage spreads if the delamination is introduced while the structure is under load, as compared to the case where the delamination has existed prior to loading.

2.2.2 General Case

The analysis for the "general" case (fig. 2e) is treated in a similar manner to that of the 'thin film problem". The algebra is more cumbersome and it is necessary to evaluate the energy numerically. Cylindrical bending of the plate will be assumed along with the condition that the strain in the z direction is $\nu\varepsilon_0$. The coordinate systems for the separate parts of the structure are shown in figure 7. Each section is treated as a beam-column with compatibility and equilibrium enforced at the interfaces between sections. The specific conditions are:

Compatibility

Section 1

$$v_1 = \frac{dv_1}{dx_1} = 0 \qquad \text{at } x_1 = 0$$

$$v_1 = \delta \ , \ \frac{dv_1}{dx_1} = \Theta \qquad \text{at } x_1 = l_1$$

Section 2 and 3 (Assume Symmetry at $x_i = 0$)

$$v_i = \delta \ , \ \frac{dv_i}{dx_i} = \Theta \qquad \text{at } x_i = -l_i/2 \ , \ i = 2,3$$

Use of these conditions and the solution to the beam-column equation produces the following results:

$$v_i(x) = f_i(x)\Theta + g_i(x)\delta \quad , \; i = 1-3 \tag{15}$$

where f_i and g_i are given in the appendix.

Equilibrium $x_1 = l_1 \; , \; x_i = -l_i/2 \; , \; i = 2,3$

Shear: $S_1 = S_2 + S_3$ (16)

Axial Force: $P_1 = P_2 + P_3$ (17)

Moment: $M_1 = M_2 + M_3 - \frac{h}{2}P_2 + \frac{(t-h)}{2}P_3$ (18)

The shear condition (equation 16) (with the aid of (17)) produces a relation between δ and Θ;

$$\delta = \frac{\Theta l_1}{2u_1}\tan u_1$$

Substituting this relation in (15) produces the following results for the deflections:

$$v_1 = \frac{\Theta l_1}{2u_1 \sin 2u_1}(1 - \cos 2u_1 x_1/l_1) \tag{19a}$$

$$v_i = \frac{\Theta l_i}{2u_i \sin u_i}(\cos 2u_i x_i/l_i - \cos 2u_i/\{\cos u_i\}) \quad , \quad i = 2,3 \tag{19b}$$

where $u_i = \frac{l_i}{2}\sqrt{\frac{P_i}{D_i}}$ and $D_i = \frac{Et_i^3}{12(1-\nu^2)}$, $i = 1-3$, are the normalized total loads and bending stiffnesses of the separate sections, respectively.

The remaining conditions necessary for a solution involve the overall shortening of the plate. The assumption that during the transition from stage ii to stage iii the ends remain fixed (i.e. overall shortening is $\varepsilon_0 L$) results in the conditions, essentially analogous to (3);

$$\varepsilon_0 L = 2\varepsilon_1 l_1 + \int_0^{l_1} \left(\frac{dv_1}{dx_1}\right)^2 dx_1 + \varepsilon_2 l_2 + \frac{1}{2}\int_{-l_2/2}^{l_2/2} \left(\frac{dv_2}{dx_2}\right)^2 dx_2 + h\Theta \qquad (20)$$

$$\varepsilon_3 l_3 + \frac{1}{2}\int_{-l_3/2}^{l_3/2} \left(\frac{dv_3}{dx_3}\right)^2 dx_3 = \varepsilon_2 l_2 + \frac{1}{2}\int_{-l_2/2}^{l_2/2} \left(\frac{dv_2}{dx_2}\right)^2 dx_2 + t\Theta \qquad (21)$$

where ε_i is the membrane strain in the i^{th} segment, and is related to the axial load P_i. The membrane stresses and strains are given by :

$$(\sigma_x)_i = \frac{E}{(1-\nu^2)}(\nu^2\varepsilon_0 - \varepsilon_i) \quad , \quad (\sigma_z)_i = \frac{E\nu}{(1-\nu^2)}(\varepsilon_0 - \varepsilon_i)$$

$$(\varepsilon_z)_i = \nu\varepsilon_0 \quad , \quad (\varepsilon_x)_i \equiv -\varepsilon_i \quad , \quad i = 1-3$$

The strain energy in the system is then calculated as;

$$U = \left[(\sigma_x)_1(\varepsilon_x)_1 + (\sigma_z)_1(\varepsilon_z)_1 \right] t_1 l_1 + D_1 \int_0^{l_1} \left(\frac{d^2 v_1}{dx_1^2}\right)^2 dx_1 +$$

$$\frac{1}{2}\sum_{i=2}^{3} \left\{ \left[(\sigma_x)_i(\varepsilon_x)_i + (\sigma_z)_i(\varepsilon_z)_i \right] t_i l_i + D_i \int_{-l_i/2}^{l_i/2} \left(\frac{d^2 v_i}{dx_i^2}\right)^2 dx_i \right\} \qquad (22)$$

Consider now ε_1, ε_2, ε_3 and Θ as the desired unknown quantities, with load and section dimension specified. Combining equation (19) with (17), (18), (20) and (21) produces four equations in the four unknowns. The nondimensional versions of these equations are given in the appendix along with the energy.

The system of equations (A-1) to (A-4) in the appendix cannot be solved in a closed-form, and a numerical iterative scheme is employed. In order to start the iteration, an initial guess to the solution is required. The subject of finding such an initial guess is considered next.

Numerical Solution

Let u_3 represent the normalized load for section 3 as defined in the nomenclature. Starting from the observation that for $\Theta=0$ the post buckling normalized axial load is given by $u_3=\pi$, let us examine the equilibrium conditions for the more general case $\Theta \neq 0$. Figure 8 shows the axial load versus deflection for

specific values of Θ, as obtained from (19). Denote $v_3(0) - \delta$ by A_3 as in fig. 8; then the third of (19; i = 3) yields

$$A_3 = \frac{l_3\Theta\,(1 - \cos u_3)}{2u_3 \sin u_3} \quad . \tag{23}$$

In the lower part of this figure, $u_3 < \pi$ ($A_3 > 0$); this situation corresponds to a closing of the delamination against section 2 and is, therefore, of no current interest. Focusing attention on $u_3 > \pi$, it is seen in fig. 8 that u_3 decreases with decreasing Θ, approaching the Euler buckling load ($u_3 = \pi$) as $\Theta \to 0$. Use of this observation will be made later on. For the general case $\Theta \neq 0$, let

$$u_3 = \pi + \eta \quad , \quad 0 < \eta < \pi \tag{24}$$

Substitution of (24) in the equations determining ε_1, ε_2, ε_3 and Θ (cf. (A-1) to (A-4) in the appendix) and the third of (A-5) in the appendix results in eight equations with eight unknowns:

$$\bar{\varepsilon}_1 = \frac{[\,(1-\bar{h})\bar{\varepsilon}_0 + \bar{h}\bar{l}\bar{\varepsilon}_3^0\,]}{(1-\bar{h}+\bar{h}\bar{l})} + e_1 \quad , \quad u_1 = \frac{\pi(1-\bar{l})}{2}\sqrt{\frac{(\bar{\varepsilon}_1 - \nu^2\bar{\varepsilon}_0)}{(1-\nu^2)}}$$

$$\bar{\varepsilon}_2 = \frac{[\,\bar{\varepsilon}_0 - \bar{h}(1-\bar{l})\bar{\varepsilon}_3^0\,]}{(1-\bar{h}+\bar{h}\bar{l})} + e_2 \quad , \quad u_2 = \frac{\pi\bar{l}}{(1-\bar{h})}\sqrt{\frac{(\bar{\varepsilon}_2 - \nu^2\bar{\varepsilon}_0)}{(1-\nu^2)}}$$

$$\bar{\varepsilon}_3 = \bar{\varepsilon}_3^0 + e_3 \quad , \quad \bar{\varepsilon}_3^0 = (1-\nu^2)\bar{\varepsilon}_{cr} + \nu^2\bar{\varepsilon}_0 \tag{25}$$

$$\bar{\Theta} = \frac{\dfrac{-(1-\bar{h})}{\bar{l}}\left[\left(\dfrac{2u_1\bar{l}}{1-\bar{l}}\right)^2 - u_2^2(1-\bar{h})^2\right] - \dfrac{2\pi^2\bar{h}^3(1+a_2)\,(\bar{\varepsilon}_0 - \bar{\varepsilon}_{cr} + a_1)^{1/2}}{[\,3(1-\bar{h}+\bar{h}\bar{l})\,]^{1/2}}}{\dfrac{\bar{l}}{(1-\bar{l})}\dfrac{2u_1}{\tan 2u_1} + (1-\bar{h})^3\dfrac{u_2}{\tan u_2}}$$

$$\eta = \bar{\Theta}\frac{[\,3(1-\bar{h}+\bar{h}\bar{l})\,]^{1/2}}{[\,4\pi^2(\bar{\varepsilon}_0 - \bar{\varepsilon}_{cr} + a_1)\,]^{1/2}}$$

where terms defined in the nomenclature are used and the quantities e_1, e_2, e_3, a_1 and a_2 are given in the appendix. Let us seek a first approximation to the solution by assuming that Θ is small ($\Theta << 1$). This implies (from the discussion

of fig. 8) that η is also small, from which it follows that the quantities e_1, e_2, e_3, a_1 and a_2 are small. By temporarily assuming zero values for these quantities an initial solution to the set (25) can now be calculated, which, in turn, allows the calculation of the quantities e_1, e_2, e_3, a_1 and a_2. Successive iterations can now be carried out (about five) until sufficient convergence is achieved.

Next the strain energy is calculated from (A-6) from which, by means of simple numerical differentiation, the strain energy release rate can be found. The results obtained in this manner are shown in fig. 9, where the nondimensional strain energy release rate $\bar{G}_e$ for model e (fig. 2e) is plotted as a function of crack length for several loadings and section dimension. Consider a typical curve in fig. 9 which corresponds to a fixed load ratio, say $\bar{\varepsilon}_0 = 0.6$, and examine the characteristic behavior of $\bar{G}_e$ with crack length ratio $\bar{l}$. $\bar{G}_e$ is nonzero (positive) only when $\bar{l} > \bar{l}_{cr}$, where $\bar{l}_{cr}$ is the critical buckling length given by $\bar{l}_{cr} = \bar{h}/\sqrt{\bar{\varepsilon}_0}$. $\bar{G}_e$ increases rapidly with delamination length, reaching a maximum at $l/L = \bar{l}_{e*}$. Its minimum occurs at $l/L = \bar{l}_{e**}$. The difference between the minimum $\bar{G}_e(\bar{l}_{e**})$ and maximum $\bar{G}_e(\bar{l}_{e*})$ is more striking for this case than that for the "thin film" case. This is significant in that these values dictate the region of stable delamination growth as shown in the discussion of figures 5 and 6.

2.2.3 The Thick Beam and Symmetric Split Models

A great simplification in the general case treated in the previous section can be achieved by neglecting bending contributions of the sections' structure other than section 3, i.e., by assuming $\Theta \equiv 0$. This leads to model b (fig. 2b). The condition $\Theta=0$ implies $e_1 = e_2 = e_3 = a_1 = a_2 = \eta = 0$ in (25) (while η/Θ is finite). Substituting the reduced results obtained from (25) in (A-6) while taking the limit as $u_3 \to \pi$ gives:

$$\bar{U} = \frac{-\pi^4 \bar{h}\bar{l}}{18(1-\bar{h}+\bar{h}\bar{l})}(\bar{\varepsilon}_0 - \bar{\varepsilon}_{cr})^2 + \frac{\pi^4 \bar{\varepsilon}_0^{\,2}}{18(1-\nu^2)} \tag{26}$$

The strain energy release rate G_b is given by

$$G_b = -\frac{\partial U}{\partial l} \text{ or } \bar{G}_b = \frac{\pi^4 \bar{h}(1-\bar{h})}{18(1-\bar{h}+\bar{h}\bar{l})^2}(\bar{\varepsilon}_0 - \bar{\varepsilon}_{cr})[\,\bar{\varepsilon}_0 + \bar{\varepsilon}_{cr}\{3 + 4\bar{h}\bar{l}/(1-\bar{h})\}\,] \tag{27}$$

Generalization of this model with n (integer) delaminations results in model 2c, the analysis of which is identical to that of model 2b if "h" is replaced by "nh" (while leaving ε_{cr} unchanged)

$$\bar{G}_c = \frac{\pi^4 n\bar{h}(1-n\bar{h})}{18(1-n\bar{h}+n\bar{h}\bar{l})^2}(\bar{\varepsilon}_0 - \bar{\varepsilon}_{cr})[\,\bar{\varepsilon}_0 + \bar{\varepsilon}_{cr}\{3 + 4n\bar{h}\bar{l}/(1-n\bar{h})\}\,] \tag{28}$$

The symmetric split (model 2d) is a particular case of model 2c with n = 2, $\bar{h}$ = 0.5 ($n\bar{h} \to 1$),

$$\bar{G}_d = \frac{\pi^4}{18}[\,\bar{\varepsilon}_0\,\bar{l}^{-3} - \bar{l}^{-6}/4\,] \tag{29}$$

Finally, it is pointed out that the "thin film" model (model 2a) treated earlier is a further simplification of the general case over case b with $\bar{h} \equiv h/t \to 0$

$$\bar{G}_a = \lim_{\bar{h}\to 0}(\bar{G}_b/h)h$$

where G_a and G_b are given in (8) and (27), respectively.

Three of the models are compared in fig. 9. It can be seen there that the "thick beam" model is not a great improvement over the "thin film" model. The range of applicability of the "thin film" model can be established by comparing measures such as the maximum value of energy release rate. This is done in fig. 10 up to a delamination thickness ratio (h/t) of 0.10. Over this range the error between the two models is monotonic with h/t and load ratio ($\varepsilon_0/\varepsilon_L$). For larger values of h/t the comparison becomes more complicated due to the large shifts in the position of the maximum energy release rate.

2.3 TWO-DIMENSIONAL MODEL

The analysis for the two-dimensional delamination/buckling model is developed in this section based on the information gained from the one-dimensional model. A formulation of the elliptical plate problem is given in section 2.3.1 along with the numerical solution. The buckling load of the elliptical delamination, which represents the minimum load at which the delamination can spread, is presented in section 2.3.2. A fracture criterion accounting for growth along the two delamination axes is developed in section 2.3.3. This section includes also a presentation of numerical data from which the delamination growth behavior can be constructed based on the fracture criterion developed.

The growth behavior of an elliptical delamination is illustrated in section 2.3.4 for various geometries and loads. Both the case of a delamination introduced prior to inception of loading and the one in which the delamination is introduced into a preloaded structure are considered. The special case where the initial delamination is circular in shape is studied in detail in section 2.3.5. This case is of special significance in the present work since it approximates the damage introduced by impact. In this section a quantitative comparison between the proposed model and impact experiments is made, and the parameters affecting damage growth tolerance are identified.

2.3.1 The Elliptical Plate Problem

The stages in the two-dimensional thin film delamination and buckling are shown in fig. 11. The elliptical delamination of thickness h, major axis "a" and minor axis "b" is part of an infinite half-space. Stage i represents the unstressed medium while stage ii denotes the uniform axially compressed medium. Stage iii differs from ii in that the delamination has buckled. It is assumed that during this transition the state of strain in the backing medium remains unaltered. The

problem formulated in this manner requires the post-buckling solution of a thin elliptical plate clamped along its boundary and subjected to the following displacement constraints:

$$u = \nu\varepsilon_0 x \ , \ v = -\varepsilon_0 y \ , \ w = \frac{\partial w}{\partial x} = \frac{\partial w}{\partial y} = 0 \qquad (30a)$$

on the boundary $$(\frac{x}{a})^2 + (\frac{y}{b})^2 = 1 \qquad (30b)$$

where u, v and w are the displacement components along the x, y and z directions, respectively.

Only two treatments of an elliptical plate subjected to axial loading at the edge are known to exist. Both Woinowsky-Krieger [11] and Shibaoka [12] have considered the buckling load of an elliptical plate uniformly compressed along its edge. The first reference employed the Rayleigh-Ritz method while the second obtained a formal solution which cannot be expressed in a closed-form. The problem at hand, which is more complicated in nature and also requires a solution into the post-buckling regime, is solved in an approximate manner. The energy method has been widely used in the past to obtain large-deflection approximate solutions, such as in [13] for the case of an elliptical plate subjected to a uniform normal pressure, and will be adopted in the present work.

In the energy method the displacement solution is approximated by an admissible displacement field given in terms of unknown coefficients. These coefficients are determined from the requirement that the potential energy be stationary. The strain energy in the delamination section is given by

$$U = 2\int_{-h/2}^{h/2} \int_{0}^{a} \int_{0}^{b\sqrt{1-(x/a)^2}} \sigma_{\alpha\beta}\, \varepsilon_{\alpha\beta} \, dz \, dx \, dy \quad , \quad \alpha,\beta = 1,2 \qquad (31)$$

The integrand in (31) can be expressed in terms of displacement gradients by using the large-deflection displacement-strain relation and the stress-strain

relation:

$$\varepsilon_{\alpha\beta} = (u_{\alpha,\beta} + u_{\beta,\alpha})/2 + (w_{,\alpha}\, w_{,\beta})/2 - z w_{,\alpha\beta} \quad , \quad \alpha,\beta = 1,2 \tag{32}$$

$$\sigma_x = \frac{E(\varepsilon_x + \nu\varepsilon_y)}{(1-\nu^2)} \; , \; \sigma_y = \frac{E(\varepsilon_y + \nu\varepsilon_x)}{(1-\nu^2)} \quad , \; \sigma_{xy} = \frac{E\varepsilon_{xy}}{(1+\nu)} \tag{33}$$

where $u_1 \equiv u$, $u_2 \equiv v$ and the symbol " , " represents differentiation. The problem can be greatly simplified by adopting the following nondimensionalizations:

$$\bar{x} = \frac{x}{b} \; , \; \bar{y} = \frac{y}{b} \; , \; \bar{u} = \frac{ub}{h^2} \; , \; \bar{v} = \frac{vb}{h^2} \; , \; \bar{w} = \frac{w}{h} \tag{34}$$

The boundary conditions (30) take the form

$$\bar{u} = \frac{\nu\lambda\bar{x}}{(1-\nu^2)} \quad , \quad \bar{v} = \frac{-\lambda\bar{y}}{(1-\nu^2)} \quad , \quad \bar{w} = \frac{\partial\bar{w}}{\partial\bar{x}} = \frac{\partial\bar{w}}{\partial\bar{y}} = 0 \tag{35a}$$

on the boundary $$\frac{\bar{x}^2}{\xi^2} + \bar{y}^2 = 1 \tag{35b}$$

where $$\xi \equiv a/b = \text{delamination aspect ratio} \tag{36a}$$

and $$\lambda \equiv (1-\nu^2)\varepsilon_0(b/h)^2 = \text{load-geometry parameter} \tag{36b}$$

The strain energy can then be expressed in terms of the two nondimensional parameters in (36)

$$\bar{\bar{U}}(\xi,\lambda) \equiv \frac{U}{\pi abEh^5[2(1-\nu^2)^2 b^4]^{-1}} =$$

$$\frac{4(1-\nu^2)}{\pi\xi}\int_0^{\xi}\int_0^{\sqrt{1-\bar{x}^2/\xi^2}} \Bigg\{ \left[\left(\frac{\partial\bar{u}}{\partial\bar{x}}\right)^2 + \left(\frac{\partial\bar{v}}{\partial\bar{y}}\right)^2 + \frac{\partial\bar{u}}{\partial\bar{x}}\left(\frac{\partial\bar{w}}{\partial\bar{x}}\right)^2 + \frac{\partial\bar{v}}{\partial\bar{y}}\left(\frac{\partial\bar{w}}{\partial\bar{y}}\right)^2 \right] +$$

$$\frac{1}{4}\left[\left(\frac{\partial\bar{w}}{\partial\bar{x}}\right)^2 + \left(\frac{\partial\bar{w}}{\partial\bar{y}}\right)^2 \right]^2 + \frac{1}{12}\left[\frac{\partial^2\bar{w}}{\partial\bar{x}^2} + \frac{\partial^2\bar{w}}{\partial\bar{y}^2} \right]^2 +$$

$$\nu\left[2\frac{\partial\bar{u}}{\partial\bar{x}}\frac{\partial\bar{v}}{\partial\bar{y}} + \frac{\partial\bar{u}}{\partial\bar{x}}\left(\frac{\partial\bar{w}}{\partial\bar{y}}\right)^2 + \frac{\partial\bar{v}}{\partial\bar{y}}\left(\frac{\partial\bar{w}}{\partial\bar{x}}\right)^2 \right] +$$

$$\frac{(1-\nu)}{2}\left[\left(\frac{\partial\bar{u}}{\partial\bar{y}} + \frac{\partial\bar{v}}{\partial\bar{x}}\right)\left(\frac{\partial\bar{u}}{\partial\bar{y}} + \frac{\partial\bar{v}}{\partial\bar{x}} + 2\frac{\partial\bar{w}}{\partial\bar{x}}\frac{\partial\bar{w}}{\partial\bar{y}}\right) \right] \Bigg\} d\bar{x}\, d\bar{y} \tag{37}$$

The boundary conditions (35) and the symmetry requirements will be satisfied by the following infinite series for the displacements:

$$\bar{u} = \frac{bu}{h^2} = \frac{\nu\lambda\bar{x}}{(1-\nu^2)}\Big[\, 1 + (\bar{x}^2/\xi^2 + \bar{y}^2 - 1)(c_1 + d_1\bar{x}^2 + e_1\bar{y}^2 + f_1\bar{x}^2\bar{y}^2 + \cdots)\Big]$$

$$\bar{v} = \frac{bv}{h^2} = \frac{\lambda\bar{y}}{(1-\nu^2)}\Big[-1 + (\bar{x}^2/\xi^2 + \bar{y}^2 - 1)(c_2 + d_2\bar{x}^2 + e_2\bar{y}^2 + f_2\bar{x}^2\bar{y}^2 + \cdots)\Big] \quad (38)$$

$$\bar{w} = \frac{w}{h} = (\bar{x}^2/\xi^2 + \bar{y}^2 - 1)^2\,(c_3 + c_4\bar{x}^2 + c_5\bar{y}^2 + c_6\bar{x}^2\bar{y}^2 + \cdots)$$

Naturally, it is impossible to determine the triple infinity of the coefficients involved in the solution of (38) and only the coefficients c_i, i = 1-5, will be assumed nonzero here. The accuracy of the solution resulting from this rather limited choice may be questioned. However, due to the fact that the solution method is based on minimization of the strain energy, which is the ultimate desired unknown here, it is believed that this choice is capable of bringing out the characteristic behavior of the proposed model. A more accurate solution is left for future work.

Upon substitution of (38) in the expression for the strain energy (equation 37) and carrying out the integration over the prescribed limits, the strain energy in the plate is obtained in terms of the five coefficients c_i , i = 1-5. Next, these coefficients are determined from the condition that the incremental energy due to a variation in any of them is zero, i.e.

$$\frac{\partial\bar{\bar{U}}}{\partial c_i} = 0 \quad , \quad i = 1-5 \qquad (39)$$

Equation (39) defines five nonlinear equations with five unknowns provided λ, ξ and ν are predetermind. The solution of (39) is carried out numerically using the Newton method. In all subsequent calculations the Poisson's ratio ν was taken to be 0.3.

2.3.2 The Buckling Load

Since the delamination can grow only after it has buckled, it is of interest to determine the buckling load as a function of the plate geometry. In the early stages of buckling the lateral displacement w is small and the inplane displacements u and v retain their prebuckling values. This results in three linear equations with the three unknowns c_3, c_4 and c_5. The requirement of a non-trivial solution leads to an eigenvalue problem. This equation is solved in a closed-form, and the results are given in fig. 12 for three approximations. The normalized load for the three-term approximation approaches 0.876 as $a/b \to \infty$, compared with $\pi^2/12$ (= 0.822) for the exact solution (one-dimensional) and 1.0 for the approximate solution given in [11].

2.3.3 Fracture Criterion and Numerical Data Interpretation

The fracture criterion in the present two-dimensional problem is derived in a manner similar to the one-dimensional case along with the assumption that the elliptical character of the delamination is maintained during the delamination growth.

Consider the strain energy released from the system (half-space & delamination) as the elliptical delamination axes are allowed to extend by small amounts "Δa" and "Δb" as shown in sketch 2.

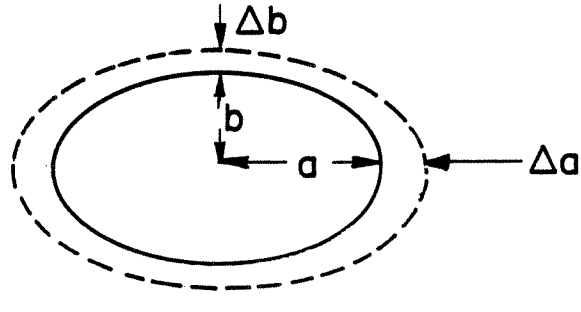

SKETCH 2

The state of strain in the half-space is assumed to be unaltered during this transition. The energy available for crack growth must come from the change in the strain energy stored in the elliptical delamination plus the energy released by the new delaminated area. A balance of energy then gives (in the limit as $\Delta a \to 0$, $\Delta b \to 0$)

$$G = -\frac{dU}{dA} + \frac{Eh\varepsilon_0^2}{2} \tag{40}$$

where G is the strain energy release rate per unit area, $A = \pi ab$, and

$$dU = \frac{\partial U}{\partial a}da + \frac{\partial U}{\partial b}db \tag{41a}$$

$$dA = \pi(adb + bda) \tag{41b}$$

Use of (41) in (40) leads to the following expression for G

$$G = \frac{G^a + G^b \frac{a}{b}\frac{db}{da}}{1 + \frac{a}{b}\frac{db}{da}} \tag{42}$$

where G^a and G^b are the "crack driving forces" along the "a" axis ("b" fixed) and along the "b" axis ("a" fixed), respectively, and are given as follows;

$$G^a = \frac{-1}{\pi b}\frac{\partial U}{\partial a} + \frac{Eh\varepsilon_0^2}{2} \tag{43a}$$

$$G^b = \frac{-1}{\pi a}\frac{\partial U}{\partial b} + \frac{Eh\varepsilon_0^2}{2} \tag{43b}$$

For given problem parameters (i.e. load and geometry) both G^a and G^b can be determined from (43) by means of simple numerical differentiations of the strain energy in (37). In order to determine the strain energy release rate G from (42), however, the slope db/da, which determines the new shape of the delamination, has to be provided. This quantity is not arbitrary, but is selected such as to provide the *maximum energy release possible with a unit increase of*

the delamination area. Sketch 3 shows the dependence of G, given in (42), on the slope db/da from which the selection of the latter is made.

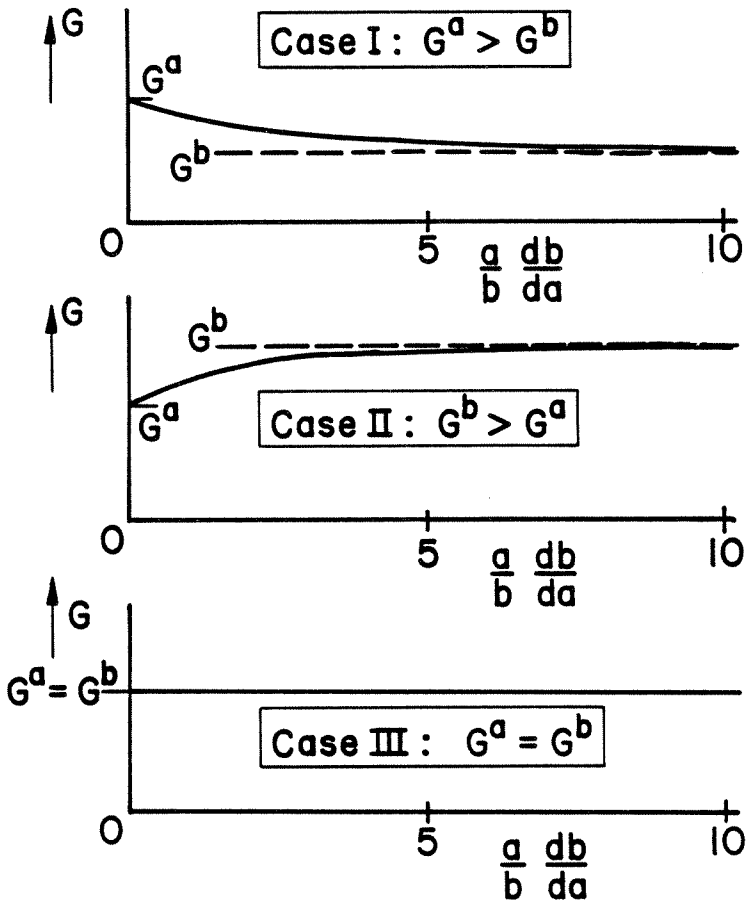

SKETCH 3 The Dependence of G on db/da

Depending upon the relative magnitude of G^a and G^b, there are three distinct cases which affect this selection, i.e.;

Case I; $G^a > G^b$: Then from sketch 3, G is maximum when db/da=0. This leads to $G=G^a$.

Case II; $G^b > G^a$: Then from sketch 3, G is maximum when da/db=0. This leads to $G=G^b$.

Case III; $G^a=G^b$: For this case, sketch 3 shows that there is no local maximum

for G, and $G=G^a=G^b$. The slope db/da cannot be determined from sketch 3, which represents the pre-fracture conditions, but it can be determined from the post-fracture conditions as will be seen later on.

From this discussion it appears that a knowledge of the quantities G^a and G^b is sufficient to determine the delamination growth history. These quantities are presented in fig. 13 as a function of the problem parameters. For a convenience, the following normalizations were employed:

$$\xi \equiv a/b = a^*/b^* \ , \ \lambda \equiv (1-\nu^2)\varepsilon_0(b/h)^2 = \varepsilon^*_0 b^{*2} \tag{44}$$

$$\varepsilon^*_0 = \frac{\varepsilon_0}{(1-\nu^2)^{-1}\,\Gamma^*_0{}^{1/2}}$$

$$a^*, b^* = \frac{(a,b)}{h\,\Gamma^*_0{}^{-1/4}} \tag{45}$$

$$\Gamma^*_0 = \frac{\Gamma_0}{Eh[2(1-\nu^2)]^{-1}}$$

All subsequent delamination growth histories were constructed from fig. 13. A brief review of data interpretation procedure follows.

Consider a fixed load-geometry parameter, $\varepsilon^*_0 b^{*2}$, and examine the dependence of the strain energy release rate G on a/b from fig. 13a. Starting from buckling, the G^a 's traces exhibit a sharp rise followed by a monotonic decrease while the G^b 's are monotonically increasing with increasing a/b. The two families of curves meet along the curve marked $G^a=G^b$. In the region to the left of this curve $G^a > G^b$ while the opposite is true for the region to the right. For aspect ratios that fall to the left of this curve, "case I" shows that only the "a" axis can grow, the "b" axis is fixed, and $G=G^a$. Delamination growth in this region is characterized by one parameter ("a"), and the growth history can be constructed according to the discussion of fig. 5 in chapter 1, in connection with the one-dimensional model.

Now suppose that the "a" axis has been increased (either by increasing the load or by an unstable growth under constant load) so that a/b approaches the path $G^a=G^b$ from the left. Then $G^a = G^b$ ($\geq \Gamma_0$), and further growth can take place. The new shape of the delamination, dictated by the ratio db/da, is determined from the maximum energy release condition in accordance with "case III". It can be shown that this condition is satisfied for growth geometries constrained by the path $G^a=G^b$. Furthermore, this mode of growth is always unstable (i.e. the growth is under constant load). Figure 14 presents the curve $G^a=G^b$ in two different coordinate systems. It is seen from this figure that the energy release rate monotonically increases over its value at the inception of this curve as the delamination axes grow. Therefore, any delamination on this curve with $G \geq \Gamma_0$ is unstable. It is also seen from fig. 14 that during this unstable growth the "a" axis extends more rapidly than the "b" axis, i.e at a ratio of about 5 to 1.

When the initial aspect ratio is such that it is to the right of the curve $G^a=G^b$, "case II" shows that the growth is along the "b" axis, "a" is fixed, and $G=G^b$. It is more convenient to analyze this situation with the data represented as in fig. 13b. The analysis for this case becomes similar to the former if the roles of "a" and "b" are interchanged.

2.3.4 The Growth Pattern of a Delamination

The model developed in this chapter will now be used to display the damage growth behavior that would be expected when a laminated panel is damaged by impact. Depending upon the time in the load history at which the delamination is introduced, two different cases are considered. **Case a** will be the case where the delamination is introduced into a preloaded structure while in **case b**, the delamination is introduced prior to inception of loading. In either case the

analysis will follow the growth history of the delamination. The special situation where the delamination is initially circular is discussed in this section briefly; a more comprehensive treatment is given in section 2.3.5.

The geometry of the problem and the delamination growth pattern for "case a" are illustrated in fig.15 for two different loadings[1]. Depending upon the load and the initial delamination size and shape, various growth patterns can take place. The delamination can remain stable, grow unstably and then be arrested at a later stage, or grow unstably without arrest. Furthermore, unstable growth can occur along either one of the delamination axes or along both axes simultaneously. Suppose, for instance, that the delamination at point 1 in fig. 15a is suddenly introduced into the preloaded structure ($\varepsilon^*_0 = 1.40$). Then unstable growth of "a" takes place until "a" is about twice its initial value (point 2). The "b" axis remains fixed during this growth. Thereafter, both axes grow unstably and simultaneously along the dashed curve, while the strain energy release rate steadily increases. Fig. 15a shows that a propagating delamination can be arrested at a later stage, as was found in the one-dimensional model. This is illustrated by points 3 and 4. The delamination at point 3 will propagate unstably along the "a" axis and will be arrested at point 4. Note, however, that the range of delamination size and shape at which this may occur is rather limited.

Delamination growth in which the "b" axis extends first can also take place. Again, delamination can grow unstably along one axis (point 6 to point 7) and then continue to grow along the dashed curve where both "a" and "b" grow simultaneously. Delamination can also be arrested at a later stage (point 7 to point 8). These modes of growth in which the "b" axis extends first are limited, however, to relatively large aspect ratios.

---

1 In the construction of fig. 15, the effect of the excess energy released in the transition from the unbuckled state to the buckled state was neglected.

According to fig. 15a, a circular delamination of any size remains stable. This is not true, however, when higher preload condition, such as in fig. 15b (ε^*_0 = 1.93), is considered. For instance, the initial circular delamination at point 9 will propagate horizontally (transverse to the loading direction) to about twice its size "a" and then continue to grow unstably along the dashed curve. Fig. 15b also shows, in contrast to fig. 15a, that no arresting mechanism exists, and any delamination that has started to grow will continue to grow.

The case where the delamination is introduced prior to loading ("case b") is considered next. Upon loading the structure, the delaminated area buckles. Increased loading will produce further delamination. The growth pattern will depend upon the aspect ratio and the initial delamination size. The growth can be stable with load (along either one of the delamination axes) or unstable, the latter which takes the same form as in "case a". The geometry of the problem and the growth behavior are illustrated in fig. 16. This figure was constructed for a given initial axis "b" (i.e. b^*_0 = 2.39). Starting with a circle, no growth is possible until the load is sufficiently large (point 1). At point 1 the growth is unstable, with "a" increasing until it is about 3 times as large as "b" (point 2). Thereafter, both "a" and "b" grow unstably and simultaneously with the aspect ratio increasing. For a 2 to 1 ellipse, the growth is initially stable with only "a" increasing as the load increases (point 4 to point 5). For aspect ratios slightly above 1, unstable growth followed by delamination arrest can take place (point 3 to point 4). For aspect ratios above point 5, the growth is first in "b". This initial growth can be stable or unstable. For instance, for aspect ratio corresponding to point 6, the growth is stable with load (point 6 to point 7). At point 7 both "a" and "b" grow unstably along the dashed curve. Yet for larger values of a/b, it was found that the delamination will first extend unstably along the "b" axis. Then both "a" and "b" grow unstably and simultaneously. These relatively large

aspect ratios are uninteresting in the present application and, therefore, have been eliminated from fig. 16.

2.3.5 The Growth History of a Circular Delamination

The situation where the delamination introduced is circular in shape has a special significance in the present work since it approximates the damage introduced by impact. The following analysis will study the growth conditions for a circular delamination as well as the growth behavior itself.

The growth history is illustrated in fig. 17 for both "case a" and "case b". First consider "case b". Upon increasing the load from zero, the (circular) delamination will buckle. Further increased loading produces unstable growth. The load at which this occurs depends on the size or radius of the delamination. This dependence is plotted in fig. 17 as a heavy-solid line, and is identified there as a "propagation threshold curve". On this curve the vertical axis measures the load ε^*_0 (since $b^*/r^* = 1$ there) and the horizontal axis measures the delamination radius r (since $a^* = b^* = r^*$ there). A noted feature of this curve is that the load to failure becomes larger as the delamination size becomes smaller.

Impact damage tolerance of a composite laminate is perhaps best characterized by the strength failure threshold curve; i.e a curve in the load-impact velocity domain as shown in fig.7 chapter 1. Therefore, it is of practical importance to relate the theoretical failure (or propagation) threshold curve in fig. 17 to the experimental one(s) so that the parameters controlling damage arrest can be understood. This can be done if a suitable relation between the impact velocity axis (in the experimental curve) and the delamination size axis (in the theoretical curve) can be found. Measurements of damage area resulting from impact have been carried out in [7] for various graphite/epoxy laminates. These measurements indicate that the variables of concern are approximately linearly

dependent over a broad range of impact velocity (0-250 ft/sec). Accordingly, the threshold curve in fig. 17 is replotted in fig. 18 (the solid curve) with the *circular delamination area* as the horizontal axis. While a quantitative comparison between the theoretical threshold curve (fig. 18) and the experimental one(s) (fig. 7 chapter 1) is difficult to make due to the complex nature of the impact process, it is quite clear that both curves display a rather similar load versus damaged area character. In both curves the load to failure is unaffected by a small damaged area and its rate of change at a relatively large damaged area is small. Also, in-between these two extremes there exists a transition region where the load-to-failure is changing rapidly. These similarities suggest that the model can be used as a guide toward impact damage tolerance improvements. From fig. 18 it is evident that improving damage tolerance (i.e. shifting the curve upward) can be achieved by increasing Γ_0, the fracture energy. This prediction was examined by measuring Γ_0 for two graphite/epoxy systems[2], constructed from the same graphite fibers but with different resins, and examining the test results with impact damage tolerance performance available for these materials [8,9]. It was found that the material with the better damage tolerance has the larger fracture energy.

It is now noted that the theoretical threshold curve was obtained by loading delaminated structures to failure ("case b") whereas the experimental one was generated by impacting preloaded panels ("case a"). These two curves differ from each other. According to the discussion of fig. 4 in chapter 1, there would be an excess of energy released during the transition from the unbuckled state to the buckled state. This energy may contribute to further delamination growth. This, in turn, will lower the load at which failure occurs. The effect of this consideration is evaluated next.

2 The details of these measurements are given in the appendix at the end of the thesis.

The additional fracture surface generated by the transition from the unbuckled state to the buckled state can be found from the following energy balance consideration:

$$\alpha \Delta U = \Gamma_0(\pi r^2 - \pi r_0^2) \tag{46}$$

or

$$r^*_0 = r^* \sqrt{1 - \frac{\alpha \Delta \bar{\bar{U}}}{(1-\nu^2) r^{*4}}} \tag{47}$$

where it was assumed that the newly generated area is a circular annulus, and

ΔU = the energy released in the transition from the unbuckled state to the buckled state.

$\alpha \Delta U$ = the fraction of energy available for further fracture, $0 \leq \alpha \leq 1$.

r_0 = the initial delamination radius introduced in the unbuckled state.

r = the new delamination radius (in the buckled state).

$\Delta \bar{\bar{U}}$ = the normalized excess energy.

If the load ε^*_0 and the new delamination radius r^* are a pair on the threshold curve of "case b", then ε^*_0 and r^*_0 would be a pair on a threshold curve corresponding to "case a" and can be found from (47) and fig. 19. The result is shown in fig. 18 as a dashed curve. This curve was constructed for a specific value of α, i.e. $\alpha = 1$. It is seen that the effect of the present consideration is to lower the load to failure over "case b" by about 6%. This finding is in line with experiments reported in [7] and reproduced in fig. 7 chapter 1, though the difference in [7] is more pronounced (about 13%).

Having studied the conditions necessary for a circular delamination to become unstable, the growth following the onset of instability will now be considered from fig. 17. Unlike the variety of growth behavior observed in the

previous section following the introduction of an elliptical delamination, the growth pattern of an initially circular delamination is more restricted. It was found that the growth is predominantly normal to the loading direction regardless of the delamination size and load. Furthermore, the growth is always unstable and there is no arresting mechanism at a later stage.

The growth behavior is exemplified in fig. 17 through points 1, 2 and 3. The conditions at point 1 represent the onset of instability for "case b", but, in order to simplify the discussion, it is assumed here that this is also true for "case a". The delamination at point 1 increases its "a" axis by about a factor of 2 (point 2) before both "a" and "b" grow simultaneously. During the latter growth, the "a" axis extending more rapidly than the "b" axis. At point 3 the "a" axis has already extended by more than 300% while the "b" axis by only 40% (at point 3 a/b= 6/2.25). Also, during the latter growth the strain energy release rate, G, increasing monotonically as the delamination spreads (see fig. 14). This indicates that *the tendency for delamination growth increases with increasing damage size.* Points 4, 5 and 6 exemplify the growth for a larger load on the threshold curve. The initial extension along the "a" axis (point 4 to point 5) is smaller than in the previous example, though the aspect ratio at point 6 (a/b= 6/1.95) is larger than that at point 3. This type of growth was observed in impact experiments reported in chapter 1 where numerous test data around the experimental threshold curve are available for comparison. The high-speed photographs show that the growth is always unstable, and it is predominantly normal to the load. This type of growth is also realized when loading to failure either a damaged panel or a simulated delamination [8,9].

The growth behavior of a circular delamination loaded above the threshold load can also be followed from fig. 17. Consider, for instance, the delamination at point 1'. This delamination has the same size as that at point 1, but it is

subjected to about 60% higher load. The growth, illustrated by points 1', 2' and 3', is similar to that illustrated by points 1, 2 and 3. It is interesting to note, however, that the minor axis at point 3' is smaller than that at point 3 (1.98 compared with 2.25). This indicates that when impacting two differently loaded panels at the same speed, the panel subjected to the smaller load will yield the larger damage extension in the load axis during the delamination growth. This growth behavior, while it appears surprising, has indeed been observed in impact experiments (see fig 12 in chapter 1).

It is of interest to follow the deflection distribution in the delamination section in a manner which will allow for a visual comparison with experiments. This was done in fig. 20a, where the deflection is presented as contours of equal out-of-plane displacements similar to the moire fringes photographed during impact tests. The sequence in fig. 20a describes an unstable growth of a delamination, with the upper print representing the onset of growth at point 1 in fig. 17. The other prints in fig. 20a are "scans" during the unstable growth from point 1 to point 2 in fig. 17. Fig. 20b shows a sequence of damage growth observed in the impact experiment. This test was carried out in a near-threshold condition, with the relative location of the test data (i.e. load and impact velocity) on the experimental threshold curve being similar to the relative location of point 1 in fig. 17 on the theoretical threshold curve. *These similarities in threshold location provide the basis for a comparison.* Note that in order to allow for a convenient comparison between fig. 20a and fig. 20b, the parameters were scaled as follows:

a) The normalized fringe constant in fig. 20a , i.e. w/nh, was selected such as to provide an equal number of fringes for the two upper prints in fig. 20.

b) The normalized delamination diameter in the upper print in fig. 20a was

scaled in size to the measured damage diameter in the upper print in fig. 20b.

Clearly, both the experimental and the theoretical sequences in fig. 20 display similar spatial deflection distribution during the delamination growth. Also, the relative increase in the peak displacement with increasing delamination size is similar in both figures. The magnitude of the peak displacement in the first print in both figures will be equal if the fringe constant in both figures is made equal. This specifies the delamination thickness h to be 0.041 in. (1.03mm). A more strict comparison can be made if Γ^*_0 is specified too. For the purpose of estimating orders of magnitude, let $\Gamma^*_0 = 670 \times 10^{-6}$. (Such value arises, for instance, by the following combination: $E = 10^7$ p.s.i., h = 0.041 in., $\nu = 0.3$ and Γ_0 = 1.5 lb/in.). With the aid of (45), one then obtains the following values for the load and delamination radius:

$$\varepsilon_0 = 0.00481 \quad \text{and} \quad r = 1.38 \text{ in.}$$

The experimental values are:

$$\varepsilon_0 = 0.00326 \quad \text{and} \quad r \approx 0.75 \text{ in.}$$

While a one-to-one agreement is not expected here due to the complex nature of the impact process, these theoretical values appear quite encouraging.

CONCLUSIONS

The models of delamination buckling and growth developed in this chapter display an interesting variety of behavior depending upon the dimensions of the delamination, the load at which it is introduced and the fracture energy. When loading an initially delaminated structure, the growth of the delamination may be stable, unstable or an unstable growth followed by an arrest. The range of this behavior can be found from the results presented and could form the basis for an experimental study of the applicability of the proposed model.

While the analysis is developed under a broad range of delamination conditions, emphasis is placed on the conditions that simulate impact-induced damage. It was found that the growth history of impact-simulated delamination predicted by the model is similar to that observed in impact experiments. In particular, it was found that the growth of the damaged area is always unstable, and it occurs predominantly normal to the loading direction.

A theoretical failure threshold curve was developed which is analogous to the experimental one. The theoretical model, which determines the conditions for a circular delamination to become unstable, displays characteristics similar to the experimental threshold curve. Therefore, the model can be used as a guide for impact damage tolerance improvements. The model identifies the parameters controlling damage arrest. It was found that the predominant factor controlling this is the fracture energy Γ_0.

REFERENCES

1. R. Guernsey, J. Gilman, "Photoelastic Study of the Stresses near a Cleavage Crack", Exptl. Mech., Vol. 1, p 50, (1961).

2. N.L. Svensson, "The Variation of the Fracture Energy of Brittle Plastics with Temperature", Proc. Phys. Soc., Vol. 77, p 876, (1961).

3. L.M. Kachanov, "The Separation of Fiberglass Tubes Subjected to an External Pressure", Mekh. Polim., No. 6, p 1106, (1975).

4. L.M. Kachanov, "Separation of Composite Materials", Mekh. Polim., No.5, p 918, (1976).

5. C.L. Chow, K.M. Ngan, "Method of Fracture Toughness Evaluation of Adhesive Joints", J. of Strain Analysis, Vol. 15, No.2, p 97, (1980).

6. J.D. Whitcomb, "Finite Element Analysis of Instability-Related Delamination Growth", NASA TM 81964, (March 1981).

7. M.D. Rhodes, J.G. Williams and J.H. Starnes, Jr., "Low-Velocity Impact Damage in Graphite-Fiber Reinforced Epoxy Laminates", presented at the 34th Annual Conference Reinforced Plastics/Composite Institute, New Orleans, Louisana, (Jan. 29 - Feb. 2, 1979).

8. J.G. Williams, M.S. Anderson, M.D. Rhodes, J.H. Starnes, Jr. and W.J. Stroud, "Recent Developments in the Design, Testing and Impact-Damage Tolerance of Stiffened Composite Panels", NASA TM 80077, (April 1979).

9. B.A. Byers, "Behavior of Damaged Graphite/Epoxy Laminates Under Compression Loading", NASA CR 159293, (August 1980).

10. D.Y. Konishi, W.R. Johnston, "Fatigue Effects on Delaminations and Strength Degradation in Graphite/Epoxy Laminates", Composite Materials: Testing and Design (Fifth Conference), ASTM STP 674, S.W. Tsai, Ed., pp 597-618, (1979).

11. S. Woinowsky-Krieger, "The Stability of a Clamped Elliptic Plate Under Uniform Compression", J. Appl. Mech., Vol. 4, p A-177, (1937).

12. Y. Shibaoka, "On the Buckling of an Elliptic Plate with Clamped Edge, part II", J. of the Physical Society of Japan, Vol. 12, No. 5, p 529, (1957).

13. N.A. Weil and N.M. Newmark, "Large Deflections of Elliptical Plates", J. of Appl. Mech., Vol. 23, p 21, (1956).

APPENDIX

The f_i and g_i in equation 15 are as follows;

$$f_1(x) = \frac{l_1}{4u_1(1-u_1/\tan u_1)}\left[\frac{(\sin 2u_1-2u_1)}{\sin^2 u_1}\sin^2 u_1x_1/l_1 - \sin 2u_1x_1/l_1 + 2u_1x_1/l_1\right]$$

$$g_1(x) = \frac{1}{2(1-u_1/\tan u_1)}\left[\frac{(\sin 2u_1x_1/l_1 - 2u_1x_1/l_1)}{\tan u_1} + 2\sin^2 u_1x_1/l_1\right]$$

$$f_i(x) = \frac{l_i}{2u_i \sin u_i}(\cos 2u_ix_i/l_i - \cos u_i) \quad , \quad g_i(x) = 1 \quad , \quad i = 2,3$$

where

$$u_i = \frac{l_i}{2}\sqrt{P_i/D_i} \quad , \quad i = 1-3$$

The nondimensional equations for the strains ε_i and the end rotation Θ are given by the following equations (A-1) – (A-4)

$$\bar{\varepsilon}_1 - (1-\bar{h})\bar{\varepsilon}_2 - \bar{h}\bar{\varepsilon}_3 = 0 \tag{A-1}$$

$$\left\{\frac{3\bar{h}\bar{\Theta}}{\pi^2} + \frac{3\bar{\Theta}^2}{8\pi^2}\left[\frac{(1-\bar{l})(4u_1 - \sin 4u_1)}{2u_1 \sin^2 2u_1} + \frac{\bar{l}(2u_2 - \sin 2u_2)}{u_2 \sin^2 u_2}\right]\right\} +$$

$$\frac{1}{(1-\nu^2)}[\,\bar{\varepsilon}_1 - \bar{\varepsilon}_0 + \bar{l}(\bar{\varepsilon}_2-\bar{\varepsilon}_1)\,]=0 \tag{A-2}$$

$$\left\{\frac{3\bar{\Theta}}{\pi^2\bar{l}} + \frac{3\bar{\Theta}^2}{8\pi^2}\frac{(2u_2 - \sin 2u_2)}{u_2 \sin^2 u_2}\right\} -$$

$$\frac{3\bar{\Theta}^2}{8\pi^2}\frac{(2u_3 - \sin 2u_3)}{u_3 \sin^2 u_3} + \frac{(\bar{\varepsilon}_2 - \bar{\varepsilon}_3)}{(1-\nu^2)} = 0 \tag{A-3}$$

$$\bar{\Theta}\bar{l}\left[\frac{\bar{l}}{(1-\bar{l})}\frac{2u_1}{\tan 2u_1} + (1-\bar{h})^3\frac{u_2}{\tan u_2} + \bar{h}^3\frac{u_3}{\tan u_3}\right] +$$

$$(1-\bar{h})\left\{\left[\frac{2u_1\bar{l}}{(1-\bar{l})}\right]^2 - \left[(1-\bar{h})u_2\right]^2\right\}=0 \tag{A-4}$$

$$u_1 = \frac{\pi(1-\bar{l})}{2}\sqrt{\frac{(\bar{\varepsilon}_1 - \nu^2\bar{\varepsilon}_0)}{(1-\nu^2)}}$$

$$u_2 = \frac{\pi\bar{l}}{(1-\bar{h})}\sqrt{\frac{(\bar{\varepsilon}_2 - \nu^2\bar{\varepsilon}_0)}{(1-\nu^2)}} \qquad \text{(A-5)}$$

$$u_3 = \frac{\pi\bar{l}}{\bar{h}}\sqrt{\frac{(\bar{\varepsilon}_3 - \nu^2\bar{\varepsilon}_0)}{(1-\nu^2)}}$$

The nondimensional strain energy is as follows;

$$\bar{U} \equiv \frac{U}{ET^5\,L^{-3}\,(1-\nu^2)^{-1}} =$$

$$\frac{\pi^4}{18(1-\nu^2)^2}\left[(1-\bar{l})\bar{\varepsilon}_1^{\,2} + (1-\bar{h})\bar{l}\,\bar{\varepsilon}_2^{\,2} + \bar{h}\bar{l}\,\bar{\varepsilon}_3^{\,2} + \nu^2\bar{\varepsilon}_0\,(\bar{\varepsilon}_0 - 2\bar{\varepsilon}_1)\right] +$$

$$\frac{\bar{\Theta}^2}{24}\left[\frac{2}{(1-\bar{l})}\frac{u_1(4u_1 + \sin 4u_1)}{\sin^2 2u_1} +\right.$$

$$\left.\frac{(1-\bar{h})^3}{\bar{l}}\frac{u_2(2u_2 + \sin 2u_2)}{\sin^2 u_2} + \frac{\bar{h}^3}{\bar{l}}\frac{u_3(2u_3 + \sin 2u_3)}{\sin^2 u_3}\right] \qquad \text{(A-6)}$$

The e_i, i = 1-3; a_1 and a_2 in equation (25) are as follows;

$$e_1 = -\frac{[\,(1-\nu^2)(1-\bar{h})\alpha_1 - \bar{h}\bar{l}\,e_3\,]}{(1-\bar{h}+\bar{h}\bar{l})}$$

$$e_2 = -\frac{[\,(1-\nu^2)\alpha_1 + \bar{h}(1-\bar{l})e_3\,]}{(1-\bar{h}+\bar{h}\bar{l})}$$

$$e_3 = 2(1-\nu^2)\,\bar{\varepsilon}_{cr}\,(\,\eta/\pi + \eta^2/2\pi^2\,)$$

$$a_1 = \alpha_2\kappa - \alpha_1 - e_3/(1-\nu^2) - \frac{3\kappa}{4\pi^2}\frac{\bar{\Theta}^2}{\sin^2\eta}\left\{1 - \left[\frac{\sin\eta}{\eta}\right]^2 - \frac{\sin 2\eta}{2(\pi+\eta)}\right\}$$

$$a_2 = \frac{(\eta + \eta^2/\pi)}{\tan\eta} - 1$$

Where α_1 and α_2 are given by the curley bracket in equations (A-2) and (A-3), respectively, and $\kappa = 1-\bar{h}+\bar{h}\bar{l}$.

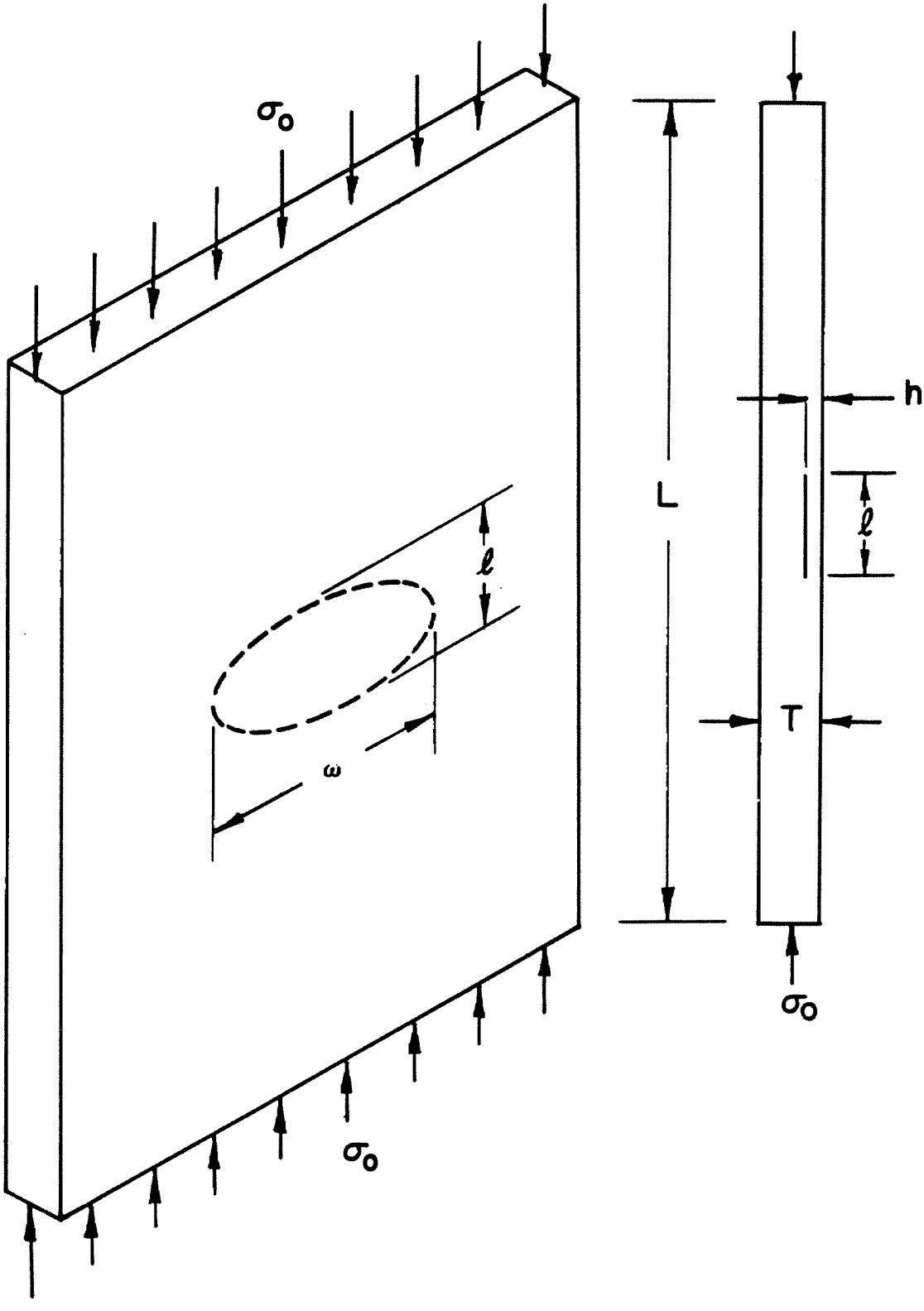

FIG. 1 IDEALIZED DELAMINATED PLATE

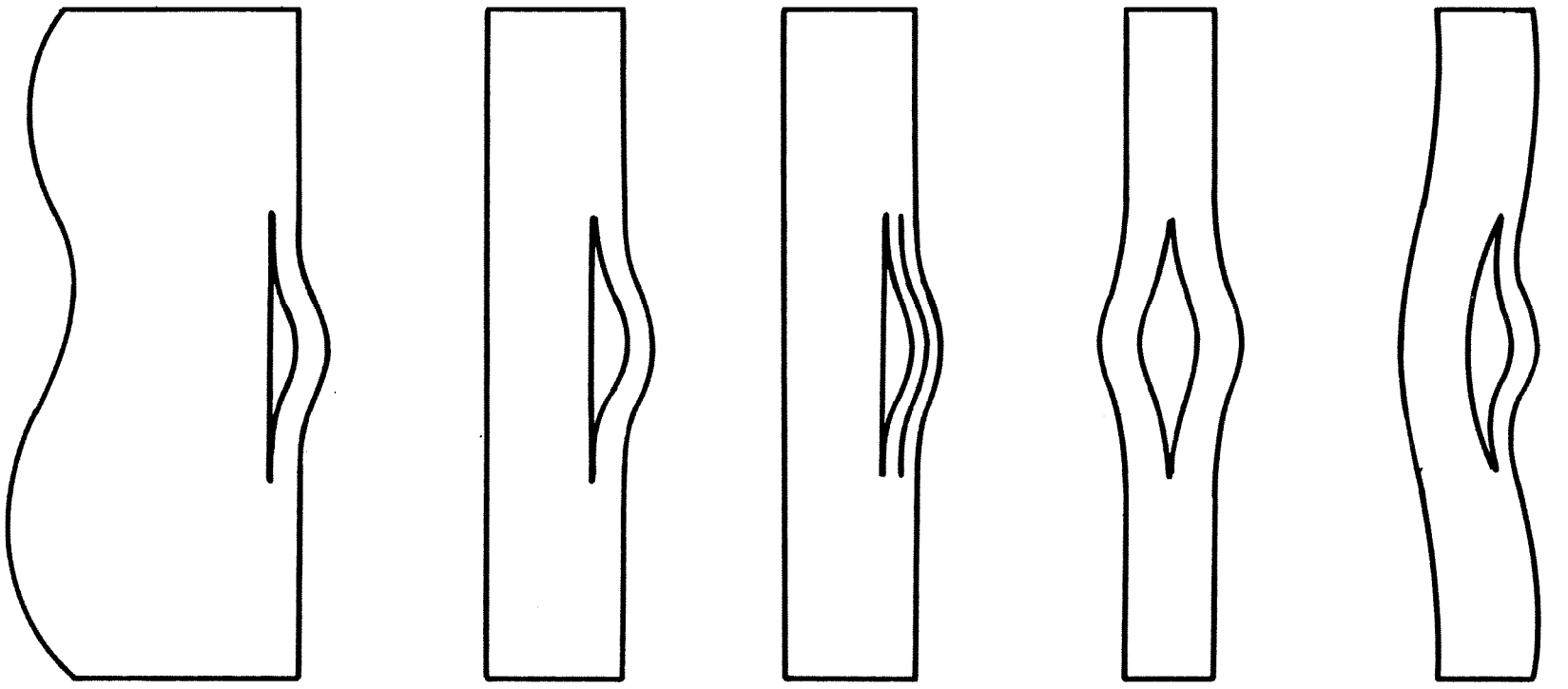

FIG. 2 DELAMINATION/BUCKLING MODELS

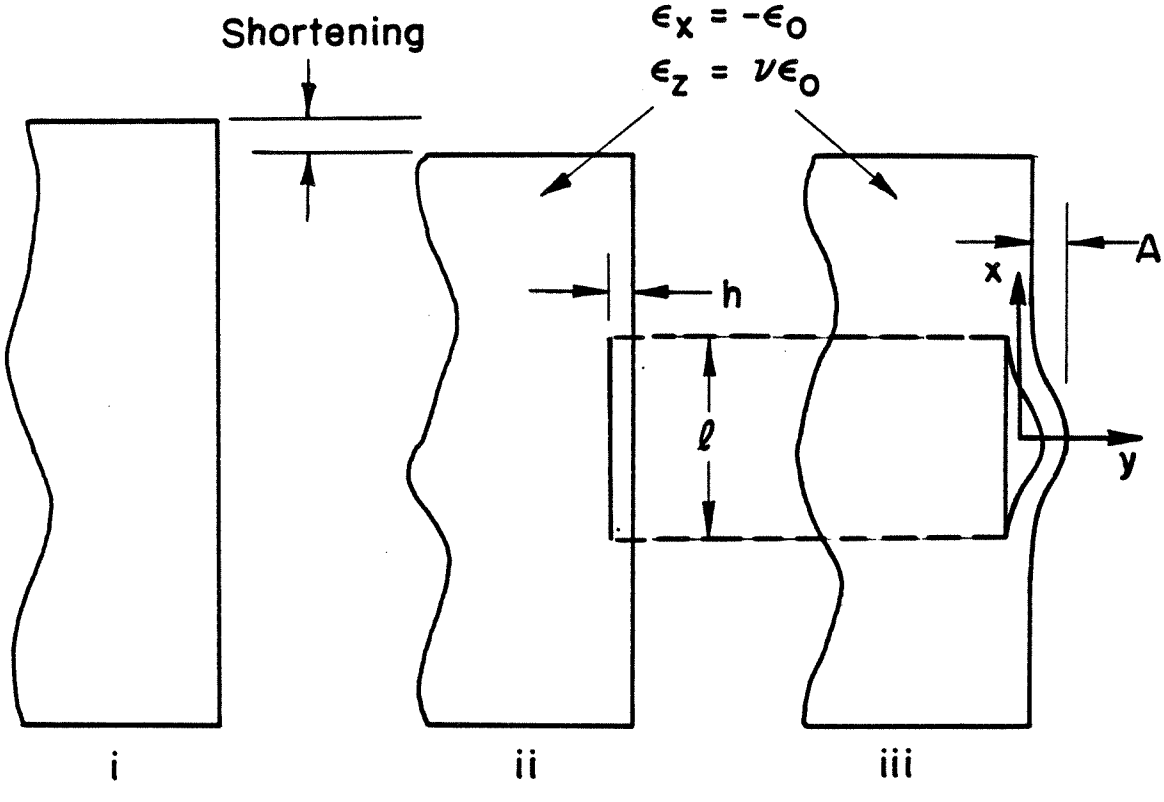

FIG. 3 THIN FILM MODEL - THREE CONFIGURATIONS

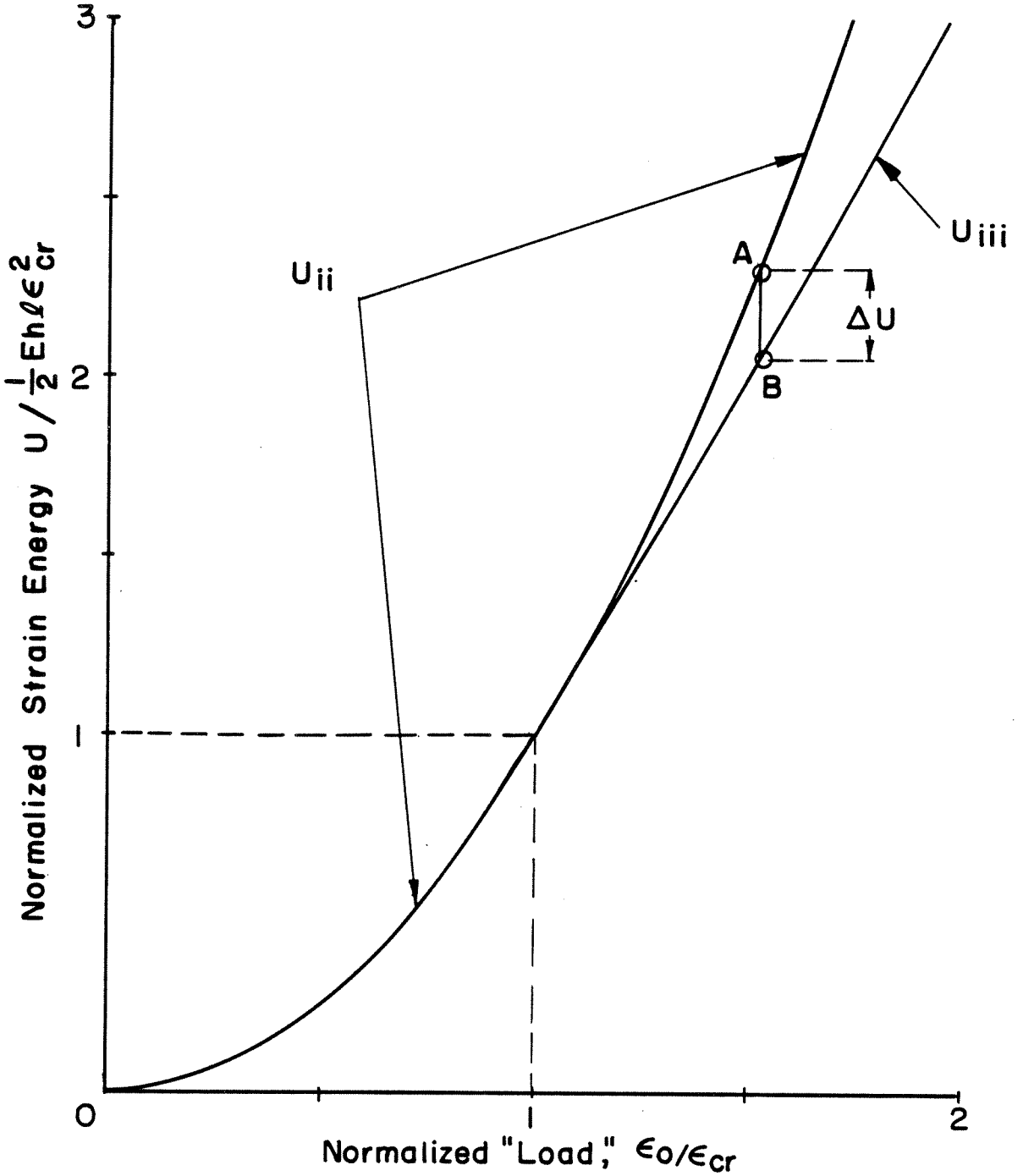

FIG. 4 STRAIN ENERGY OF THE DELAMINATED SECTION AS A FUNCTION OF LOAD

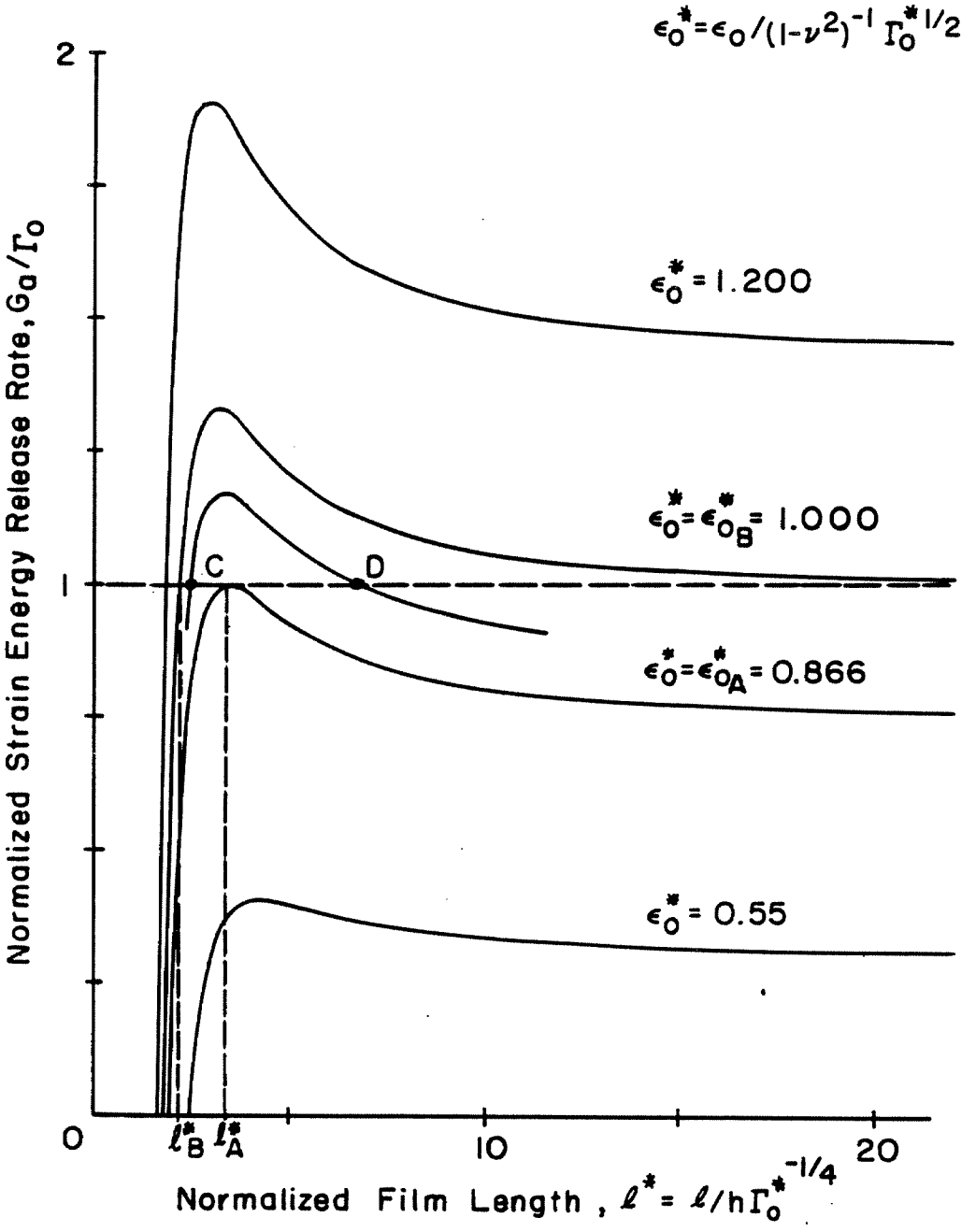

FIG. 5 THIN FILM MODEL-STRAIN ENERGY RELEASE RATE

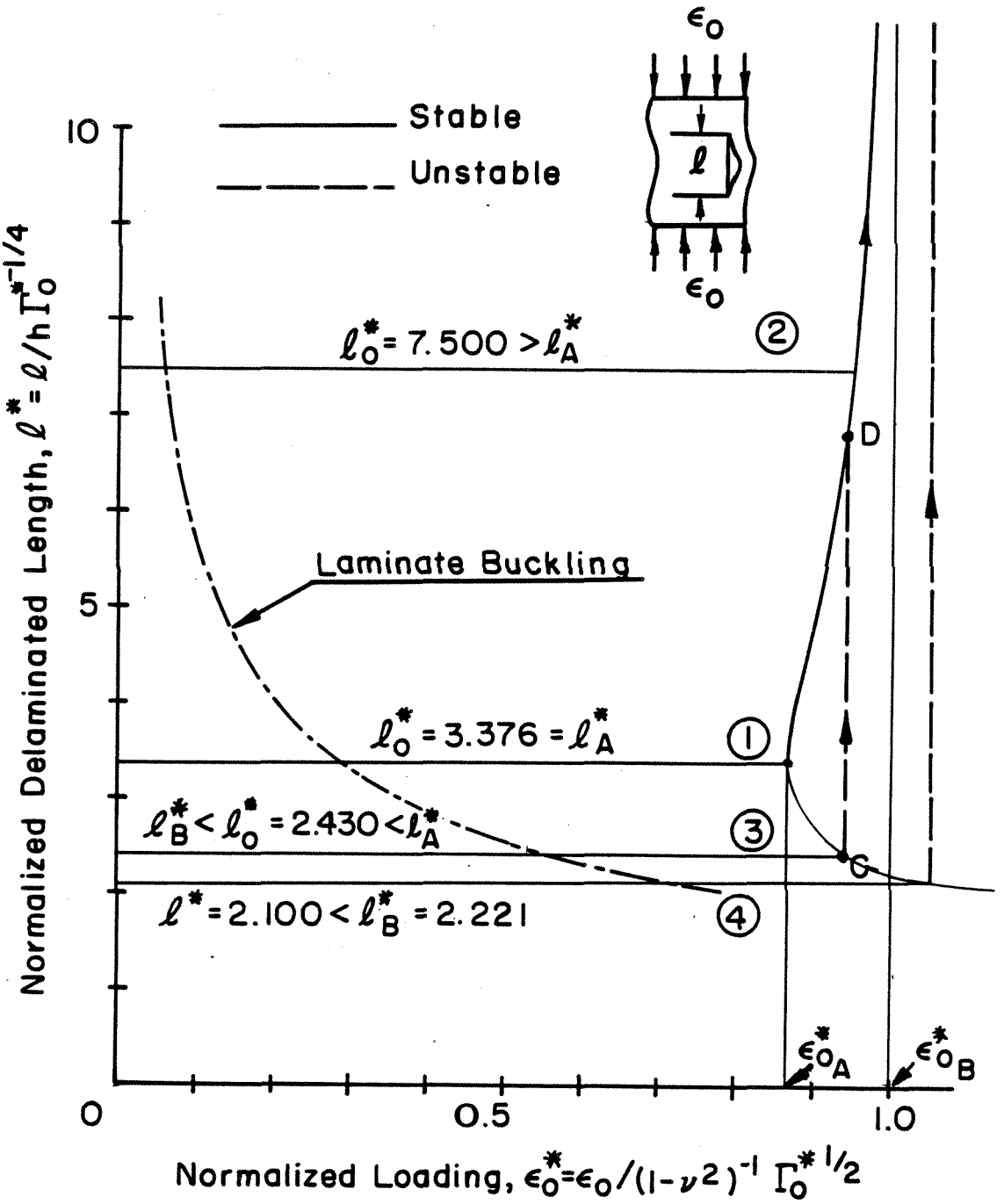

FIG. 6 DELAMINATED LENGTH AS A FUNCTION OF LOAD

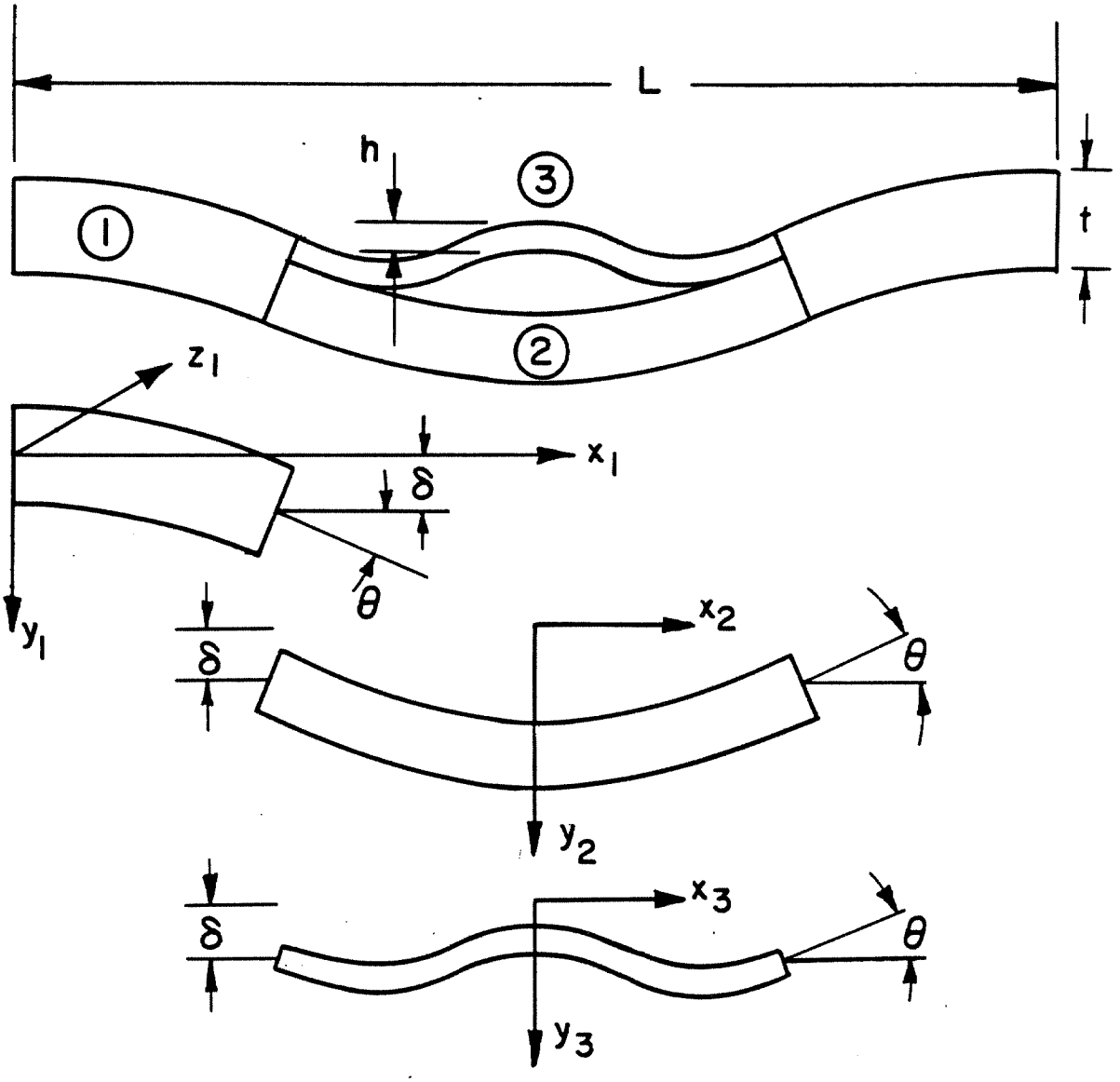

FIG. 7 COORDINATE SYSTEM FOR GENERAL PANEL PROBLEM

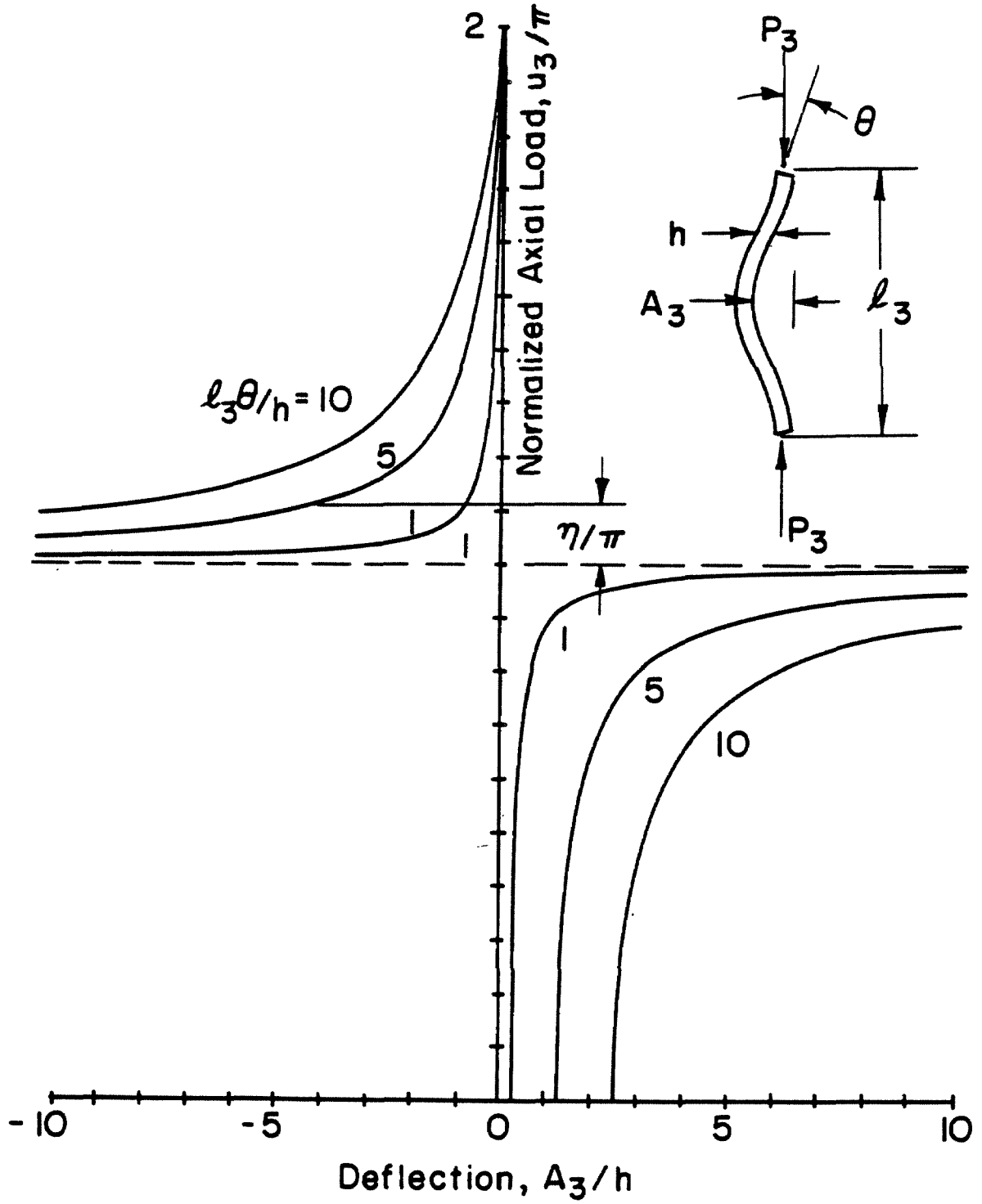

FIG. 8 EQUILIBRIUM POSITION OF SECTION 3

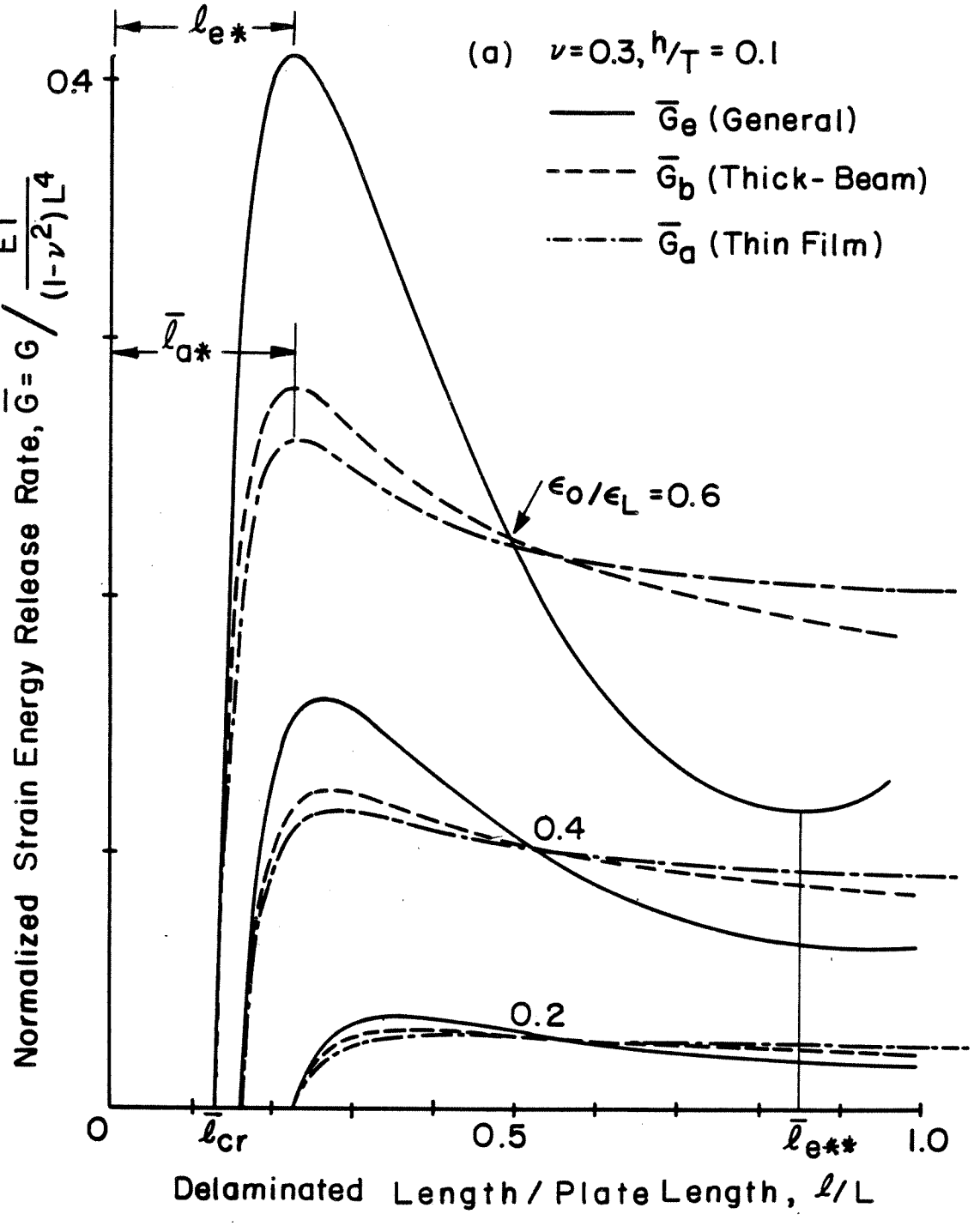

FIG. 9 STRAIN ENERGY RELEASE RATE - VARIOUS MODELS

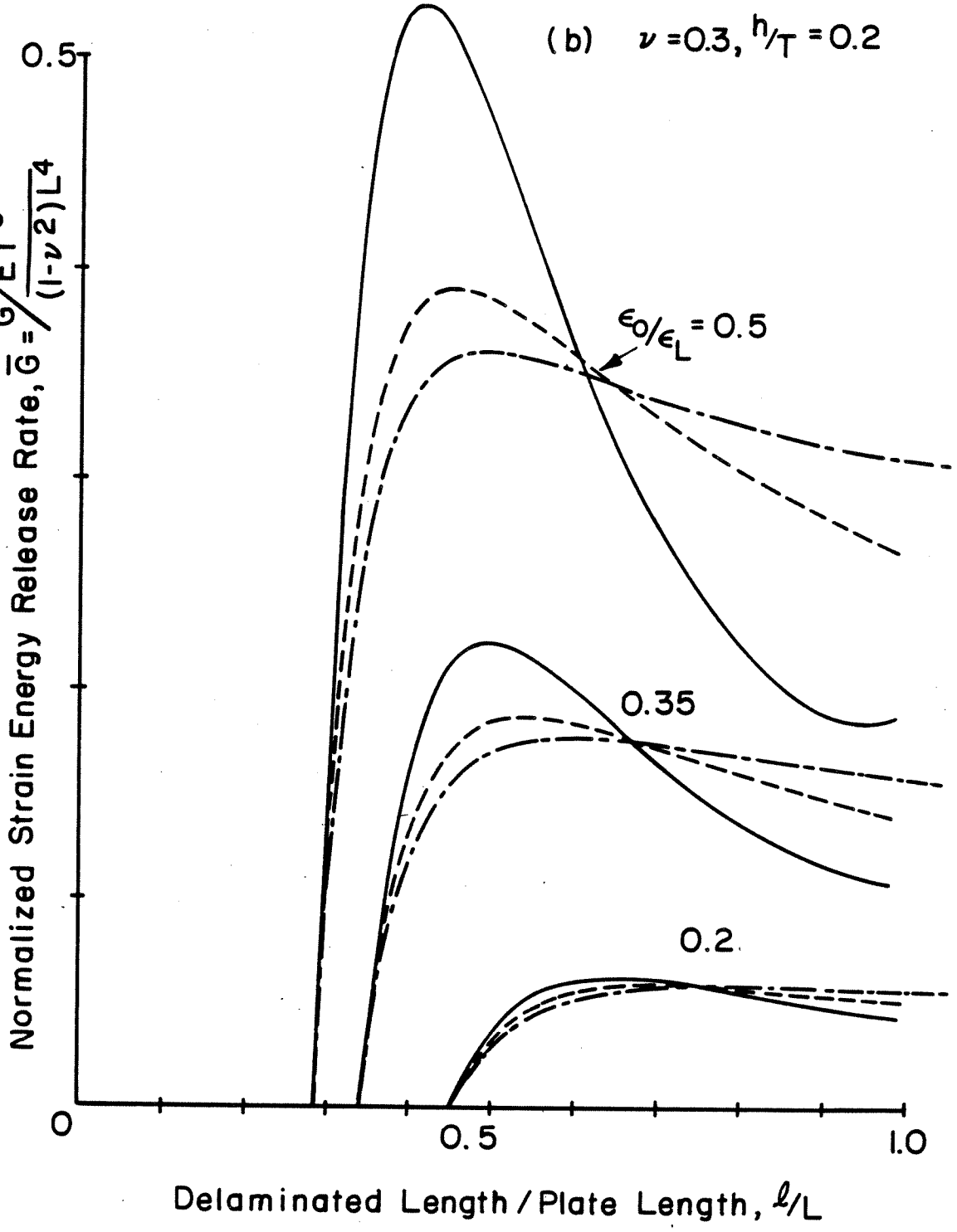

FIG. 9 CONTINUED

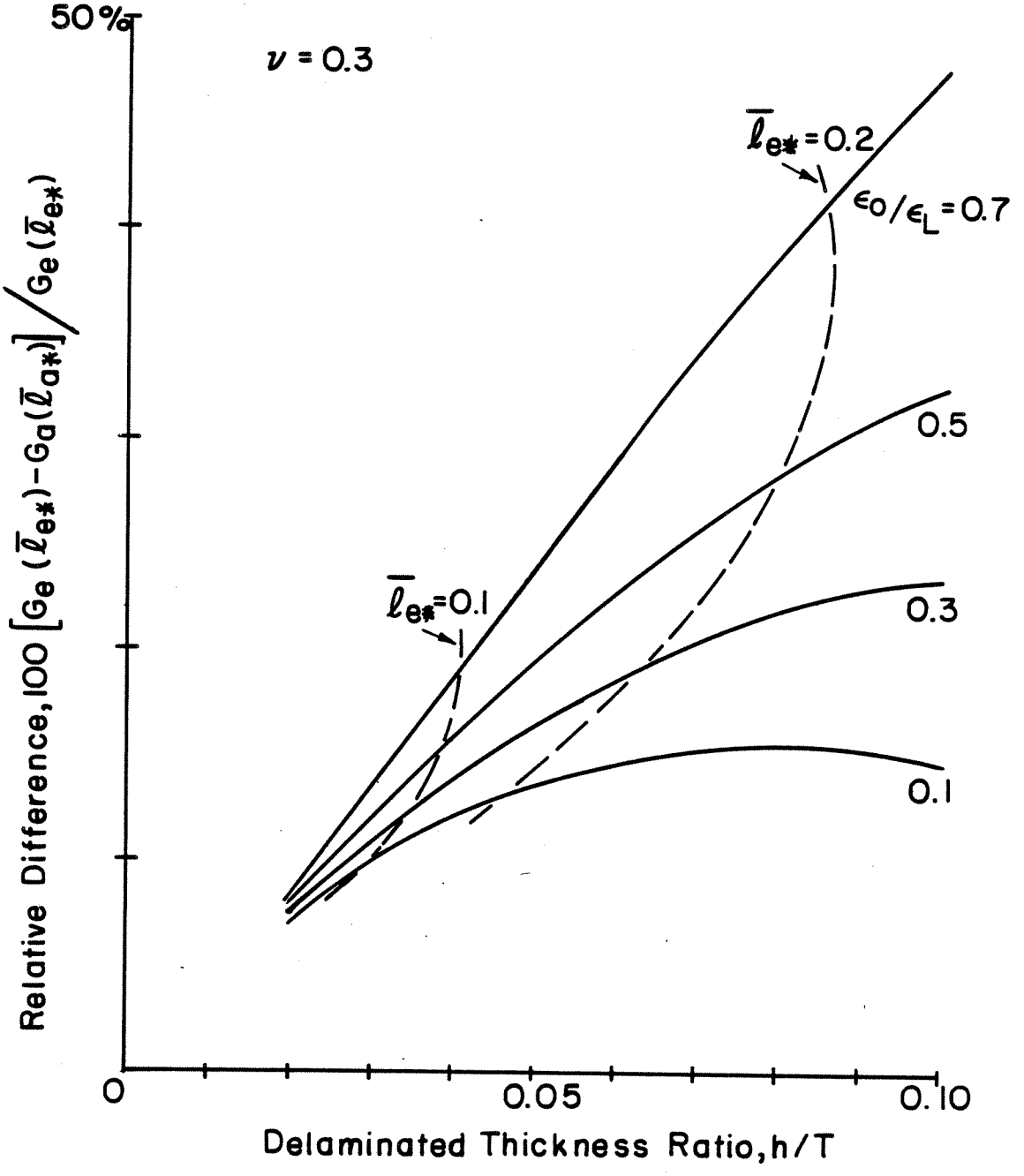

FIG. 10 RELATIVE DIFFERENCE BETWEEN THIN FILM AND GENERAL MODEL AS A FUNCTION OF THE CONTROLLING PARAMETERS

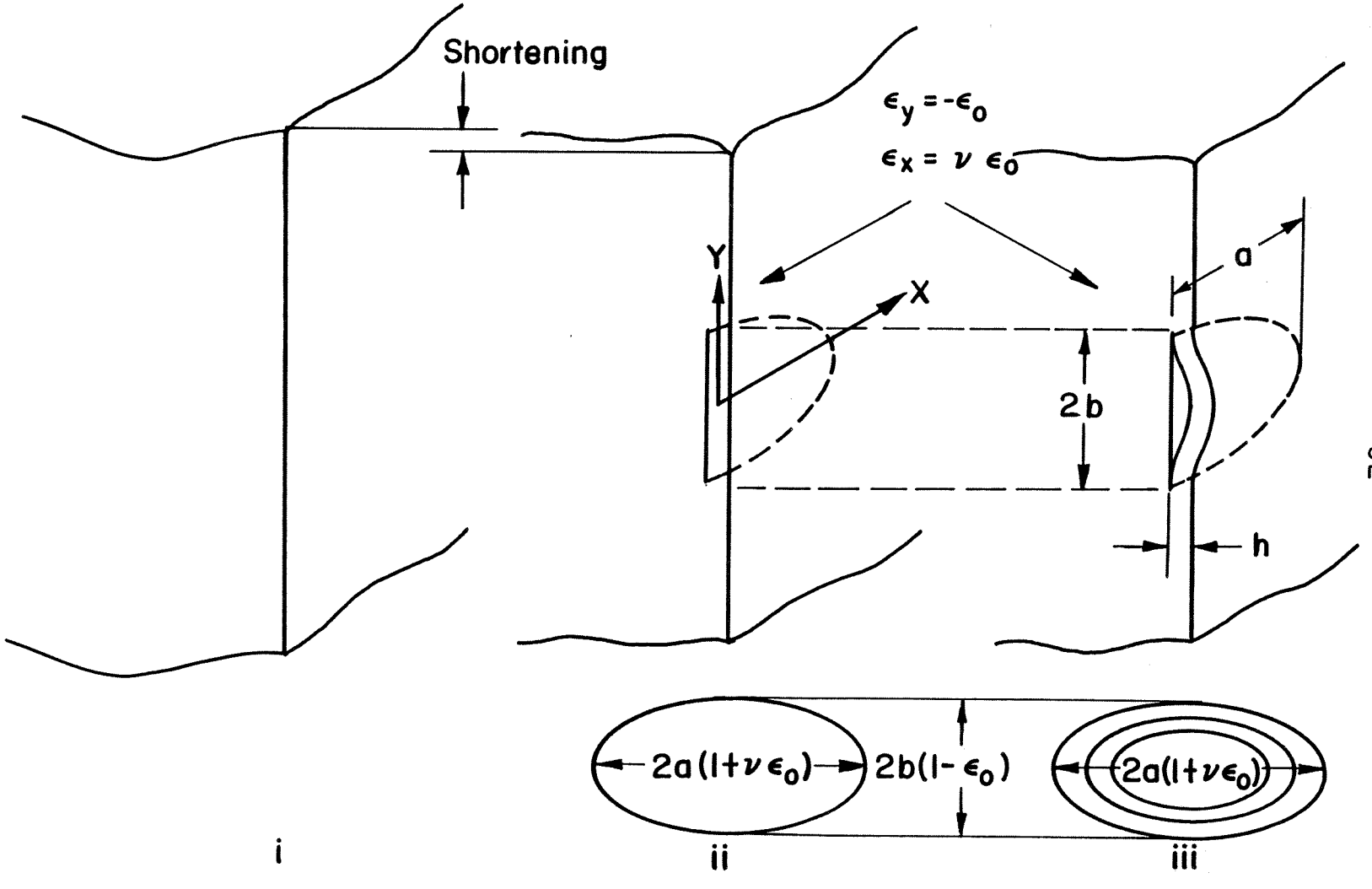

FIG.11 THIN FILM DELAMINATION - THREE CONFIGURATIONS

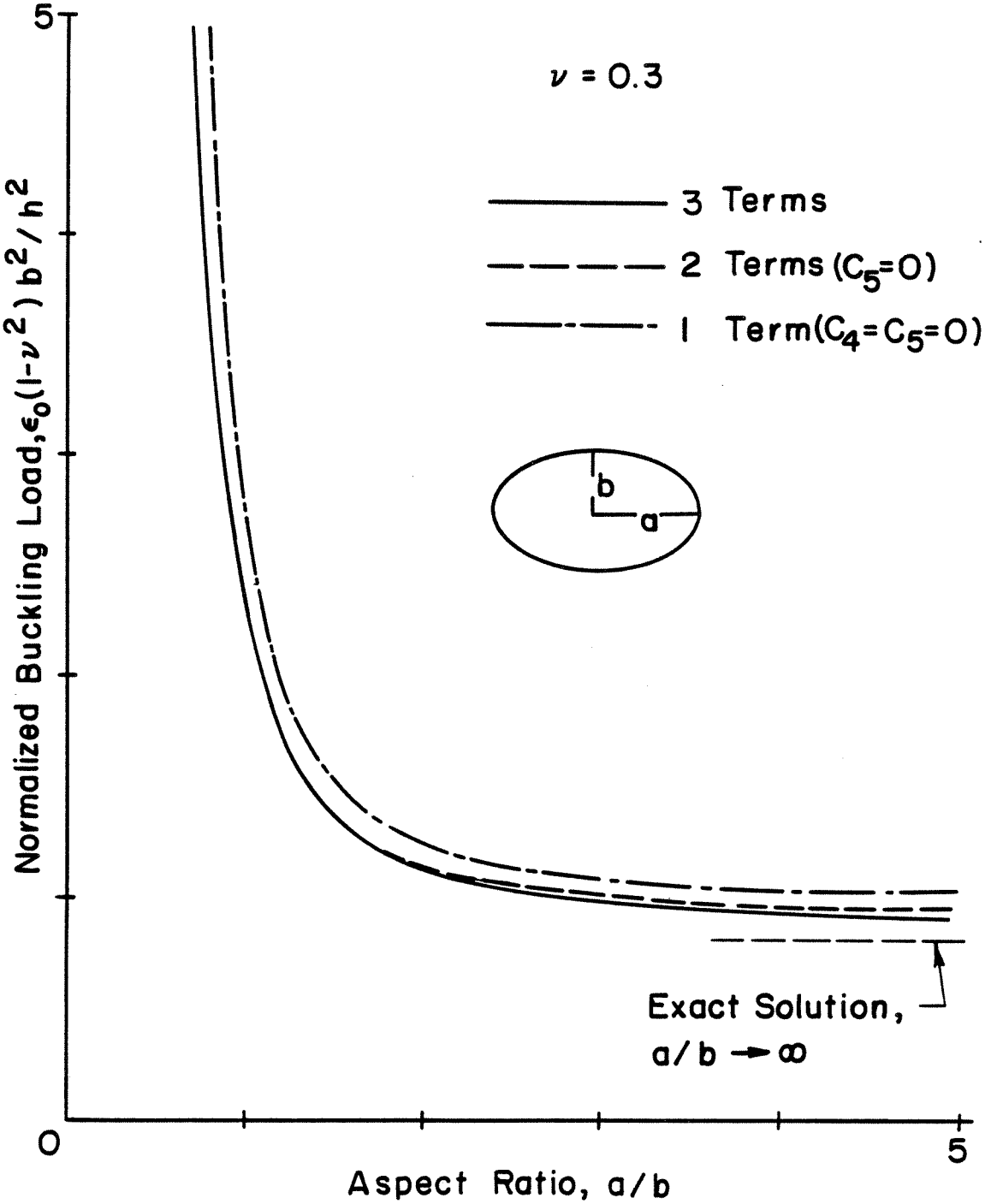

FIG. 12 BUCKLING LOAD – ELLIPTICAL DELAMINATION

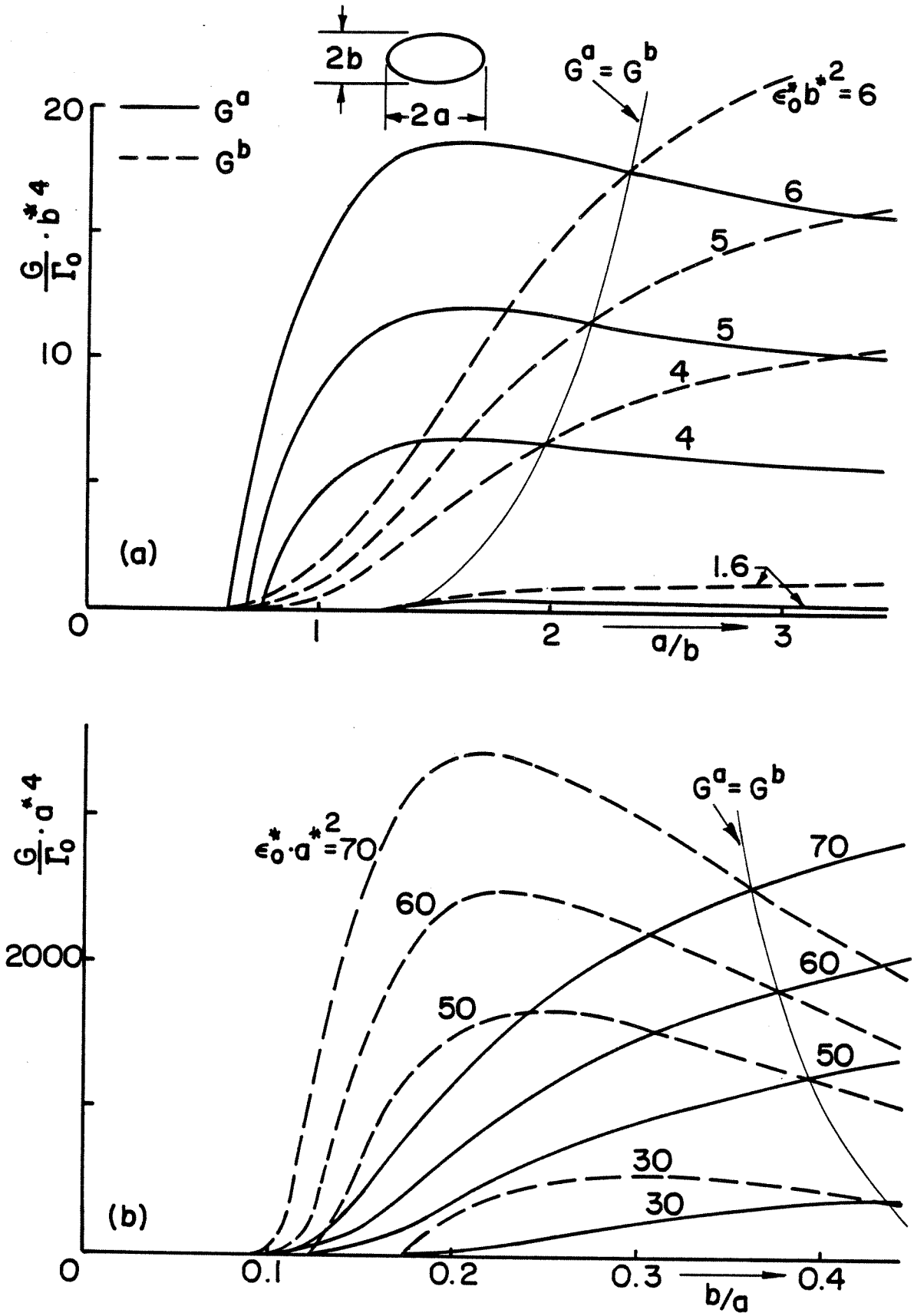

FIG. 13 STRAIN ENERGY RELEASE RATE, G

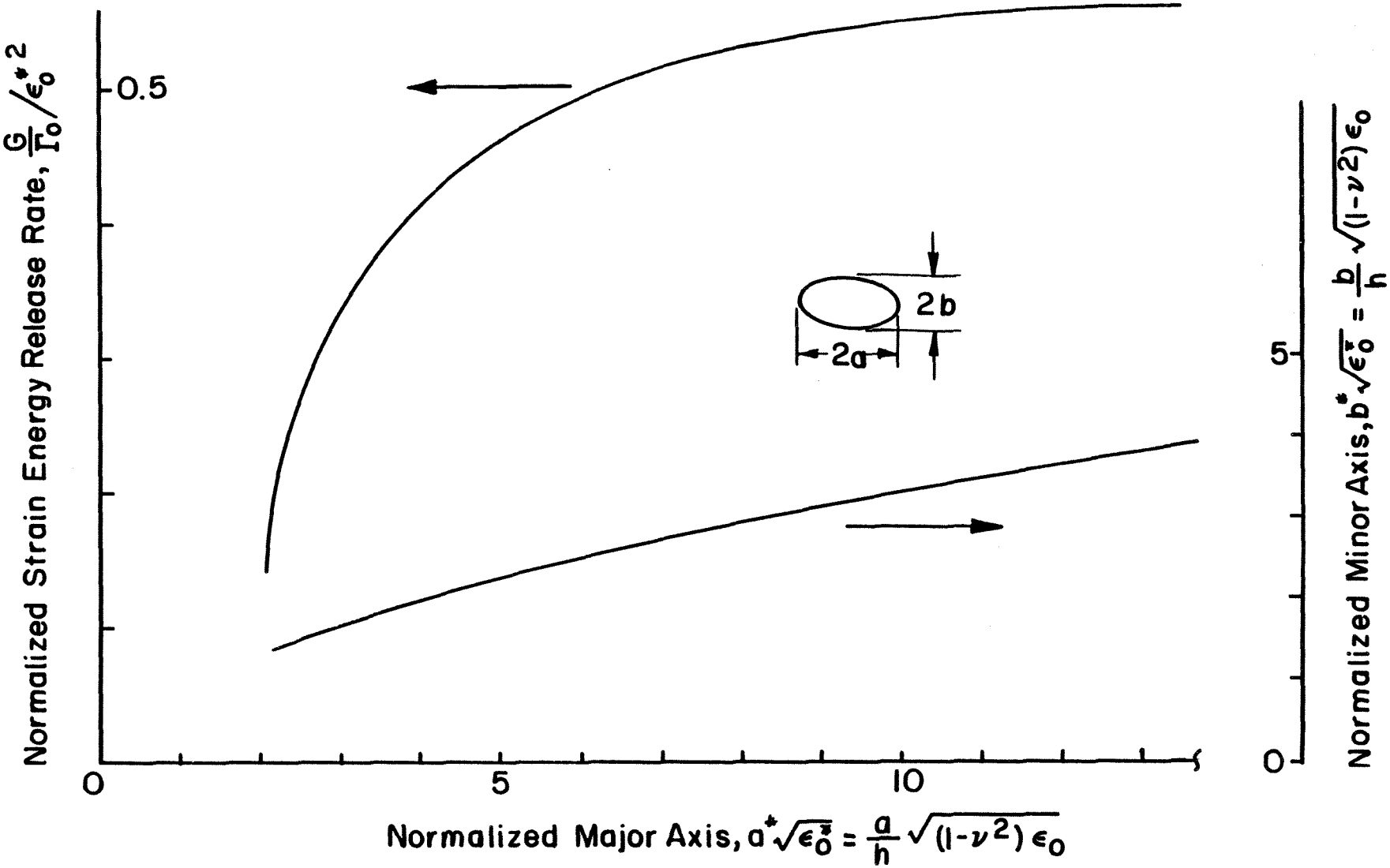

FIG. 14 STRAIN ENERGY RELEASE RATE AND GEOMETRY CONDITIONS ON THE PATH $G^a = G^b$

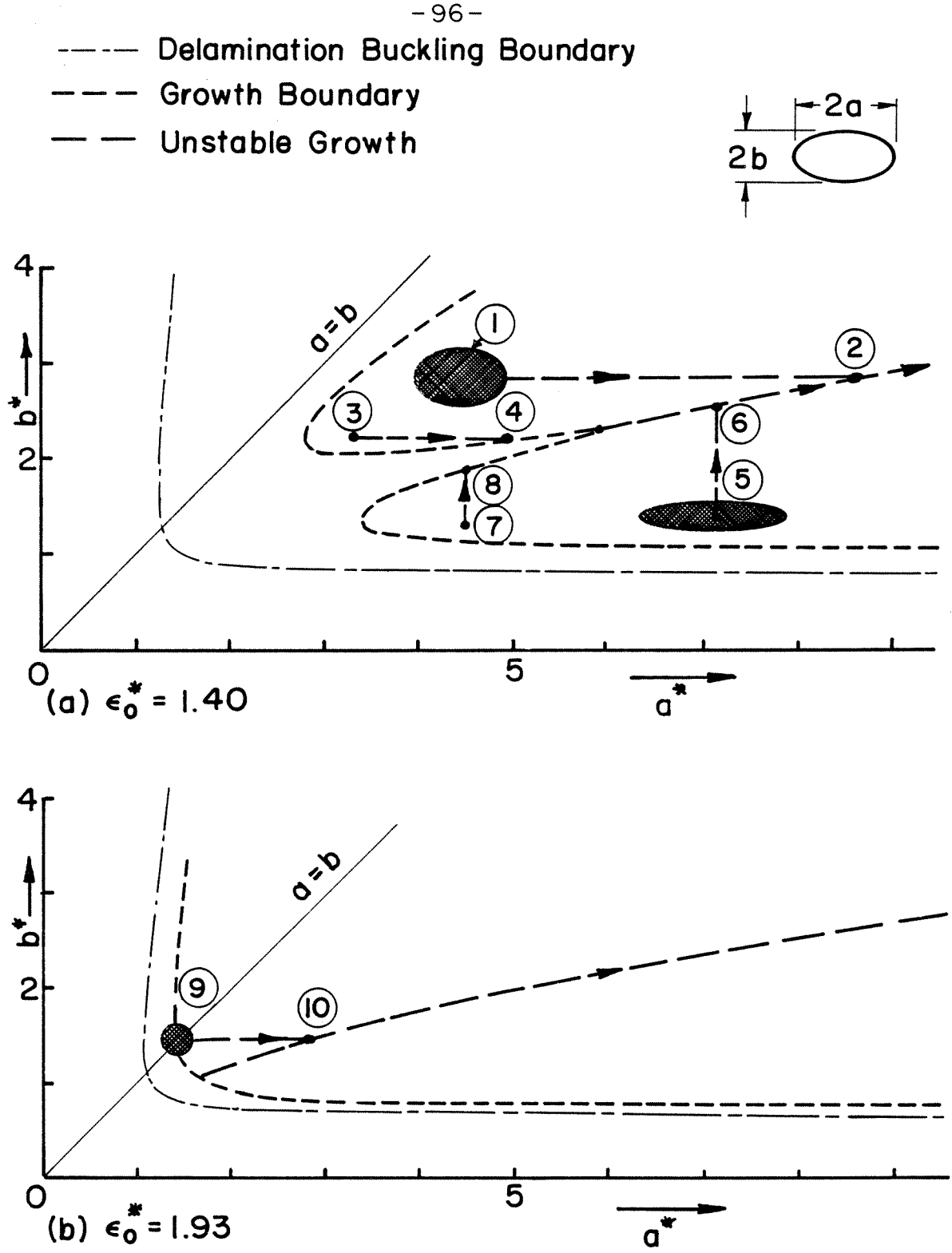

FIG. 15 DELAMINATION GROWTH UNDER CONSTANT LOADING

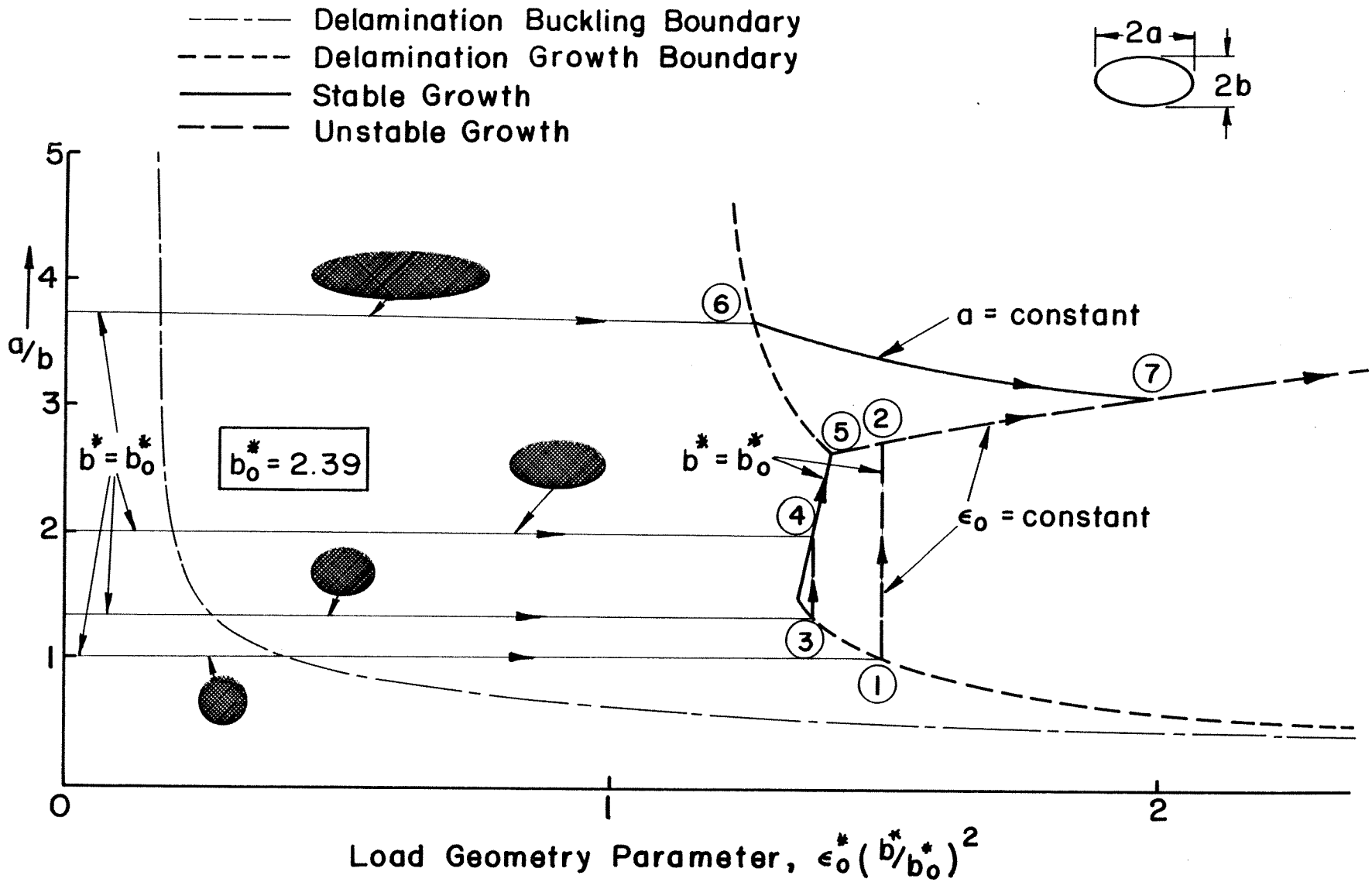

FIG.16 DELAMINATION GROWTH AS A FUNCTION OF LOAD

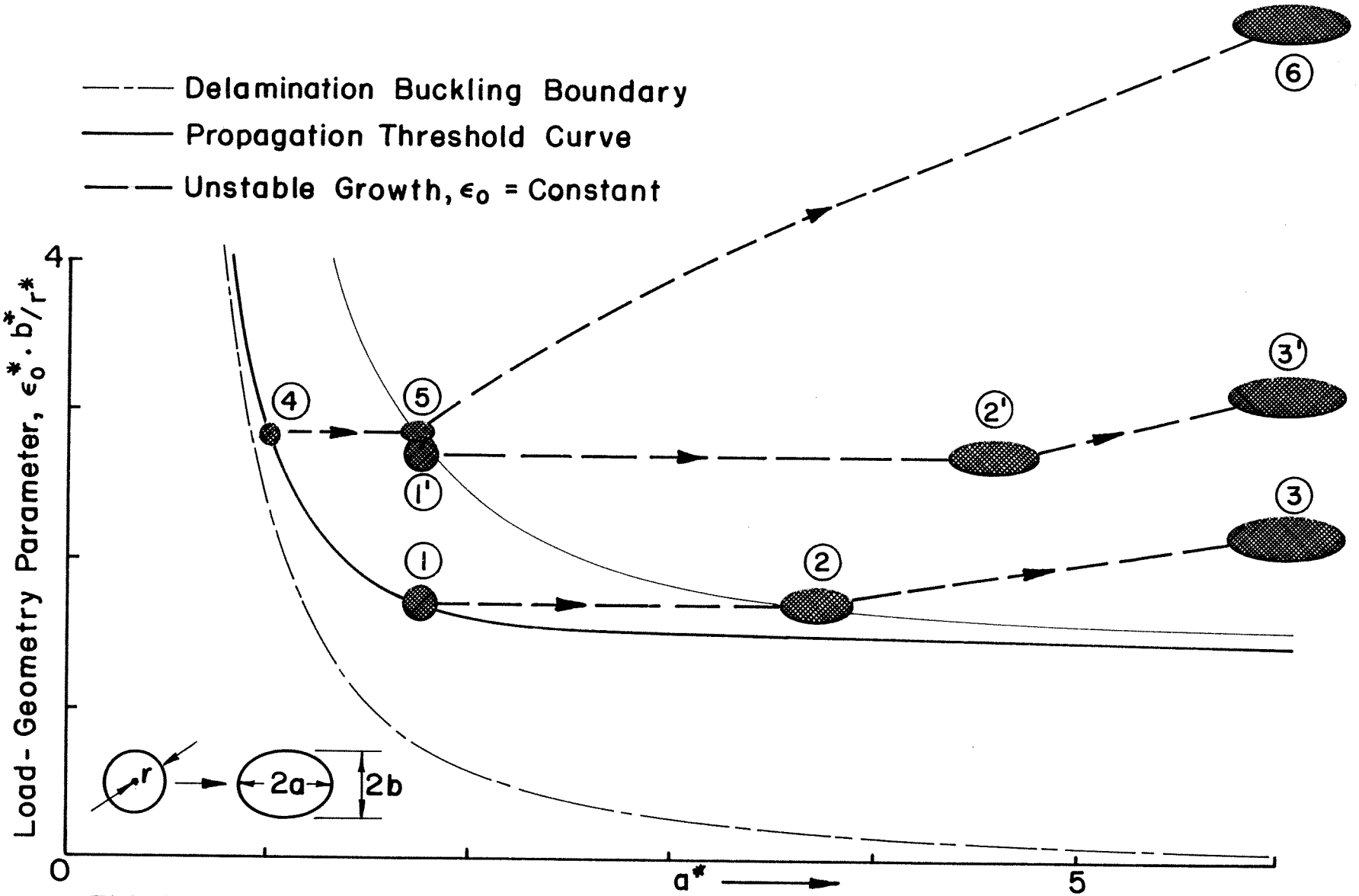

FIG. 17 THE GROWTH HISTORY OF A CIRCULAR DELAMINATION

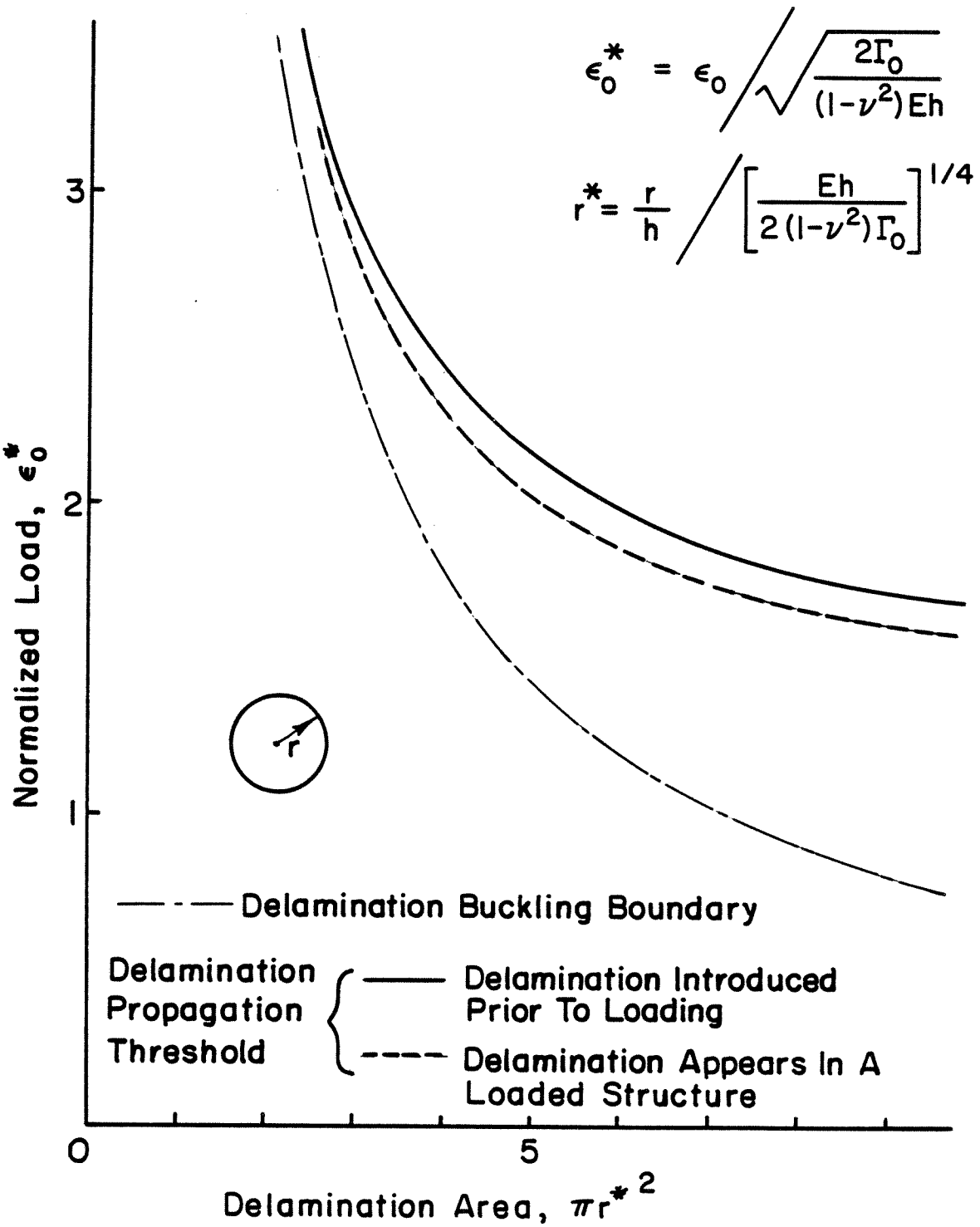

FIG. 18 THE PROPAGATION CONDITIONS OF A CIRCULAR DELAMINATION

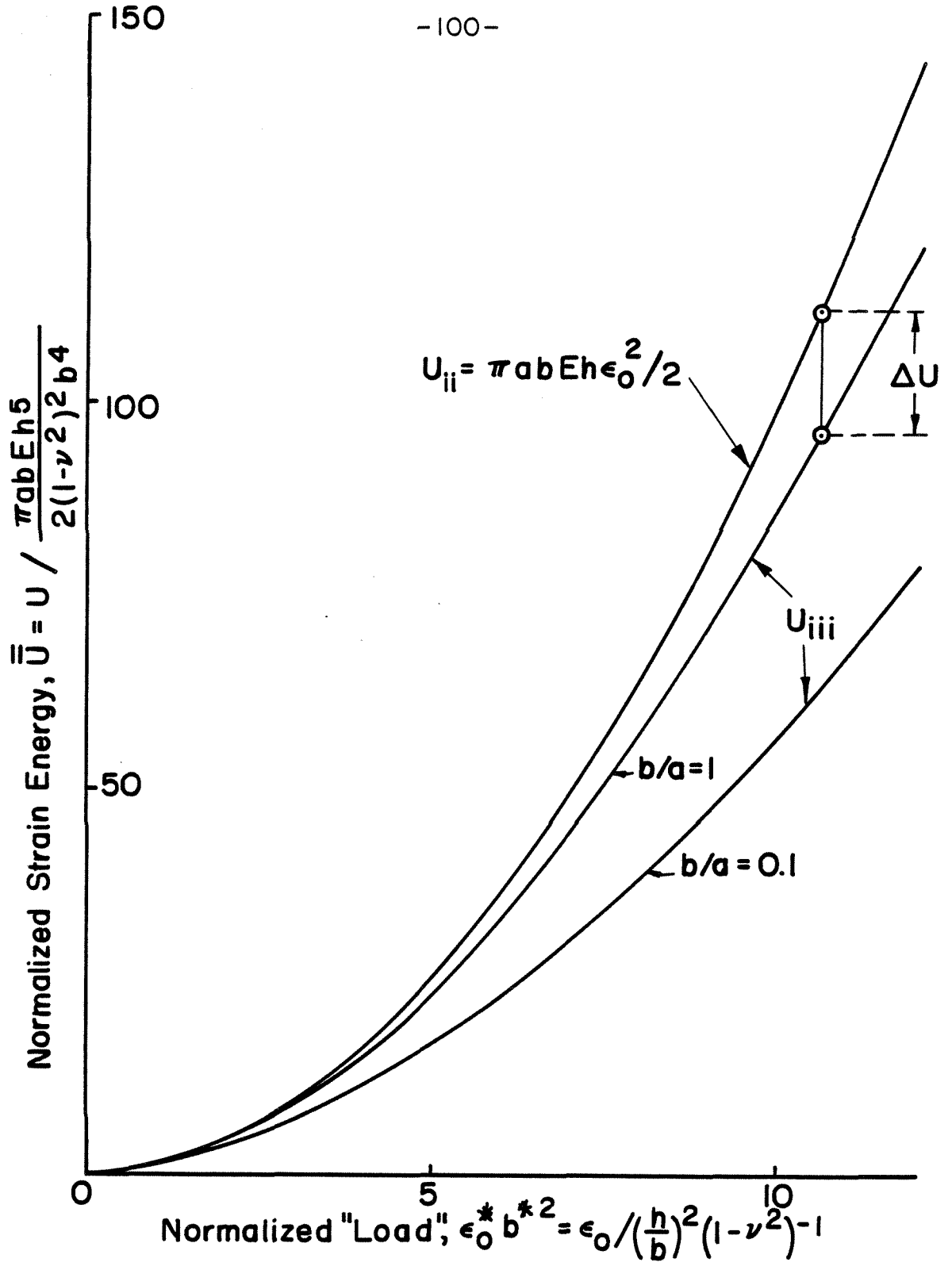

FIG. 19 STRAIN ENERGY OF THE DELAMINATED SECTION AS A FUNCTION OF LOAD AND GEOMETRY

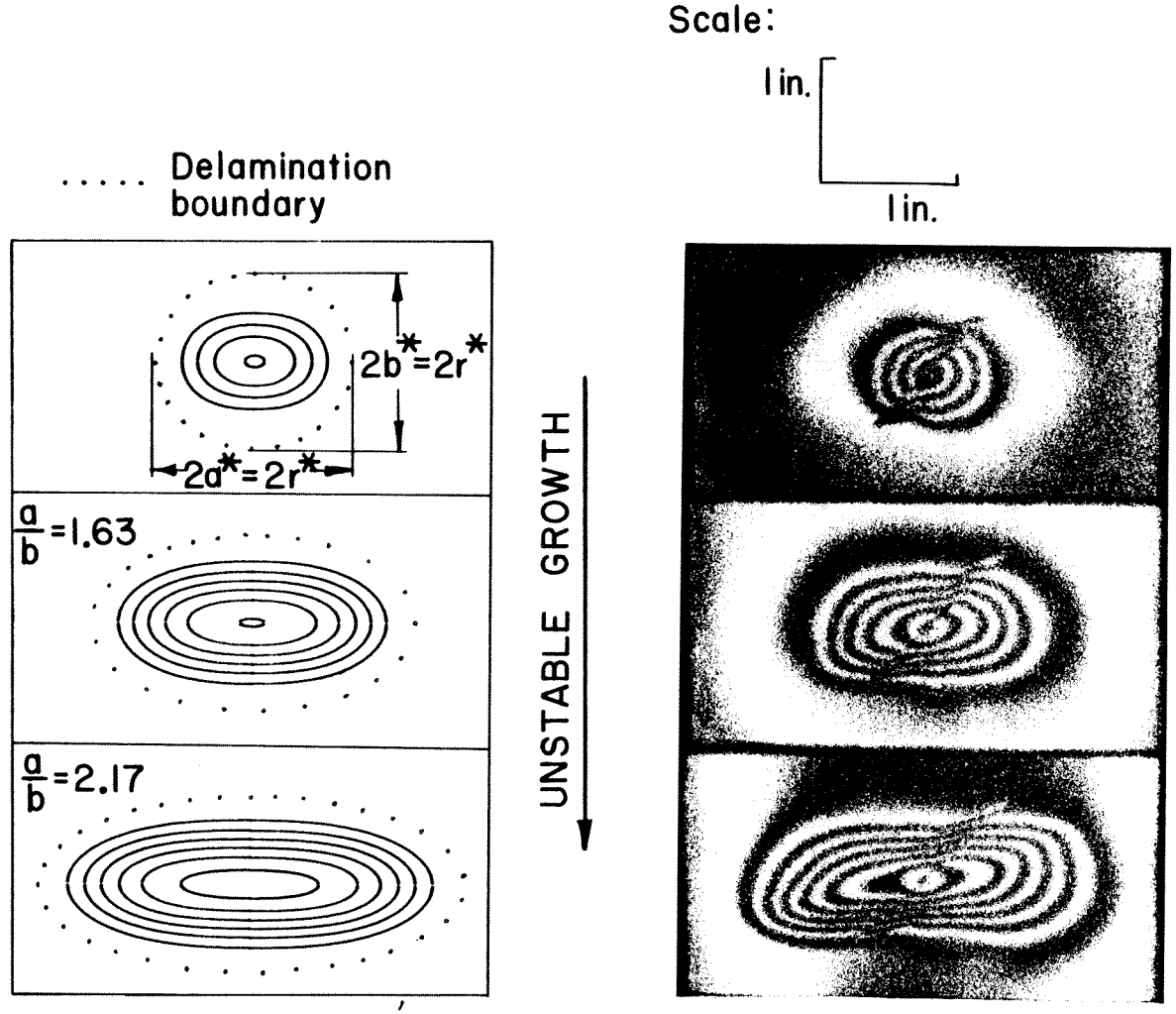

(a) $w/n = 0.31h$
$\epsilon_0^* = 1.69$, $r^* = 1.72$

(b) $w/n = 0.0126$ in., $\Delta t = 50\mu s$
$\epsilon_0 = 0.00326$, $V = 233$ ft/sec

FIG. 20 THE GROWTH PATTERN OF A DELAMINATION (a) AND IMPACT DAMAGE (b).

APPENDIX

EVALUATION OF FRACTURE ENERGY IN FIBER/EPOXY LAMINATE

AND

VISCOELASTIC CHARACTERIZATION OF THE NEAT RESIN

ABSTRACT

Impact experiments on compressively-loaded graphite/epoxy laminates carried out by various investigators have shown that a great improvement in damage growth tolerance can be achieved using certain epoxy resins. It was not very well understood, however, which specific resin property accounted for such an improvement. Post-impact damage growth observations in chapter 1, and subsequent modelling in chapter 2, have identified this property as the fracture energy associated with delamination. In this work, a modified cleavage technique is applied to evaluate this quantity for two composite materials of current interest, constructed from the same fibers but from different resins. The test results are then examined with reference to impact damage tolerance performance available for these materials.

The selection of matrix material is also influenced by other considerations such as long-term durability of the composite. Changes in environmental conditions (temperature, moisture, etc.) and time lead to changes in the mechanical properties of the matrix. This, in turn, can lower the fracture resistance of the composite. Therefore, the time-temperature behavior of the matrix material is needed in making a reliable selection. In this work, a viscoelastic characterization of the two resins of current interest is provided, and the results are examined with reference to long-term applicability.

TABLE OF CONTENTS

3.1 INTRODUCTION

The growth or arrest of impact damage in a compressively-loaded laminate is affected by the fracture energy of the composite. The fracture energy depends on both the fiber and the resin used in fabricating the composite material. A good selection of these components will not only reduce impact induced delaminations but also prevent existing ones from propagating. When considering the fracture energy of a fiber-resin type system, a distinction between the fracture energy of the composite system and that of the neat resin should be noted. While the latter is associated with a cohesive failure, the former more likely depends upon the adhesion quality between the specific fiber and resin. In this work, the fracture or delamination of the composite material is considered using the Double-Cantilever-Beam technique. This test geometry resembles the delamination-buckling beam geometry, which its fracture energy is of concern in this investigation.

The peel testing technique, originally developed by Obreimoff [1] to evaluate cleavage surface work of Mica, has been used with variations by many investigators to measure both cohesive fracture energy of monolithic materials as well as adhesion bond strength of resins [2-8]. In this method the adhesion problem is approached with a specimen having a simplified geometry as in fig.1a. Test results are concerned with net forces acting on the simple structure and the resulting large deformation under the load, both of which are easily measured with a standard testing machine, thus one avoids dealing with the details of stress distribution around the crack tip. This advantage is particularly meaningful in the present application which deals with the laminated specimen shown in fig.1b, where there are the additional complexities of material inhomogeneity and anisotropy.

The selection of epoxy resin is not only influenced by its performance at normal service conditions but also by its response to environmental changes. Most resins are polymers and possess viscoelastic time-dependent properties. Changes in resin mechanical properties may lead to changes in the fracture resistance of the composite. Thus a local delamination which may not grow immediately after impact can suffer a delayed fracture as the environmental conditions are changed. The severity of such a situation is perhaps most pronounced in the low-velocity impact range where, while an internal damage may exist in the composite, its surface may appear unharmed. Failure might then be developed with time and/or at elevated temperature.

The analysis of a delayed fracture in a composite resulting from changes in time, temperature, moisture, etc. is a subject of investigation by itself, and is considered beyond the scope of this work. Some information regarding this matter can be achieved, however, by examining the viscoelastic behavior of the material constants. This behavior is evaluated here for two matrix materials of current interest through shear compliance measurements. In general, two material functions are needed to fully characterize the material response. Since, however, the bulk response typically varies much less over the glass-to-rubber transition than the shear, it is often justified to approximate the bulk modulus as a constant. In this event, the shear behavior characterizes the viscoelasticity of the material completely.

3.2 EVALUATION OF FRACTURE ENERGY IN FIBER/EPOXY LAMINATE

This part is concerned with the determination of interlaminar fracture toughness in a composite laminate, in particular T300/5208 and T300/BP-907. These two graphite/epoxy systems are considered candidates for use in aerospace applications, and a large amount of impact damage tolerance data is available for comparison purposes.

The fracture toughness is measured using the cleavage technique. Section 3.2.1 deals with the cleavage analysis. The test procedure is outlined in section 3.2.2 and test results and discussions are given in section 3.2.3.

3.2.1 Cleavage Analysis

This section develops a cleavage analysis for the laminated specimen shown in fig. 1b. The specimen is composed of several plies which, while all arranged parallel to each other, may possess different axes of symmetry. Before dealing with this problem it appears prudent to consider first the simpler analogues shown in fig. 1a. The specimen in fig. 1a consists of a pair of long rectangular beams cemented together over some length, leaving a portion of length l uncemented. Assuming that the specimen behaves like a pair of cantilever beams of length l measured from the point of loading, and making use of the technical theory of beams (while neglecting shear deformation), one has

$$C \equiv \frac{\delta}{P} = \frac{2l^3}{3EI} = \text{Compliance} \tag{1}$$

$$U = P\frac{\delta}{2} = \frac{3EI\delta^2}{4l^3} = \text{Strain Energy} \tag{2}$$

where E is the Young's Modulus, I is the beam cross-section moment of inertia, P is the load and δ is the total deflection under the load (cf. fig. 1a).

Next, the strain energy release rate, G, (on a per unit area basis) is calculated

using the condition that the crack extends from l to $l + \Delta l$ while the specimen ends are held fixed (i.e. δ remains fixed). An energy balance gives

$$G = \lim_{\Delta l \to 0} \frac{[U(l) - U(l+\Delta l)]}{b\Delta l} = \frac{-1}{b}\left[\frac{\partial U}{\partial l}\right]_{\delta} \tag{3a}$$

or

$$G = \frac{9EI\delta^2}{4bl^4} = \frac{3P\delta}{2bl} \tag{3b}$$

where b is the specimen width. Equation 3b indicates a decrease in the strain energy release rate, G, with increasing crack length l. Crack extension is possible when $G \geq \Gamma_0$, where Γ_0 is the energy required to produce a unit of new surface in the splitting process. In a cleavage experiment the deflection δ is increased at a constant and slow rate; fracture occurs when l becomes sufficiently large, i.e. such that G reaches the value Γ_0. Thereafter "stable" crack growth occurs with G retaining its value Γ_0. Thus, successive P, δ and l measurements during crack growth allow several determinations of Γ_0 with a single specimen.

Experimental values of compliance in cleavage tests show that in addition to the deflection due to bending (and shear), some deflection also occurs due to rotation at the assumed "built-in" base of the beam [2]. Mostovoy et al. [6] proposed the replacement of the actual crack length by an effective one (larger) which best fits the data. Berry [5] has treated this discrepancy by adopting the following compliance-crack length relation:

$$C = al^n \quad , \quad a = f(EI) \tag{4}$$

For the relation given in (4), it is easy to show that

$$G = \frac{nP\delta}{2bl} \tag{5a}$$

or, during a quasistatic growth

$$\Gamma_0 = \frac{nP\delta}{2bl} \tag{5b}$$

where n is a constant found from compliance calibration, i.e. n is found from

$$\text{Log } C = \text{Log } a + n \text{ Log } l \tag{6}$$

It is noted that for a true cantilever n=3 while the value found by Berry [5] and others is on the order of 2.7 .

An attempt to clarify the discrepancy mentioned above will now be presented. Suppose that the assumed "built-in" support at the beam base is replaced by a "spring" type rotation, so that the following holds

$$M_0 = Pl = k\varphi \quad , \quad \varphi = \frac{\delta}{l} \tag{7}$$

where M_0 is the moment at the beam base, φ is the rotation there and k is the spring constant. With shear deformation included, the compliance takes the form

$$C = \left[\frac{h^2 l}{4IG_0} + \frac{l^2}{k} + \frac{2l^3}{3EI} \right] \tag{8}$$

where G_0 is the shear modulus. The first, second and third terms in the bracket are deflections due to shear, base rotation, and bending, respectively. It is seen from (8) that the shear term dominates as $l \to 0$, the bending as $l \to \infty$ and the rotation term has its effect in the transition range. For a crack long compared to the beam thickness, the shear term can be dropped out and the compliance depends upon powers of 2 and 3 in l. Thus the relation proposed by Berry which yielded n = 2.67 in his experiment may represent a compromise between the two dominant powers in l.

The analysis of the problem at hand shown in fig. 1b is treated in an analogues manner to that of fig. 1a. Let

$$\delta = \delta_1 + \delta_2 \tag{9}$$

Assuming a sufficiently long crack, and following Berry's correction, let

$$C_1 \equiv \frac{\delta_1}{P} = a_1 \ell^n \qquad C_2 \equiv \frac{\delta_2}{P} = a_2 \ell^n \tag{10}$$

where the subscripts 1 and 2 refer to beam 1 and beam 2 in fig. 1b, respectively. Equation 10 implies that $a_2\delta_1 = a_1\delta_2$. Using this relation and (9) give

$$\delta_1 = \frac{\delta}{(1+a_2/a_1)} \quad , \quad \delta_2 = \frac{\delta}{(1+a_1/a_2)} \tag{11}$$

Substituting (11) in (10) leads to

$$C \equiv \frac{\delta}{P} = (a_1 + a_2)\, \ell^n \tag{12}$$

This relation is identical to (4) derived for the case in fig. 1a (except for a constant) and so the strain energy release rate for the present case is also given by equation (5) which was derived for the prototype specimen (fig. 1a).

3.2.2 Test Procedure

Two groups of graphite/epoxy composites, namely T300/5208 and T300/BP-907, referred to here as material A and material B, respectively, were tested. The specimens were cut from a 48-ply $(+45/-45/0/0/+45/-45/0/0/+45/-45/0/90)_{2s}$ laminates supplied by NASA-Langley. The cuts were made along the 0^0-ply axis. The test specimens were 10 in. long and 0.2-0.4 in. wide. Both materials A and B were fabricated from the same graphite fibers, thus permitting a direct evaluation of the effect of the resin material on the fracture toughness of the composite. Laminates of material B were 18% thicker than laminates of material A, mainly due to the higher resin content (38% vs. 28%). A crack approximately 2 in. long was introduced either along the beam midplane or away from it using a razor blade. The specimen ends were then separated in an Instron machine, through gripping as illustrated in fig. 1a, at a constant rate of

0.05 in./min. . The load and deflection were continuously recorded on a chart-recorder. After the deflection had reached the critical value needed for crack initiation, the crack grew, usually in a "stick-slip" fashion. Crack length measurements were taken during crack growth. The tests data for four specimens, two for each material tested, are summarized in table I.

3.2.3 Test Results and Discussions:

In order to understand the fracture behavior, a photographic survey was carried out for all specimens. Fig. 2a shows three photographs of specimen #A1 (T300/5208 composite). It is clear from fig. 2a(I) that the crack has not maintained a plane surface, and a "zig-zag" type surface is evident along the entire specimen gauge length. A top view and a view at an angle of a typical surface variation are shown in fig. 2a(II) and fig. 2a(III), respectively. It can be seen that the fracture is confined to the 90^0-ply region at the beam center, and is bounded by the adjacent 0^0 plies. The characteristic fracture surface has a "trapezoidal" section with two plies in height (0.01 in.) and approximately ten plies in length (0.05 in.). This surface has no thickness variations (see fig. 2a(III)), and it is aligned with the 90^0 ply direction. The fracture consists of 0^0 - 90^0 interfacial separation (debonding), as well as failure within the 90^0-ply region. Because of the through-the-thickness uniformity of the fracture surface inside the 90^0-ply region (fig 2a(III), the failure in this region is interpreted as a fiber-matrix adhesion failure, with no actual fiber rupturing. The fracture pattern for test #A2 (T300/5208) was quite different. Fig. 2b shows that the fracture surface has a "channel" type section with the "channel" wall being 1 ply deep (the 0^0 ply). The "channel" is approximately 0.12 in. wide (about half the total beam width). The fracture at the "channel" section consists of a 0^0 - 90^0 interfacial separation, plus shearing off failure at the "channel" wall. The other parts of the failure surface consists of a 0^0 - -45^0 interfacial separation. As in test #A1, no fiber

rupturing took place.

The fracture process in the T300/BP-907 composite was quite different in both the fracture pattern and the fracture mechanism. Fig. 2c shows the results for test #B1. The delamination was largely confined to the 90^0-ply region at the center of the beam. Unlike in test #A1, however, the crack has penetrated the adjacent 0^0 plies at several locations (three at all). This is demonstrated in fig. 2c(II). Also, in the 90^0-ply region the fracture surface is not a plane surface (see fig. 2c(III)), and therefore is not aligned with the 90^0 plies. This indicates the basic difference in the fracture behavior between the T300/5208 and the T300/BP-907 composites. In the T300/5208 fracture is characterized by interfacial separation while the fracture in the T300/BP-907 is characterized by fiber rupturing. The fracture process in test #B2 was quite similar to that of test #B1. In this test, fracturing away from the main crack has occurred. This is shown in fig. 2d(II). The main crack and the secondary crack in this print are separated by the 0^0 ply. The secondary crack grew about 0.5 in. before it coalesced with the main crack again.

The information given in Table I is used to determine the fracture energy. First, the constant n is determined by plotting the logarithm of the compliance inverse versus the crack lengh logarithm, in accordance with (6). This is done in fig. 3 for the four specimens. The constant n, indicated by the slope of a straight line best fit through the respective data points, ranges from 2.58 to 2.85. These values are smaller than the value 3 for a true cantilever. Next, the fracture energy is evaluated from (5b) and the results are shown in fig. 4. Both materials show a considerable scatter in the data but a quantitative estimate of Γ_0 can still be made. From fig. 4, the fracture energy of T300/5208 is found to be 260 N/m (1.5 lb/in.)$\pm$ 20% while for T300/BP-907 the value is 805 N/m (4.6 lb/in.)$\pm$ 30%. Additional cleavage experiments on T300/5208, reported in [9],

have yielded similar value for Γ_0.

Fig. 4 shows that the value of Γ_0 in tests #A1 and #A2 are approximately the same (within experimental scatter), even though the fracture pattern in the two tests was quite different. However, in both tests the fracture mechanism is the same, i.e interfacial separation and fiber-matrix debonding, and no fiber rupturing. The relatively large value of Γ_0 obtained for the T300/BP-907 composite indicates that a good fiber to matrix bonding is achieved with the BP-907 matrix. This good bonding leads to an actual fiber breakage which accounts for the large fracture energy.

Impact experiments on T300/BP-907 composite laminates have shown a great improvement in both damage generation phase [10] and damage growth phase [10,11] over the T300/5208 composite. It is believed that the reason for that improvement is directly related to the better fracture toughness found for the T300/BP-907 over the T300/5208 (by a factor of 3).

3.3 VISCOELASTIC CHARACTERIZATION OF THE NEAT RESIN

The viscoelastic behavior of the adhesives used in fabricating the T300/5208 and T300/BP-907 composites is achieved through torsion tests. Section 3.3.1 describes torsion specimen preparation. The creep measurement procedure is outlined in section 3.3.2 and test results are given in section 3.3.3.

3.3.1 Specimen Preparation

The Narmco-5208 and the BP-907 resins were obtained from NASA-Langley in the form of spherical beads. These beads were molded in a cylindrical cavity according to the following procedure;

Heat (250^0 F for Narmco-5208 and 300^0 F for BP-907) and hold while degassing under vaccum. Increase temperature slowly to 350^0 F and hold (under vaccum) for two hours. Cool slowly over a period of few hours.

Torsion specimens were then machined from the molded cylinders to the dimension shown in sketch 1. The specimen ends were held by the fixtures shown in sketch 1 which provide good gripping for the specimen ends to eliminate possible slipping which may occur at high temperature testing.

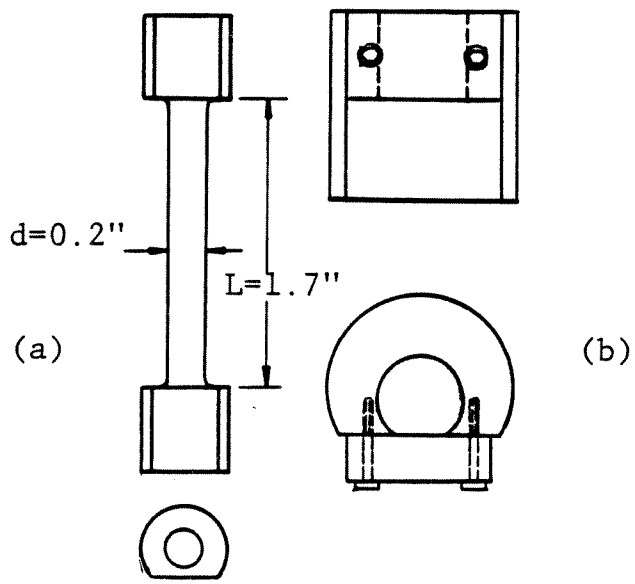

SKETCH 1

(a) - Specimen
(b) - End Fixtures

3.3.2 Creep Measurements

Creep tests were carried out on an in-house developed Creep Torsiometer [12] where all moving parts, including specimen support shaft, torsional loading unit and specimen rotation measurement device are supported by air-bearings to minimize friction. The specimen is housed in an inner chamber constructed from a thick walled metal. The chamber itself is contained in a temperature-controlled cabinet so that after thermal equilibrium is reached (about two hours), specimen temperature is maintained within $\pm 0.1^0$ C indefinitely. All creep data were obtained from a single specimen. Tests were initiated from the lowest temperature. After each test, the load direction was reversed so as to eliminate cumulative deformation in subsequent tests.

3.3.3 Test Results

Figure 5 presents plots of creep compliance J(t) versus time for the two materials tested. These plots were derived from the experimental data through the classical relation for torsion of circular cross sections, which gives

$$J(t) = \frac{\gamma(t)}{\tau} = \frac{\pi d^4\, \Theta(t)}{32LM} \qquad (13)$$

where $\gamma(t)$ and τ are the time-dependent shear strain and constant shear stress, respectively, and d, $\Theta(t)$, L and M are the specimen diameter, measured twist angle, specimen gauge length, and applied torque, respectively.

Master creep curves for Narmco-5208 and BP-907 were generated from the data in fig.5. First, test temperature was accounted for by shifting each curve vertically by amount T/T_0 [13], where T_0 is the reference temperature taken to be 21^0 C for Narmco-5208 and 22^0 C for BP-907. Then horizontal shifting was effected to the reference data to produce the smoothest composite curve from the individual curves. This master curve is presented in fig. 6. It can be seen

from this figure that the BP-907 matrix exhibits a much more significant creep behavior than the Narmco-5208, and its compliance at a reference temperature of 22^0 C coincides with that of Narmco-5208 at 53^0 C over a period of 5 years (over 8 decades of time). At the end of this time period, and at a temperature of 53^0 C, the BP-907 will creep by about 350% while the Narmco-5208 by only 60%.

As can be seen in fig. 6 the shifting of creep data to form a master creep curve was accomplished with a good degree of consistency for both materials. Thus, both materials appear to be characterized as thermorheologically simple materials so that

$$J(T,t) = (T_0/T)\, J\left\{ T_0,[t/a_T(T)] \right\} \tag{14}$$

where $a_T(T)$ is the temperature-dependent shift factor which is plotted in fig 7. Note that the glass-transition temperature T_g for BP-907, as indicated by the abrupt change in the slope of the shift factor at 98.5^0 C, is much less than that of Narmco-5208, reported in [14] to be 200^0 C. The data in fig 7 are well approximated by the WLF equation[1] [13] given by

$$\text{Log } a_T = \frac{-C_1(T-T_s)}{C_2 + (T-T_s)} \tag{15}$$

as can be seen by the solid curves in fig.7. The constants C_1 and C_2 are:

Narmco–5208 with $T_s=21^0$C; $C_1=32.5$, $C_2=129.5$.

BP–907 with $T_s=T_g$; $C_1=10.7$, $C_2=197.5$ for $T< T_g$ and $C_1=8.5$, $C_2=28.2$ for $T> T_g$.

1 This equation was proposed in [13] for temperatures above the glass-transition temperature of the material. Here it is also applied to temperatures above the glass-transition temperature.

CONCLUSIONS

A modified cleavage type analysis for evaluation of fracture energy in fiber/epoxy laminates was developed. Cleavage tests were carried out on two groups of composites of current interest, i.e T300/5208 and T300/BP-907. Test results indicate a factor of approximately 3 in favor of the T300/BP-907 composite. In the T300/5208 composite, fracture occurred as an interlaminar separation or fiber-matrix debonding while in T300/BP-907 the failure is characterized by fibers rupturing. The superiority in fracture toughness is attributed to the better fiber-matrix adhesion obtained with the BP-907 matrix. Two rather unique fracture patterns were found for the T300/5208 composite. The fracture mechanism in both cases was the same, however, which led to the same value for the fracture energy. The better fracture resistance found for the T300/BP-907 composite supports the theoretical model prediction in chapter 2 that the fracture energy is an important factor in controlling damage arrest, and is consistent with improved damage growth tolerance found in experiments reported in [10,11]. Therefore, it may be of practical importance to employ this type of testing in the selection process of the matrix material.

Viscoelastic characterization of the neat resins used in fabricating the above mentioned composites has shown that the BP-907 resin is affected more than the Narmco-5208 by variations in time and temperature, and its glass-transition temperature (100^0 C) is well below that of Narmco-5208 (200^0 C). The significant creep behavior found in the BP-907 lessened its fracture toughness advantage in those cases where long term durability is of concerned.

REFERENCES

1. J.W. Obreimoff, 'The Splitting Strength of Mica", Proc. Roy. Soc. (London), A127, p 290, (1980)

2. Y. Inoue, Y. Kobatake, "Mechanics of Adhesive Joints", Part IV: *Peeling Test*, Applied Scientific Research (A), Vol. 8, p 321, (1959).

3. J.J. Gilman, "Direct Measurement of Surface Energies of Crystals", J. Appl. Phys., Vol. 31, p 2208, (1960).

4. N.L. Svensson, "The Variation of the Fracture Energy of Brittle Plastics with Temperature", Proc. Phys. Soc., Vol. 77, p 876, (1961).

5. J.P. Berry, "Determination of Surface Fracture Energies by the Cleavage Technique", J. Appl. Phys., Vol. 34, No.1, p 62, (1963).

6. S. Mostovoy, P.B. Crosley, E.J. Ripling, "Use of Crack-Line-Loaded Specimens for Measuring Plane-Strain Fracture Toughness", J. of Materials, Vol. 2, No.3, p 661, (September 1967).

7. M.L. Williams, "The Continuum Interpretation of Fracture and Adhesive", J. Appl. Polym. Sci., Vol. 13, p 29, (1969).

8. S. Mostovoy, E.J. Ripling, "Fracture Toughness of Adhesive Joints", J. Adhesion, Vol. 3, p 125, (1971).

9. H. Chai, C.D. Babcock, W.G. Knauss, "Fracture Energy of Graphite-Epoxy Composite Laminates", GALCIT SM 79-13, (July 1979).

10. B.A. Byers, "Behavior of Damaged Graphite/Epoxy Laminates Under Compression Loading", NASA CR 159293, (August 1980).

11. M.D. Rhodes, "Damage Tolerance Research on Composite Compression Panels", Selected NASA Research on Composite Materials and Structures,

NASA-CP 2142, p 107, (August 1980).

12. V.H. Kenner, W.G. Knauss, H. Chai, "Thermorheological Characterization of Structural Adhesive", Experimental Mechanics, Vol. 22, No. 2, pp 75-80, (February 82).

13. M.L. Williams, R.F. Landel, J.D. Ferry, "The Temperature Dependence of Relaxation Mechanisms in Amorphous Polymers and Other Glass Forming Liquids", J. Amer. Chem. Soc. Vol. 77, p 3701, (1965).

14. H.G. Carter, K.G. Kibler, J.D. Reynolds, in "Advance Composite Materials-Environmental Effects", ASTM STP 658, J.R. Vinson, Ed, p 84, (1978).

TABLE I

Test Data*

P(ℓb)	ℓ(in.)	δ(in.)	P(ℓb)	ℓ(in.)	δ(in.)
A#1, b=0.205 in., t=0.238 in.			B#1, b=0.359 in., t=0.302 in.		
3.05	2.65	0.21	8.50	3.74	0.51
3.12	2.96	0.27	7.45	4.13	0.60
2.31	4.02	0.44	7.78	4.33	0.69
1.75	5.34	0.75	7.70	4.61	0.81
1.82	5.67	0.85	7.25	4.80	0.85
1.50	6.25	0.96	5.38	5.81	1.05
1.42	6.77	1.08	5.34	5.94	1.10
1.37	7.47	1.38	6.21	6.22	1.47
			4.57	7.32	1.63
			5.50	7.36	2.04
			5.50	7.64	2.23
A#2, b=0.217 in., t=0.236 in.			B#2, b=0.280 in., t=0.302 in.		
3.70	2.72	0.23	5.87	4.17	0.70
2.65	3.62	0.34	4.74	4.92	0.83
1.85	4.67	0.50	5.05	4.96	0.92
1.62	5.42	0.70	5.05	5.00	0.94
1.43	6.35	0.95	4.80	5.39	1.05
1.38	7.05	1.25	4.70	5.63	1.15
1.29	7.85	1.54	4.00	6.54	1.50
			3.40	7.40	1.79

* P is the load, ℓ-crack length, δ-ends separation, b-beam width and t is total beam thickness.

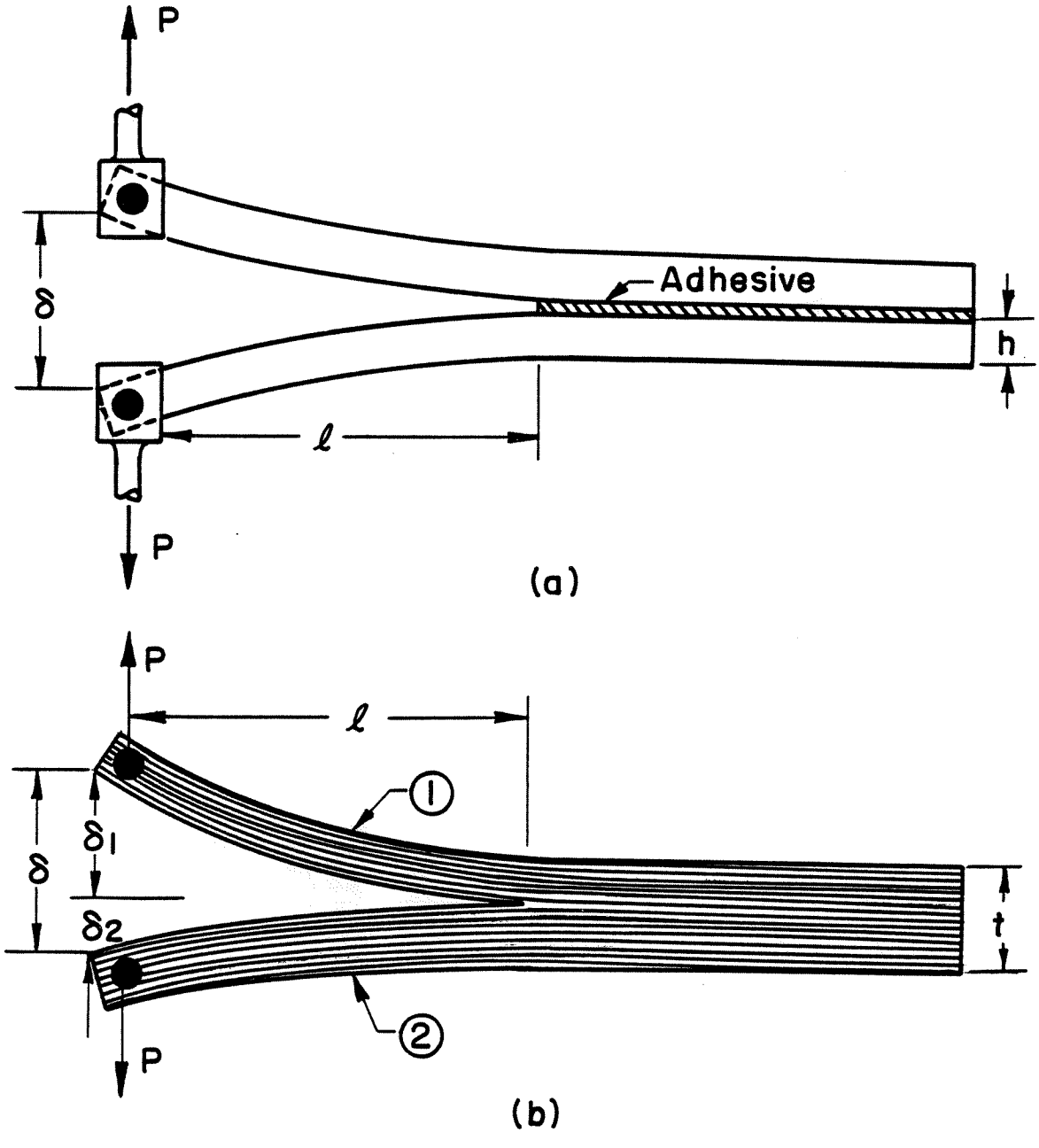

FIG. 1 CLEAVAGE SPECIMEN;(a)-PROTOTYPE, (b)-MODIFIED

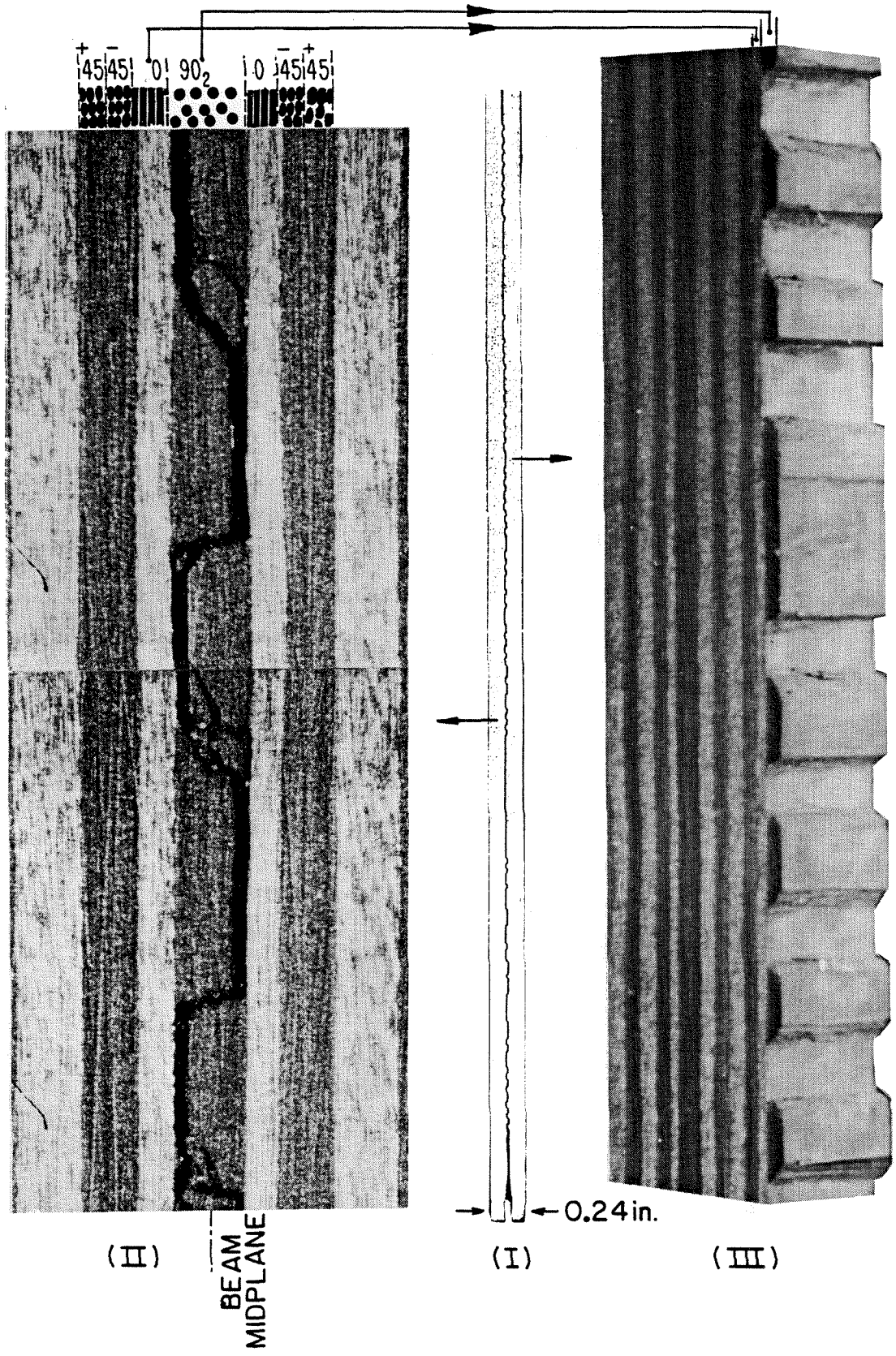

FIG. 2a FRACTURE SURFACE OF A 48-PLY T300/5208 LAMINATE; TEST #A1

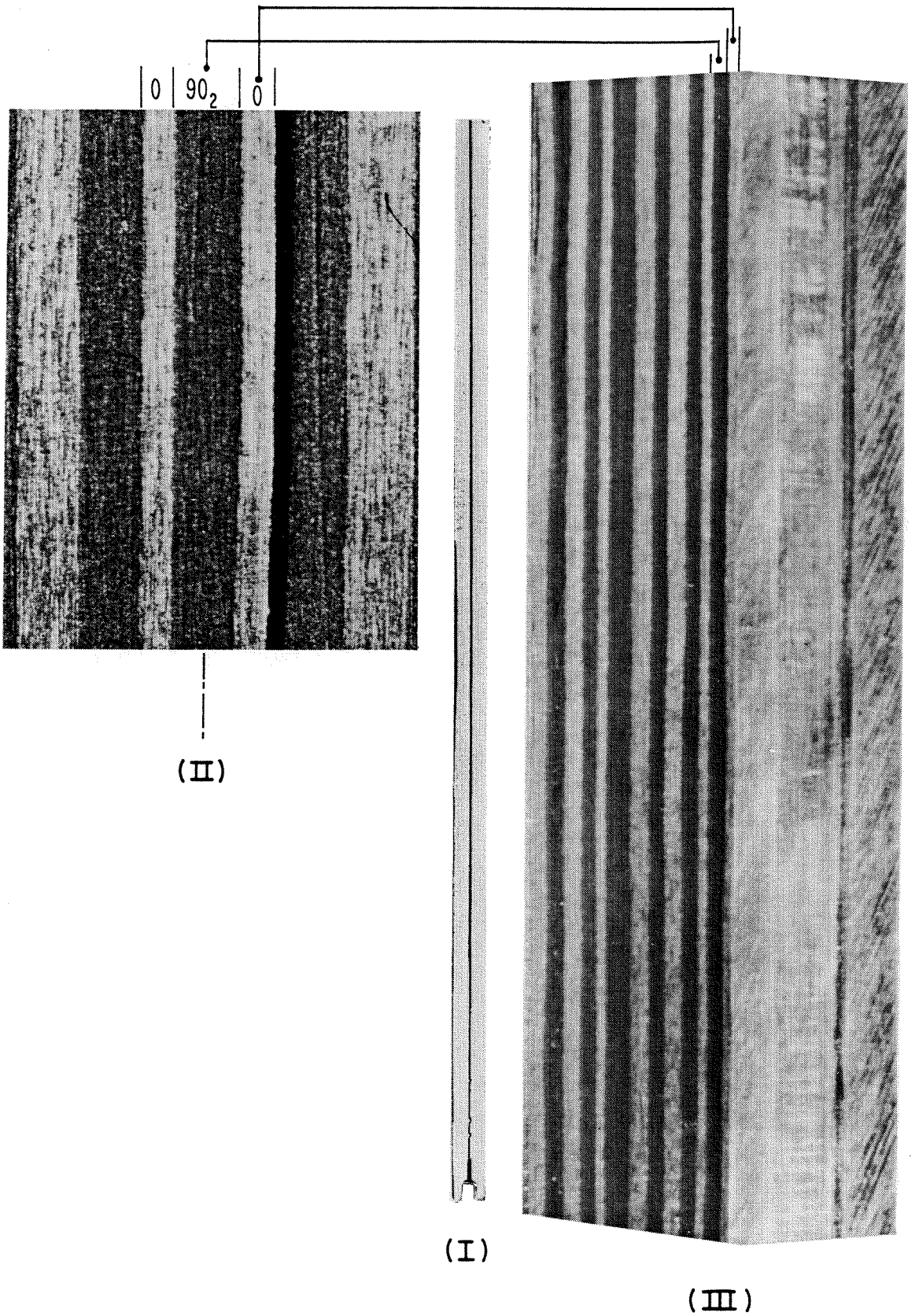

FIG. 2b AS IN FIG. 2a, TEST #A2

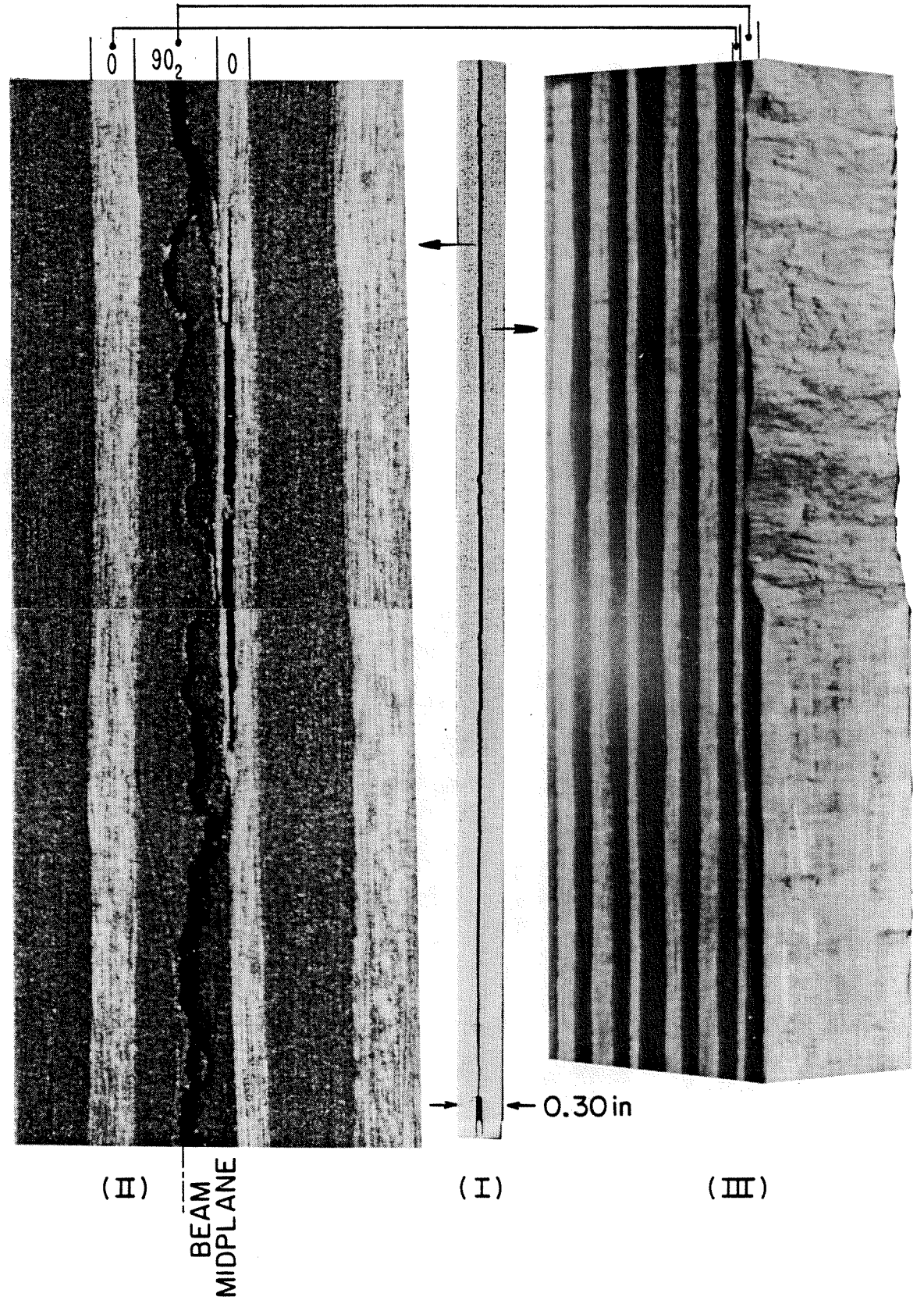

FIG. 2c FRACTURE SURFACE OF A 48-PLY T300/BP-907 LAMINATE; TEST #B1

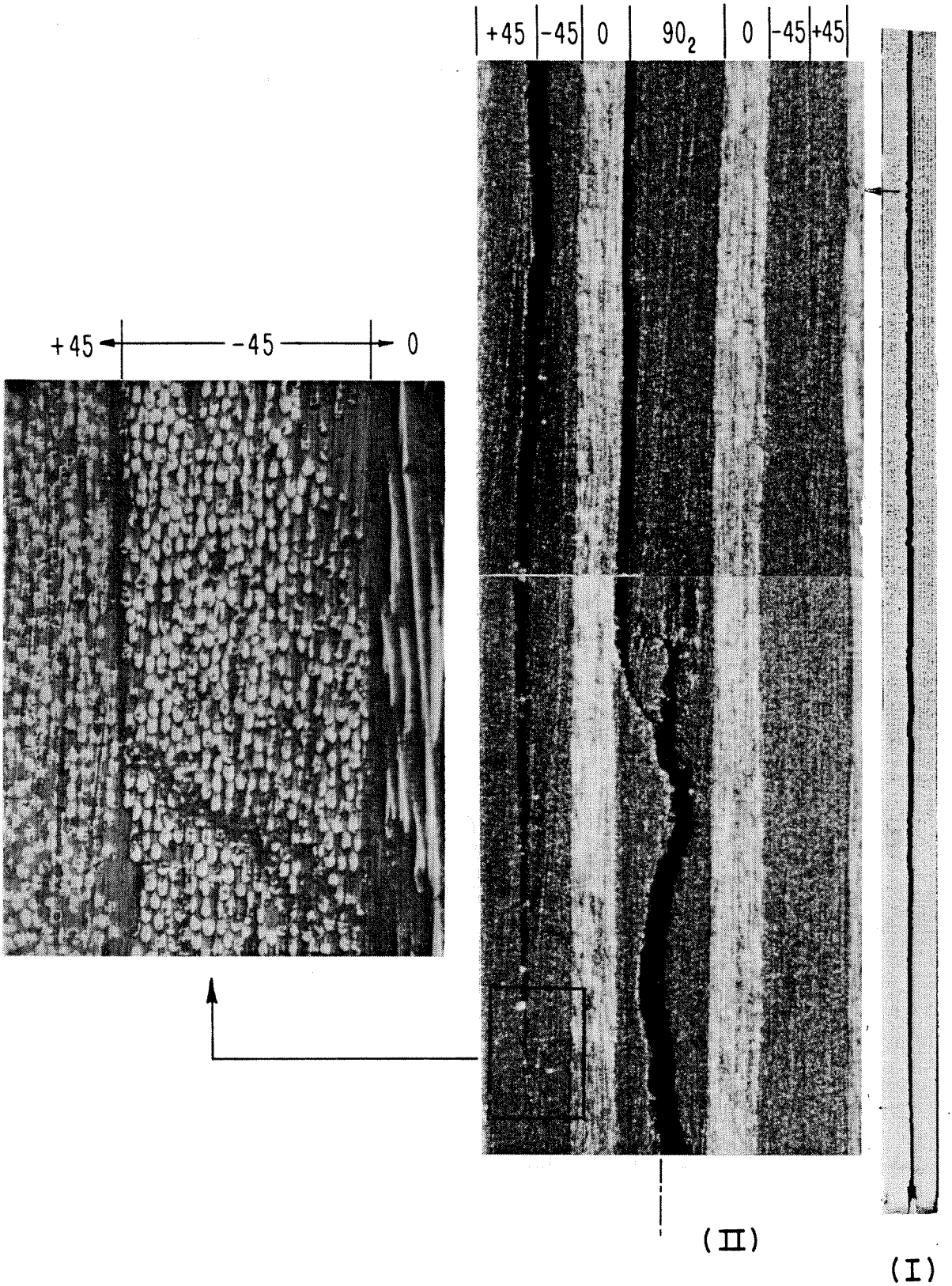

FIG. 2d AS IN FIG. 2c, TEST #B2

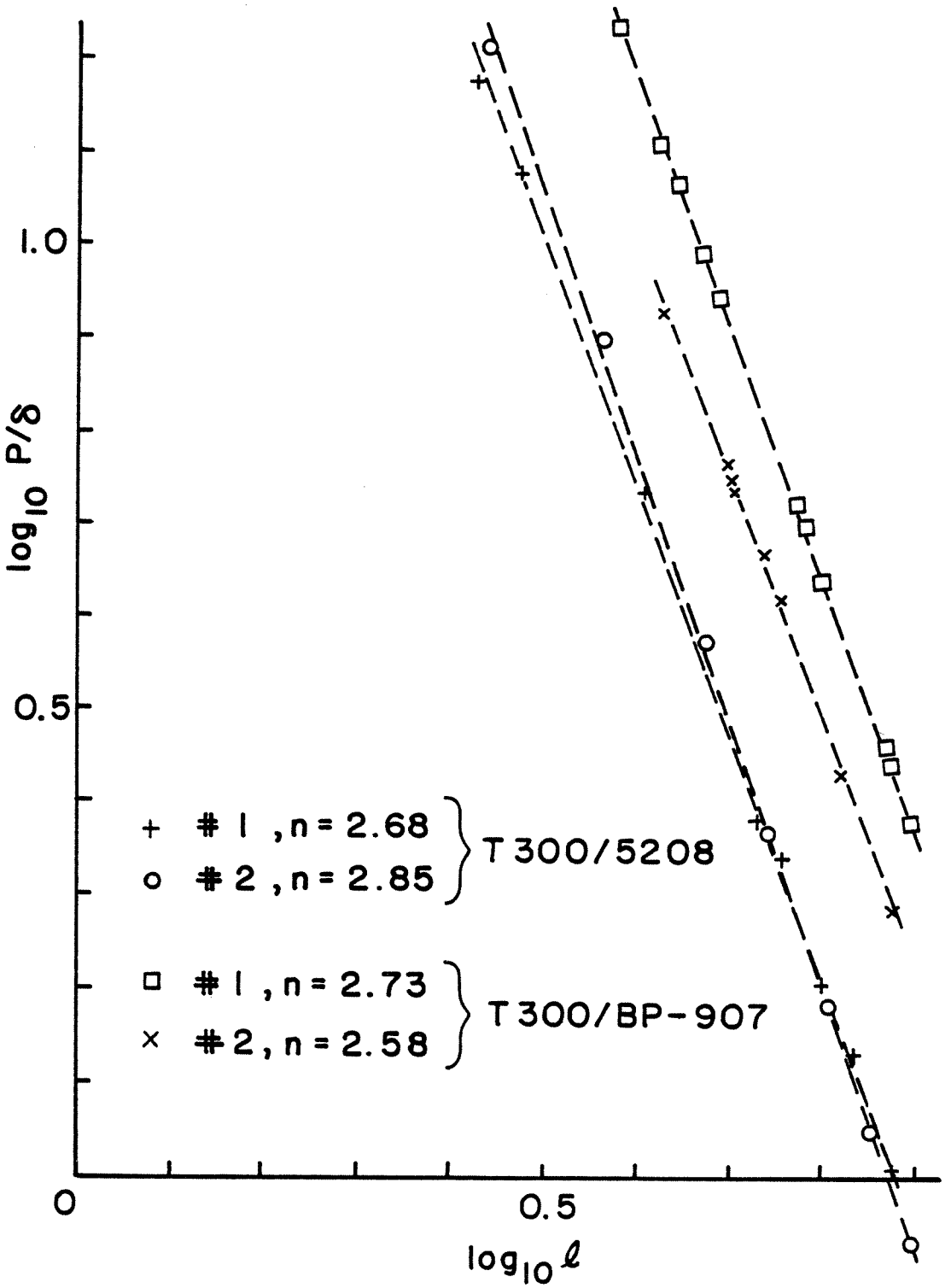

FIG. 3 P/δ VS. ℓ – n DETERMINED FROM $\frac{\delta}{P} = (a_1 + a_2)\ell^n$

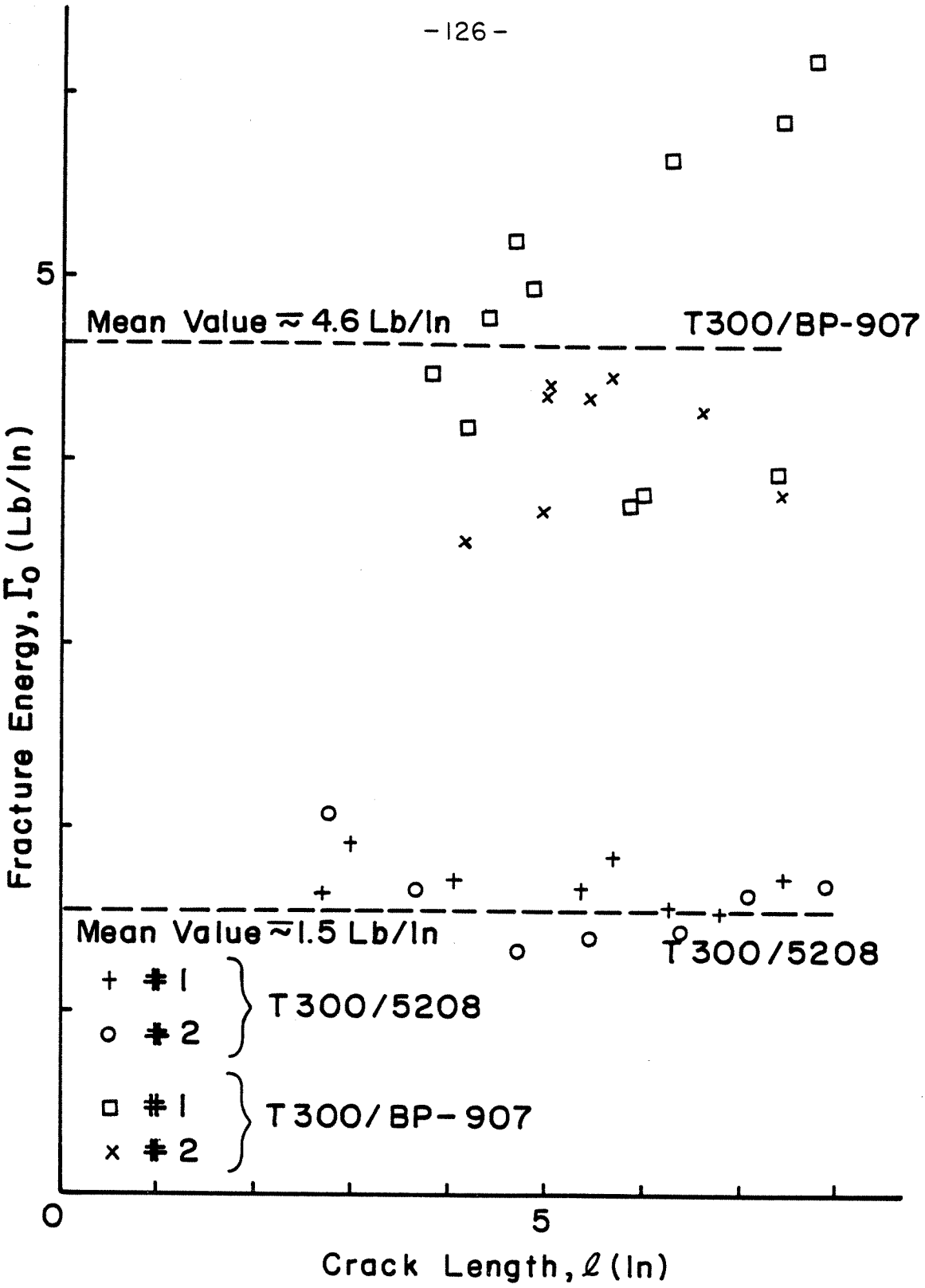

FIG. 4 EXPERIMENTAL DATA FOR FRACTURE ENERGY

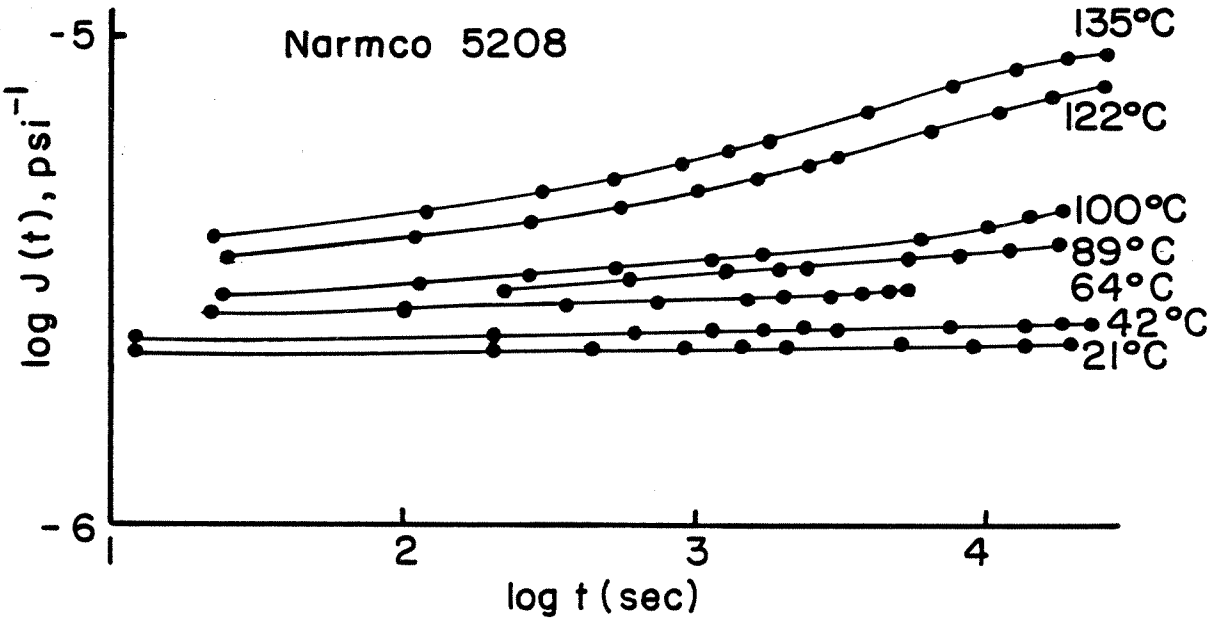

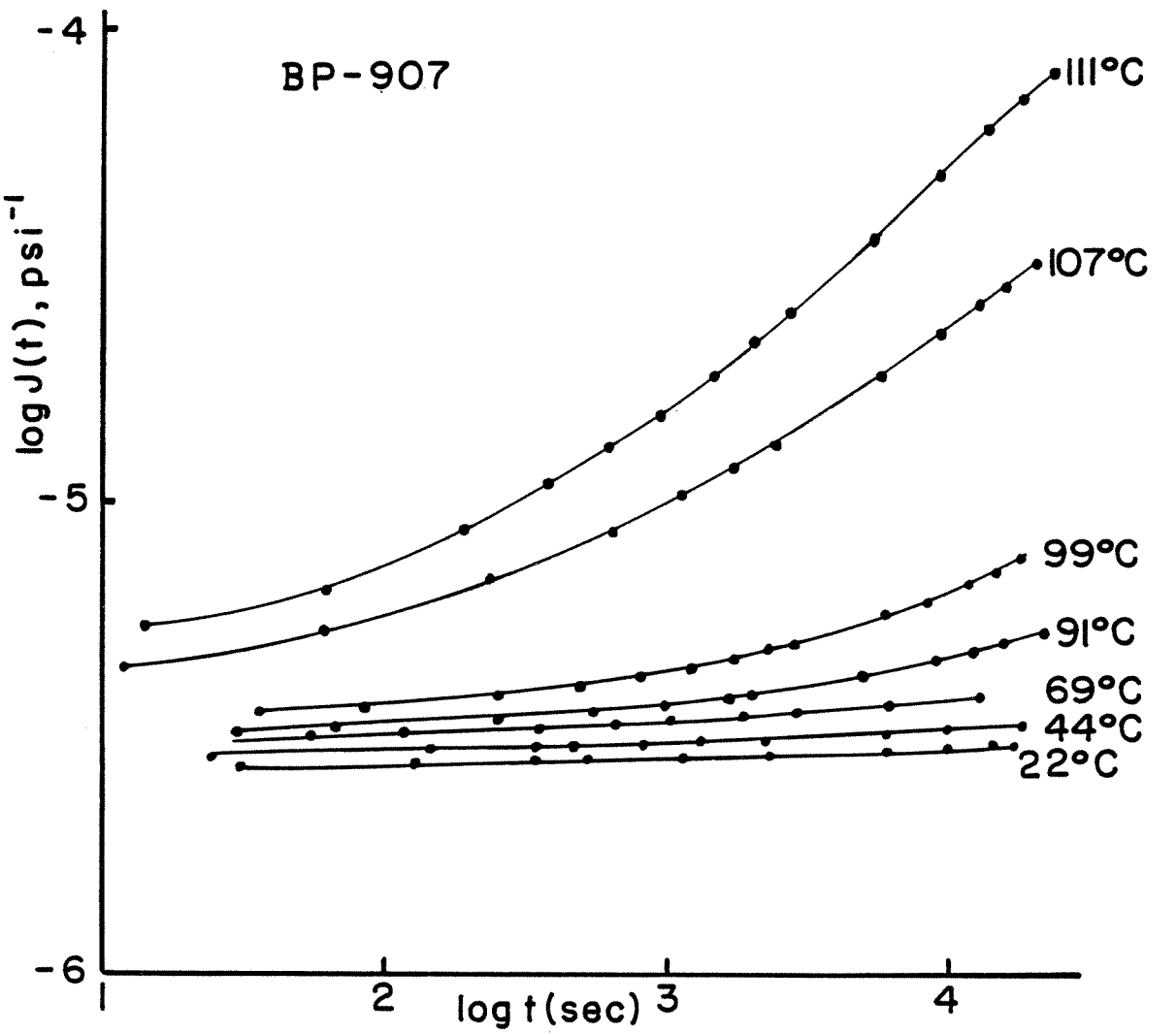

FIG. 5 CREEP DATA AT SEVERAL TEMPERATURES

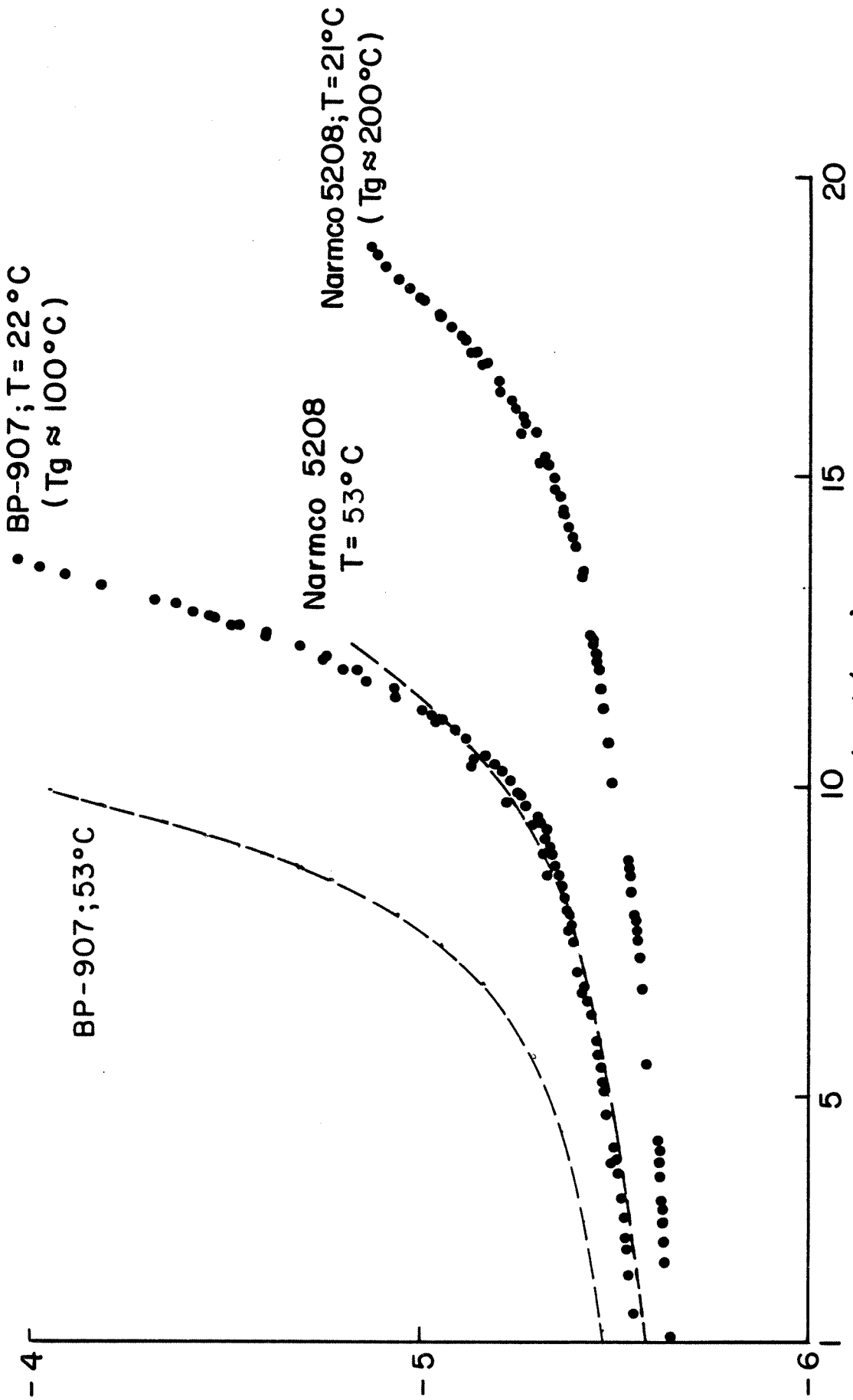

FIG. 6 MASTER CREEP COMPLIANCE

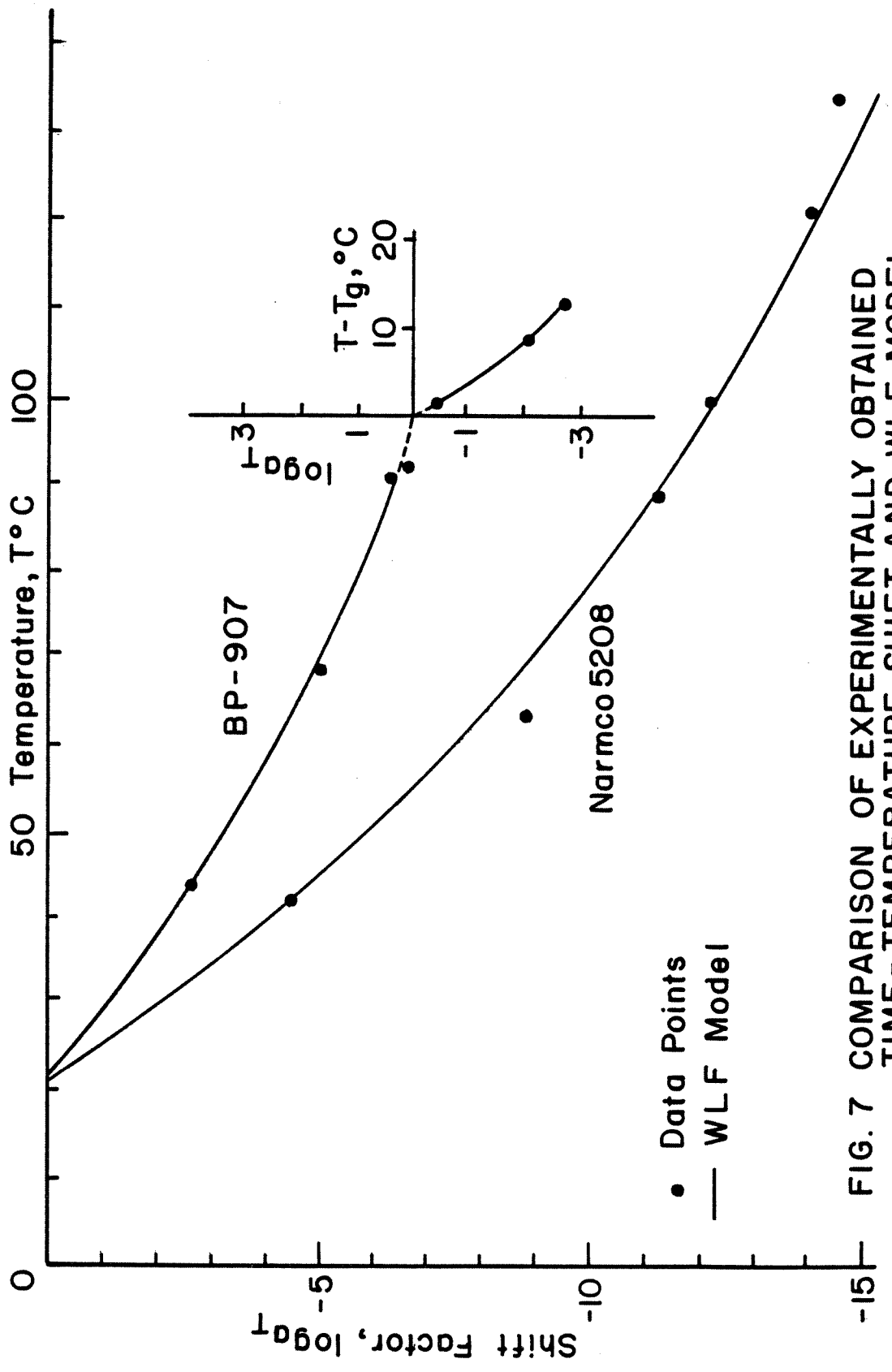

FIG. 7 COMPARISON OF EXPERIMENTALLY OBTAINED TIME-TEMPERATURE SHIFT AND WLF MODEL